Title
Exploring Basic Properties and Applications of Nitrogen-Vacancy Color Centers in Diamond

Author
Kehayias, Pauli

Publication Date
2015

Exploring Basic Properties and Applications of Nitrogen-Vacancy Color Centers in Diamond

by

Pauli Mark Kehayias

A dissertation submitted in partial satisfaction of the

requirements for the degree of

Doctor of Philosophy

in

Physics

in the

Graduate Division

of the

University of California, Berkeley

Committee in charge:

Professor Dmitry Budker, Co-chair
Professor Holger Müller, Co-chair
Professor Hartmut Häffner
Professor Joel E. Moore
Professor Jeffrey A. Reimer
Professor Dan M. Stamper-Kurn

Spring 2015

Abstract

Exploring Basic Properties and Applications of Nitrogen-Vacancy Color Centers in Diamond

by

Pauli Mark Kehayias

Doctor of Philosophy in Physics

University of California, Berkeley

Professor Dmitry Budker, Co-chair

Professor Holger Müller, Co-chair

Nitrogen-vacancy (NV) defect centers in diamond have generated much interest for their uses in quantum information and sensing. Despite the ongoing improvements in sensitivity and the range of new applications, much about the NV basic physics remains unresolved, which is important to understand in order to fully exploit potential uses. In this work I describe a series of experiments on NV basic properties, applications, and projects in between. First, I describe an NV singlet absorption spectroscopy experiment, which searched for additional NV electronic states and studied the $^1A_1$ phonon modes. Next, I discuss an NV microwave saturation spectroscopy experiment, which is useful for NV thermometry, removes inhomogeneous broadening, and can yield information about diamond magnetic spin bath dynamics. I then describe an NV relaxation experiment that senses GHz-frequency magnetic noise, which we demonstrated using paramagnetic substitutional nitrogen (P1) centers. Finally, I describe open questions on the NV singlet states, saturation spectroscopy, and relaxation (and how to address them), and report on my ongoing work on using NVs for nuclear polarization and rotation sensing.

Contents

Contents **i**

List of Figures **iii**

List of Tables **v**

1 Background **1**
1.1 Basic properties 2
1.2 NV sensing and quantum information 9
1.3 Advantages and limitations 16
1.4 Overview of work presented 20

2 NV Singlet Spectroscopy **21**
2.1 Introduction 21
2.2 Experiment and results 22
2.3 912 nm polarization selection rules 27
2.4 Analysis and discussion 30
2.5 Summary 31

3 NV Saturation Spectroscopy **33**
3.1 Introduction 33
3.2 Methods and results 34
3.3 Analysis and discussion 39
3.4 Summary 46

4 NV Relaxation and Decoherence Spectroscopy **47**
4.1 Magnetic noise sensing by NV relaxation 48
4.2 Previous NV electronic T_1 work 51
4.3 Experimental details and results 54
4.4 Summary 58

5 Summary and Outlook **60**
5.1 Summary 60

5.2 Ongoing work 65
5.3 Outlook 68

Bibliography **69**

List of Figures

1.1 NV embedded in the diamond lattice 2
1.2 LCAO and NV energy level diagram 5
1.3 Simplified zero-phonon line and phonon sideband illustrations 6
1.4 Optical pumping and experimental setup schematic 8
1.5 NV ground-state substructure 9
1.6 Example ODMR plot with a magnetic field in an arbitrary direction 10
1.7 Photon shot noise ODMR sensitivity analysis 12
1.8 NV Rabi oscillations and ^{14}N-state readout 15

2.1 The NV electronic singlet states 23
2.2 NV singlet absorption spectroscopy schematic 24
2.3 $^1E \rightarrow {}^1A_1$ and $^3E \rightarrow {}^3A_2$ low-temperature spectra 25
2.4 $^1E \rightarrow {}^1A_1$ and $^3E \rightarrow {}^3A_2$ one-phonon spectra 26
2.5 Temperature dependence of NV singlet absorption features 28
2.6 912 nm absorption polarization dependence 29

3.1 CW and pulsed hole-burning schemes 35
3.2 CW hole-burning demonstration 36
3.3 Schematic for a CW NV saturation spectroscopy experiment 37
3.4 The effect of varying the pump frequency f_+ and the axial magnetic field B on the hole center frequency f_- 38
3.5 NV saturation spectroscopy thermometer demonstration 39
3.6 NV population dynamics in a pulsed hole-burning experiment 41
3.7 Expected pulsed hole-burning results 41
3.8 Expected CW hole-burning results 43
3.9 Calculated expectations for a pulsed hole-burning experiment 45

4.1 Phonon and magnetic-dipole NV T_1 relaxation 48
4.2 Hahn echo and ESEEM coherence revivals 50
4.3 T_1 common-mode rejection scheme 52
4.4 NV-P1 energy-level crossings 53
4.5 Schematic for NV T_1 measurements 54

4.6 NV-P1 energy-level crossings 57
4.7 T_2^* and T_2 near 500 G 59

5.1 Schemes for measuring the NV triplet-singlet energies and the ^1E ionization energy 62
5.2 Detected hole width at different hole microwave chopping frequencies 63
5.3 Pulsed-hole lifetime measurement attempt 64
5.4 ODMR plots for a ^{13}C sample near 500 G 67

List of Tables

2.1 One-phonon peak energies for ${}^1E \rightarrow {}^1A_1$ and ${}^3E \rightarrow {}^3A_2$ 27
2.2 C_{3v} selection rules for electric dipole transitions 29

3.1 Specifications for the samples used for NV saturation spectroscopy 35

4.1 NV T_1 and T_2 magnetic noise detection comparison 51
4.2 Sample specifications for T_1 and T_2 measurements near 500 G 55

Acknowledgments

I thank Professor Dmitry Budker for his guidance, and my committee members, Professors Hartmut Häffner, Joel Moore, Holger Müller, Jeffrey Reimer, and Dan Stamper-Kurn. I also thank the US Department of Energy Office of Science Graduate Fellowship (SCGF) program for funding a portion of my graduate career (including equipment and travel). I also thank my labmates, collaborators, and group visitors, which include Victor Acosta, Audrius Alkauskas, Yehuda Band, Nir Bar-Gill, Lykourgos Bougas, SangKook Choi, Viatcheslav Dobrovitski, Marcus Doherty, Yannick Dumeige, Damon English, Ran Fischer, Ron Folman, Florian Gahbauer, Ádám Gali, Wojciech Gawlik, Liam Hall, Phil Hemmer, Lloyd Hollenberg, Andrey Jarmola, Kasper Jensen, Jonghwan Kim, Mark Kowarsky, Nathan Leefer, Alex Lohrmann, Sean Lourette, Neil Manson, Jeronimo Maze, Mariusz Mrózek, Milos Nesladek, Linh Pham, Daniel Rudnicki, Karen Sauer, David Simpson, and Alastair Stacey.

Chapter 1

Background

Physicists often prefer analyzing the simplest possible problems, as these problems have the highest chance of yielding an analytical solution. Although more general problems are challenging and complex, they often lead to interesting results that are unobtainable with simplified analyses. In condensed-matter physics we often consider infinite lattices, but these materials can become more interesting when we add impurities. Gemologists and materials scientists seek to understand how defects give rise to desirable properties in gems and materials. Some examples are electron and hole donors in semiconductors; tuning the carrier densities in silicon and germanium makes semiconductor electronics possible. Atomic and optical physicists are interested in atom-like solid-state defects for lasers and masers (such as ruby, Nd:YAG, Nd:YVO$_4$, and Ti:sapphire), quantum information, sensing, and other applications. This argument applies to color centers in diamond. Diamond is a favorable material for studying "atomic physics" with color centers since diamond is optically transparent, allows long room-temperature lifetimes for defect centers, and can be grown and nanofabricated. In this work, we consider the the nitrogen-vacancy (NV) center in diamond and its use in sensing [1–3].

An NV color center (Fig. 1.1) is a defect center consisting of a substitutional nitrogen atom adjacent to a lattice vacancy. When negatively charged (NV$^-$) they are used for high-spatial-resolution sensing (magnetometry, electrometry, thermometry, and barometry) and for quantum information (with a scalable quantum computer as the eventual goal) [4–10]. Furthermore, NV-based sensors and qubits can work in a wide range of physical conditions (cryogenic to 600 K in temperature, atmospheric pressure to 60 GPa, and zero-field to several tesla in magnetic field). Since they work in ambient conditions, NV experiments can often be technically simpler than other sensing experiments. Furthermore, NV sensors are useful in applications requiring high spatial resolution, and are also biocompatible and do not photobleach. NVs are also an emerging sensing technology with potential for novel applications and much room for improvement, having generated much excitement and development over the last decade.

Despite the rapid NV applications development, our grasp of NV basic properties is incomplete. It is important to understand NV basic properties to enable unanticipated applications and research directions. Following an introduction describing NV properties, applications, advantages, and limitations, the later chapters detail my work on NV centers, which extends the library of NV sensing techniques and advances our understanding of NV physics.

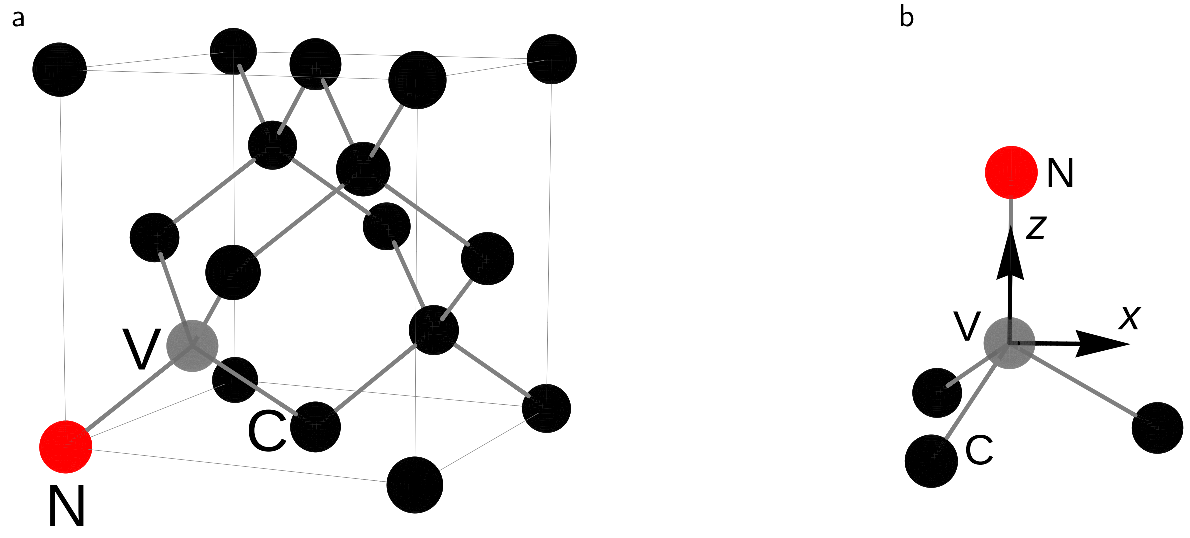

Figure 1.1: (a) An NV center embedded in the diamond crystal lattice. The diamond lattice constant is 0.3567 nm, and the carbon-carbon separation is 0.1545 nm [11]. (b) An NV center, with the x- and z-axes labeled.

1.1 Basic properties

Diamond sample types and manufacturing

Although natural diamonds can contain NV centers and other defects [12], we usually use synthetic diamonds in order to have a better understanding of what the samples contain and to have a controlled and reproducible manufacturing method. There are several types of NV experiments that require different samples:

- NV ensemble experiments, where we interrogate many centers in a sample with a sheet of NVs or a uniform spatial distribution.
- Single-NV experiments, where we use a sparsely-populated sample and select one NV with which to make measurements.

- NV nanodiamond experiments, which use nanodiamonds containing one or many NV centers. The nanodiamonds can be attached to AFM cantilevers, trapped in optical dipole traps, or functionalized and put into living cells [13–15].

There are several ways to manufacture diamond samples to suit these experimental requirements:

- High-pressure high-temperature (HPHT) growth, which is done in an anvil press at 5000 GPa and 1700 K and is similar to natural diamond formation. After a solvent metal dissolves the carbon in a source graphite block, the carbon precipitates onto a seed crystal, which then grows. This yields samples with $\sim$100 ppm nitrogen, though making ultrapure samples with HPHT growth is impossible.
- Chemical vapor deposition (CVD), where diamond is grown layer-by-layer in a gaseous environment. CVD produces samples with fewer nitrogen impurities (roughly 1 ppb to 1 ppm).
- Explosives detonation (such as with TNT or RDX), which produces nanodiamonds with high nitrogen and NV densities.

HPHT and CVD growth can yield a variety of diamond qualities, such as polycrystalline, monocrystalline, optical-grade, and electronic-grade diamond. With a given manufacturing technique, we have further control over how NV centers are formed:

- Crystal growers can vary the nitrogen concentration in HPHT and CVD growth, and although some NVs form naturally, most embedded nitrogen atoms do not. These samples can be used as-is (for instance, in a single-NV experiment), but are often irradiated with high-energy electrons, protons, C_2, or N_2 to improve the N to NV yield.
- Irradiating diamond samples can create vacancies in the diamond lattice and also implant nitrogen defects in the case of N_2. Varying the energy and species of the accelerated particles yields a uniform or near-surface defect layer. Irradiation and implantation can be done with particle accelerators or with an electron microscope [16, 17]. After creating vacancies, the NV density is not much improved as the N and V locations are uncorrelated, but annealing the diamond samples after irradiation improves the NV yield, as the vacancies migrate next to nitrogen atoms [16, 18]. Annealing temperatures range from 700-1200 °C.
- Using a growth technique called delta-doping, CVD diamond growth can create an NV layer (usually near the surface) by introducing nitrogen. To form the NV layer, ^{15}N is often added to the diamond growth environment to distinguish the near-surface NVs by the ^{15}N (instead of ^{14}N) ground-state hyperfine splitting. This ensures that CVD samples have few NVs except near the surface, where they are most useful for sensing

external fields. We can also use delta-doping to create NV layers with known relative separations [19, 20].

- Bulk diamond samples can be turned into nanodiamonds by ball milling or chemical etching [21, 22].
- Diamond samples can be chemically etched to make diamond nanostructures, including optical waveguides, resonators, photonic crystals, or atomic force microscopy (AFM) cantilevers [13, 23, 24].

Many experiments use diamond samples with few defects and select a particular NV to investigate. However, motivated by vapor cell magnetometry (which uses an ensemble of alkali atoms), in this work we instead study NV ensembles. Interrogating many NVs can lead to better signal-to-noise, but this comes at the expense of reduced spatial resolution.

NV symmetry and electronic states

Atoms have spherical symmetry, and we use this symmetry basis to describe atomic properties like electronic wave functions, quantum numbers, and selection rules. Molecules and solid-state defects have a reduced point-group symmetry depending on their structure. An NV center has C_{3v} symmetry, meaning it is spatially invariant under the C_{3v} symmetry transformations (the identity, two 120° rotations about the z-axis, and three vertical reflection planes). NV centers also have a built-in quantization axis (the N-V z-axis, shown in Fig. 1.1b). We label NV electronic states with C_{3v} irreducible representations (orbital singlets A_1, A_2, and orbital doublet E) instead of ${}^{2S+1}L_J$ spectroscopic notation.

Chemists and condensed-matter physicists use the linear combinations of atomic orbitals (LCAO) approximation to describe molecular orbitals as superimposed atomic orbitals from contributed atoms in the molecule [25–27]. With an NV, we combine four sp^3 orbitals (the dangling-bond electrons from atoms next to the vacancy) to yield the NV orbitals labeled a_1, a_1', and $e = \{e_x, e_y\}$ (Fig. 1.2a). NV$^-$ is a "six-electron atom" (with three electrons contributed from nearest-neighbor carbon atoms, two from nitrogen, and one extra electron contributed from elsewhere in the lattice), which we place in the orbitals to yield the NV electronic states (two electronic spin triplets and four singlets, shown in Fig. 1.2b). There is also a neutral charge state (NV^0), though we will always refer to the NV$^-$ state in this work.

NV$^-$ has four experimentally-observed electronic states (the spin-triplets ${}^3A_2$ and ${}^3E$ and the spin-singlets ${}^1E$ and ${}^1A_1$) and two additional states (${}^1E'$ and ${}^1A_1'$) predicted by LCAO analysis (Fig. 1.2b). The ${}^3E$ state has a $\sim$10 ns lifetime and decays to the ${}^3A_2$ and the singlet states. The ${}^1A_1$ state has a $\lesssim$1 ns lifetime and decays largely nonradiatively to ${}^1E$, which is "metastable" with a $\sim$150 ns lifetime and decays to ${}^3A_2$ [28, 29]. The sections below describe the NV optical transitions in greater detail.

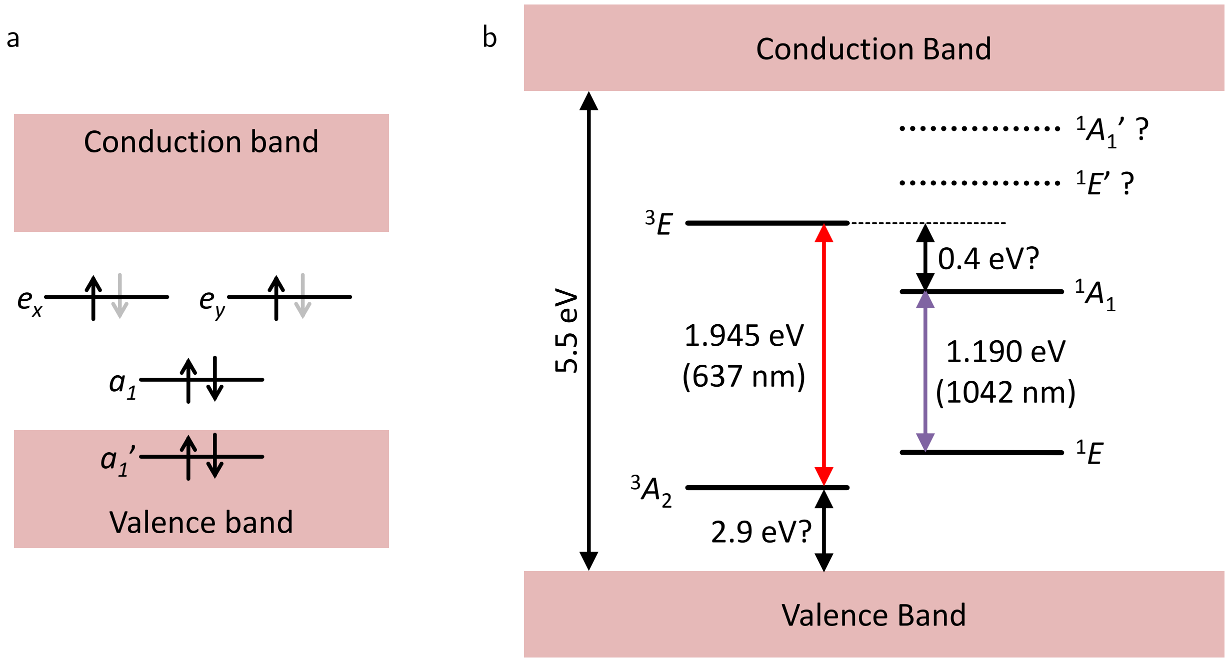

Figure 1.2: (a) The LCAO energy levels for NV$^-$. The ${}^3A_2$, ${}^1E$, and ${}^1A_1$ states have two electrons distributed among the e states (the configuration $a_1^2e^2$), while the ${}^3E$ state has one a_1 electron promoted to an e state (configuration a_1e^3). (b) The NV$^-$ energy levels. Four electronic states are confirmed experimentally, and two additional singlet states (${}^1E'$ and ${}^1A_1'$) are predicted, one or both of which may lie in the diamond conduction band. Some of the relative energies are only assessed indirectly [30, 31].

NV-phonon interactions and optical transitions

In addition to their electronic states, defect centers in solids (and molecules) have additional vibrational (and rotational) degrees of freedom, further complicating their electronic states and optical spectra [32, 33]. Figure 1.3a shows an energy-level diagram of a simplified two-level defect with one phonon mode. Since the electrons are $\sim 10^4$ times lighter than nuclei, we may use the Born-Oppenheimer approximation to simplify the problem by assuming that the lattice nuclei are static compared to the nearby electrons and that the electronic and nuclear wave functions are separable. This means that after calculating electronic spatial wave functions as a function of the nuclear normalized coordinates, we can then generate electrostatic potentials the nuclei oscillate in. This yields the nuclear phonon modes, their energies, and the nuclear equilibrium coordinates. Since the upper and lower electronic states in Fig. 1.3a may have different electronic spatial wave functions, the nuclei can vibrate in different electrostatic potentials, which leads to different nuclear equilibrium positions and phonon mode energies.

We now consider optical transitions between the electronic states in Fig. 1.3a. Depending

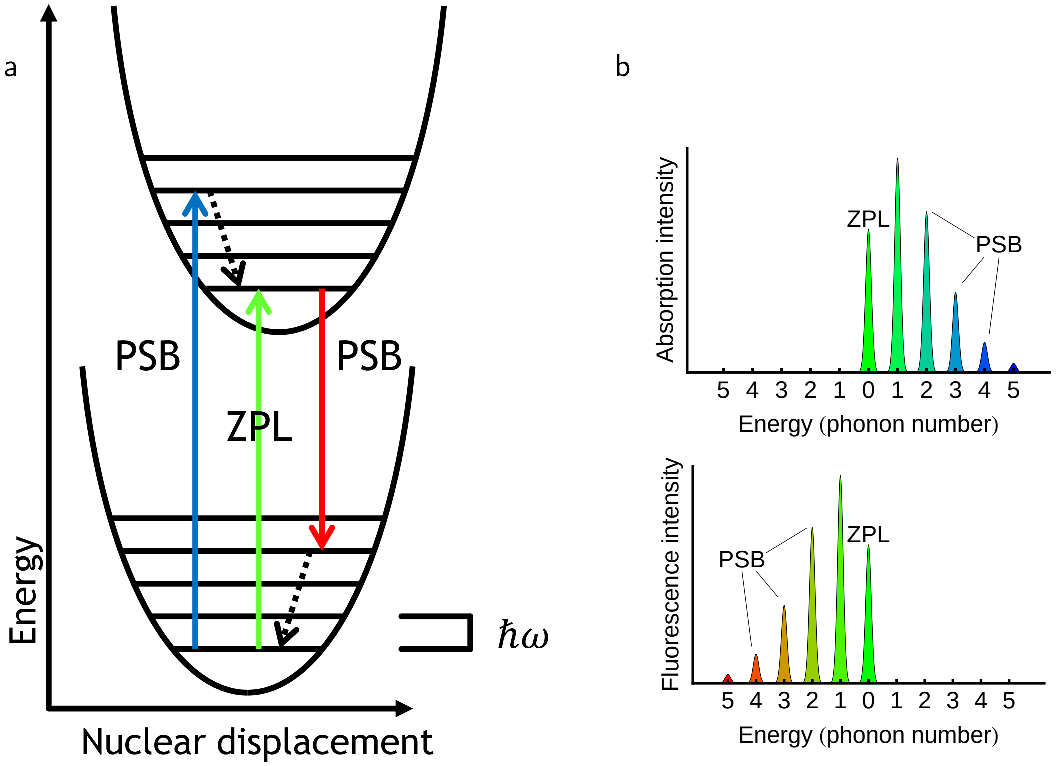

Figure 1.3: (a) Two electronic states, each with vibrational sublevels for one phonon mode. Optical excitation and decay is separated into phonon sideband (PSB) and zero-phonon line (ZPL) absorption and fluorescence; the former creates or destroys phonons while the latter does not. The electronic states may have different equilibrium separations, indicated by the horizontal offset between between the two harmonic potentials (roughly 0.01 nm [34]), which is related to the Huang-Rhys parameter S. Optical transitions are shown with solid lines, and nonradiative phonon decay to the vibrational ground state with dotted lines. (b) Optical absorption and fluorescence spectra for the simplified system shown in (a), drawn with $S = 1.5$. If the lower and upper electronic states have the same phonon mode energies, the absorption and fluorescence spectra have a mirror symmetry about the ZPL. The different colors for each peak illustrate the optical wavelength shifts for each PSB peak.

on the initial and final vibrational states, an optical transition can create or destroy phonon quanta in "phonon sideband" (PSB) transitions. Transitions that conserve phonon number are called "zero-phonon line" (ZPL) transitions. PSB transitions can have less energy (Stokes-shifted) or more energy (anti-Stokes-shifted) compared to the ZPL transition. The thermal population in excited vibrational states at room temperature is small (a 50 meV NV phonon energy corresponds to 580 K) and the vibrational excited-state lifetime is ∼1 ps (compared to a ∼10 ns ^3E lifetime) [35, 36]. The initial state in an optical transition is usually a vibrational ground state, while the final state can be any vibrational state. This means the PSB transitions are usually Stokes-shifted, as shown in Fig. 1.3b.

Vibrational properties determine the shape and extent of the PSB. Using the Franck-Condon principle, which states that the nuclei are stationary during an optical transition, we can predict the relative intensities of the ZPL and PSB transitions by calculating overlap integrals between the initial- and final-state phonon numbers. The relative intensities of the ZPL and PSB is $I(n) \propto e^{-S}\frac{S^n}{n!}$, where n is the number of phonons created and S is the the Huang-Rhys parameter, which is related to the difference in nuclear equilibrium positions and is roughly an average number of phonons the optical transition will generate. Figure 1.3b shows example emission and fluorescence spectra. Furthermore, optical emission and absorption spectra are temperature-dependent. The thermal vibrational populations change with temperature, and the ZPL and PSB features broaden as temperature increases [32, 33].

If the lower and upper electronic states have similar curvature in their nuclear electrostatic potentials, then they will have similar phonon modes, and the emission and absorption spectra will have mirror symmetry about the ZPL energy (Fig. 1.3). An $S \lesssim 1$ corresponds to initial and final states with similar nuclear equilibrium positions, putting most of the emission intensity in the ZPL. A small S indicates a transition with most of the intensity in the ZPL, making it a useful transition for monochromatic light.

Defects in solids (including NV centers) have many associated phonon modes and continuous PSB spectra. In NV centers, the $^3E \rightarrow {}^3A_2$ PSB extends from the 637 nm ZPL to beyond 1000 nm. This transition has $S = 3.49$, with only ~3% of the fluorescence intensity in the ZPL at 10 K and similar conditions for the $^3A_2 \rightarrow {}^3E$ transition [37]. Although this large S makes quantum information applications more challenging, the wide PSB removes the frequency stability requirements on $^3A_2 \rightarrow {}^3E$ excitation lasers we normally encounter in other AMO systems. We often pump the $^3A_2 \rightarrow {}^3E$ transition with 532 nm light from a frequency-doubled Nd:YAG or Nd:YVO_4 laser instead of using a frequency-stabilized 637 nm laser.

Optical properties

When illuminated with resonant laser light, NV centers are always optically pumped to the $m_s = 0$ electronic sublevel of the $^3A_2$ state, where m_s is the magnetic quantum number. Most NV sensing and quantum information experiments take advantage of the optical pumping mechanism for initialization and readout. This works differently from optical pumping with alkali atoms, which uses light polarization selection rules and the spin-orbit interaction. In NV centers, the spin-orbit interaction is weak (~5 GHz for ^3E [38] compared to a few THz for the rubidium ^{5}P states), meaning optical transitions between the triplet states largely conserve m_s (Fig. 1.4a). The NV optical pumping instead comes from the spin-selective ^3E intersystem crossing (ISC) decay through the electronic singlet states. The ^3E $m_s = \pm 1$ states have a substantial probability of decaying (enabled by triplet-singlet spin-orbit mixing) through the singlet levels back to the ground state, while the $m_s = 0$ state does not [35, 39]. This means an illuminated NV starting in the $m_s = 0$ sublevel is trapped in a cycling transition between $m_s = 0$ states, while an NV starting in the $m_s = +1$ or -1 state is eventually driven to the $m_s = 0$ cycling transition, where it remains.

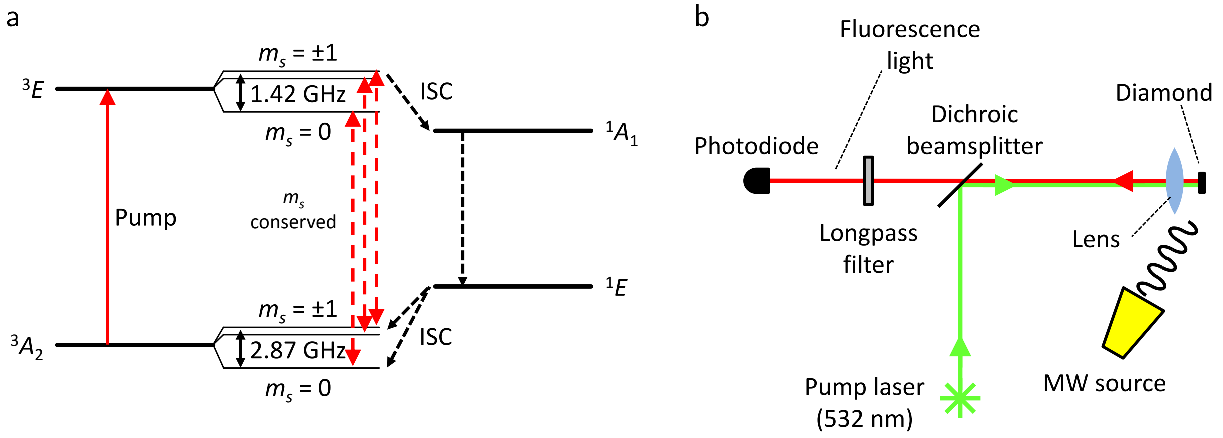

Figure 1.4: (a) The optical pumping and ISC mechanisms illustrated for a room-temperature NV. The $^3A_2 \leftrightarrow {}^3E$ optical transitions conserve m_s, and the $m_s = \pm1$ states have a ∼40% chance of decaying through the singlet states [39], eventually ending up in the m_s triplet states primarily through non-radiative decay. (b) A schematic for a typical confocal microscopy NV experiment.

The ISC decay channel through the singlet states is largely non-radiative, and the $m_s = \pm1$ sublevels fluoresce less brightly than the $m_s = 0$ state. Thus, NV experiments use optical illumination to optically pump the NV centers to initialize them and to read out their m_s final states. Figure 1.4b shows a typical NV confocal microscopy setup. The pump light is focused onto the diamond with a lens, and the fluorescence is collected with the same lens and measured with a photodetector.

The difference in fluorescence intensity between $^3A_2$ magnetic sublevels allows us to measure the transition frequencies between them, which we use for sensing. As shown in Fig. 1.5, the magnetic sublevel transition frequencies depend on parameters such as magnetic field and temperature, which we can measure by determining the transition frequencies. One way to do this is called optically-detected magnetic resonance (ODMR), a variant of electronic paramagnetic resonance (EPR). Although the NVs are optically pumped to the $m_s = 0$ "bright" sublevel, a microwave field resonant with the $^3A_2$ sublevel resonances will drive transitions between magnetic sublevels, removing NV population from the $m_s = 0$ sublevel, spoiling the optical pumping and reducing the fluorescence intensity. Figure 1.6 shows an example spectrum. By monitoring the $^3A_2$ sublevel transition frequencies with ODMR, we can extract the NV local conditions and use them as sensors.

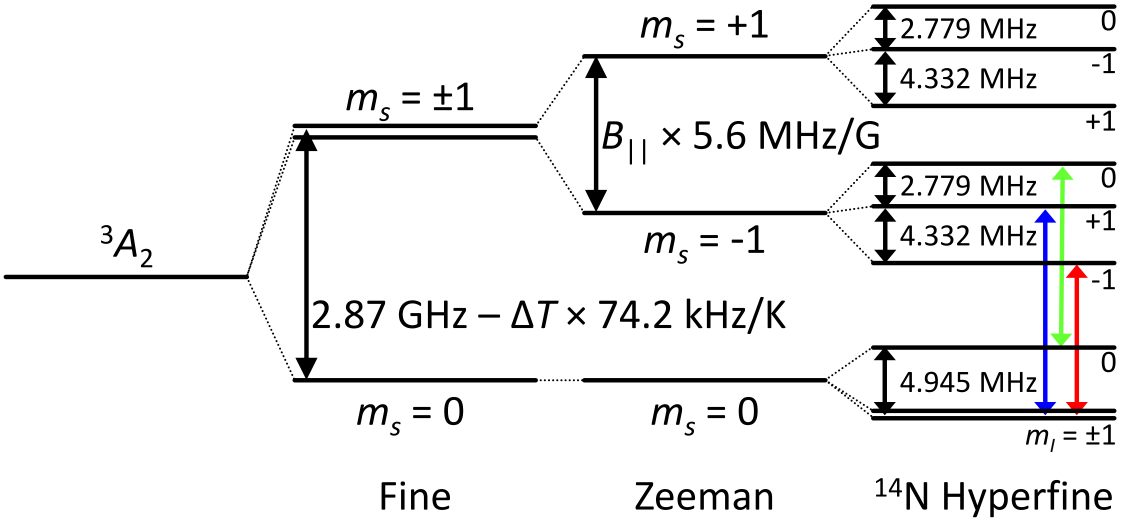

Figure 1.5: The NV $^3A_2$ fine, Zeeman, and ^{14}N hyperfine structure. The hyperfine structure splits the $m_s = 0$ to ±1 transitions into three transitions separated by 2.166 MHz. Here we assume that B is parallel to NV z-axis, and we leave out electric field, strain, and nuclear Zeeman terms (307.7 Hz/G gyromagnetic ratio) [40, 41].

1.2 NV sensing and quantum information

The NV ground-state Hamiltonian

We can itemize different contributions to the NV $^3A_2$ Hamiltonian in the following way (in frequency units) [5]:

- The fine structure (electronic spin-spin interaction) is DS_z^2, where D is the zero-field splitting (∼2870 MHz at room temperature) and S_x, S_y, S_z are the dimensionless spin-projection operators (spin 1). At room temperature, D changes by −74.2 kHz/K due to diamond lattice expansion [6, 42].

- The Zeeman interaction term is $\gamma\vec{B}\cdot\vec{S}$, where $\gamma = 28$ GHz/T is the gyromagnetic ratio and $\vec{B}$ is the magnetic field.

- The Stark interaction term is $d^{\parallel}E_zS_z^2 - d^{\perp}[E_x(S_xS_y + S_yS_x) + E_y(S_x^2 - S_y^2)]$, where $d^{\parallel} =$ 3.5 mHz m/V and $d^{\perp} = 0.17$ Hz m/V are the parallel and perpendicular components of the $^3A_2$ electric dipole moment and $\vec{E}$ is the electric field. In addition, crystal strain (due to external pressure or lattice imperfections) can be written as an effective electric field.

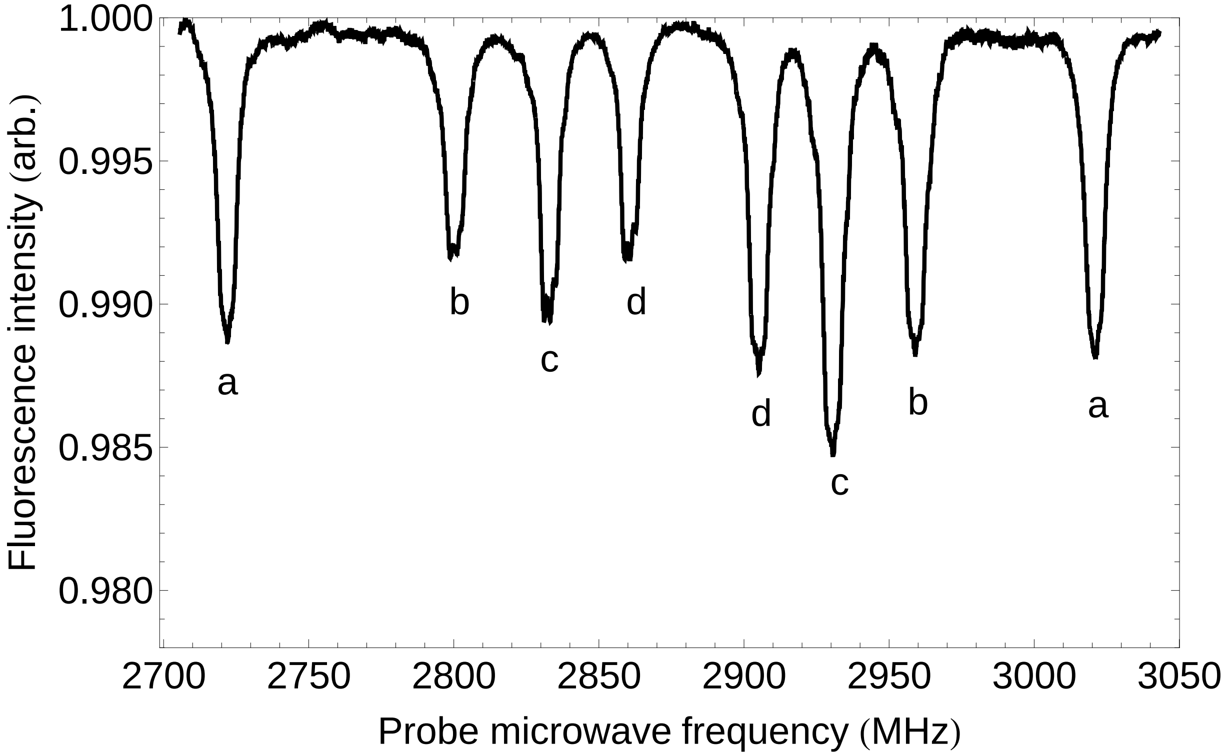

Figure 1.6: An example ODMR plot with a magnetic field $\vec{B}$ in an arbitrary direction. Each of the four NV orientations (labeled a-d) has a different magnetic field projection along its quantization axis, leading to eight ODMR dips in fluorescence (which I refer to as "ODMR peaks"), with two for each NV orientation. All four orientations are degenerate when $\vec{B}$ is along the diamond [100] direction, giving rise to two ODMR peaks. When $\vec{B}$ is along the [111] direction, it is aligned with one of the NV orientations, and the ODMR frequency shift is linear with B, while the other three NV orientations are degenerate, resulting in four ODMR peaks. Similarly, when $\vec{B}$ is along the [110] direction, the four orientations are pairwise degenerate, also resulting in four ODMR peaks.

By measuring the $^3A_2$ resonance frequencies, we can extract the temperature, magnetic field, electric field, and pressure the NV experiences.

Furthermore, if the nitrogen nucleus is ^{14}N (99.6% natural abundance, nuclear spin 1), this introduces further splittings shown in Fig. 1.5 [40]. The $^3A_2$ resonances split into three hyperfine peaks, one for each ^{14}N nuclear state. Neighboring ^{13}C nuclei (nuclear spin 1/2) also have a hyperfine interaction, depending on their location in the lattice relative to the NV [43].

Magnetic sensitivity analysis

Ignoring spin-squeezing, which allows sensing beyond the standard quantum limit, the sensitivity of an NV electron-spin-based magnetometer is [44]

$$\Delta B \approx \frac{1}{\gamma\sqrt{NT_2^* t}}, \tag{1.1}$$

where $\gamma = 28$ GHz/T is electron gyromagnetic ratio, N is the number of NV centers interrogated, T_2^* is the inhomogeneously-broadened transverse spin relaxation rate, and t is the experiment duration. With typical parameters for confocal microscopy experiments with a high-density HPHT diamond sample ($N = 4 \times 10^9$ when interrogating a cylindrical diamond volume with 5 µm radius, 300 µm depth, and 1 ppm $= 1.76 \times 10^{23}$ NVs / m^3; $T_2^* = 300$ ns) we estimate 1 pT/$\sqrt{\text{Hz}}$ as the standard quantum limit for sensitivity. A best-case sensitivity, where we interrogate all of the NVs in a 2 × 2 × 0.3 mm diamond sample, is 3 fT/$\sqrt{\text{Hz}}$, which is comparable to the sensitivity achievable with with vapor cell magnetometers. Similarly, the spin-projection-limited sensitivity for an NV AC magnetometer (implemented with quantum lock-in decoupling schemes described in Chapter 4) is

$$\Delta B \approx \frac{\pi}{2\gamma\sqrt{NT_2 t}}, \tag{1.2}$$

where T_2 is the transverse spin relaxation time for the particular decoupling sequence [4]. The NV T_2 can often be extended to ~300 µs when decoupled from the inhomogeneous magnetic environment, meaning the spin-projection-limited sensitivity to AC magnetic fields is improved from 1 to 0.03 pT/$\sqrt{\text{Hz}}$.

In practice, the NV sensitivity is instead limited by other noise sources (such as photon shot noise or technical noise), which dominate the NV spin projection noise. Following Fig. 1.7, if we monitor the NV fluorescence at a microwave frequency where the $m_s = 0$ to $+1$ ODMR peak slope is greatest, the change in transition frequency is proportional to the change in fluorescence intensity,

$$\Delta f \approx \frac{1}{\alpha}\Delta F. \tag{1.3}$$

Here, f is the ODMR center frequency, $\alpha \approx \frac{N_0 - N_{+1}}{\Gamma}$ is the maximum slope of the ODMR peak, $F \approx \frac{N_0 + N_{+1}}{2}$ is the fluorescence intensity, N_0 and N_{+1} are the fluorescence intensities for the $m_s = 0$ and $+1$ states, and Γ is the ODMR peak FWHM (which can be inhomogeneously broadened and microwave power broadened). The uncertainty in f is

$$\delta f \approx \frac{\partial f}{\partial F}\delta F = \frac{1}{\alpha}\delta F. \tag{1.4}$$

We can define $p = \frac{N_{+1}}{N_0}$ as the fractional fluorescence intensity for the $m_s = +1$ state, which yields $\delta F = \frac{1+p}{2}\delta N_0$, or

$$\delta f \approx \frac{\Gamma}{N_0(1-p)}\frac{1+p}{2}\delta N_0. \tag{1.5}$$

If the magnetometer is photon shot-noise-limited, then $\delta N_0 = \sqrt{N_0}$. Converting f to B with the NV gyromagnetic ratio γ and ignoring the multiplicative constants of order 1, we get

$$\delta B \approx \frac{\Gamma}{\gamma\sqrt{N_0}}. \tag{1.6}$$

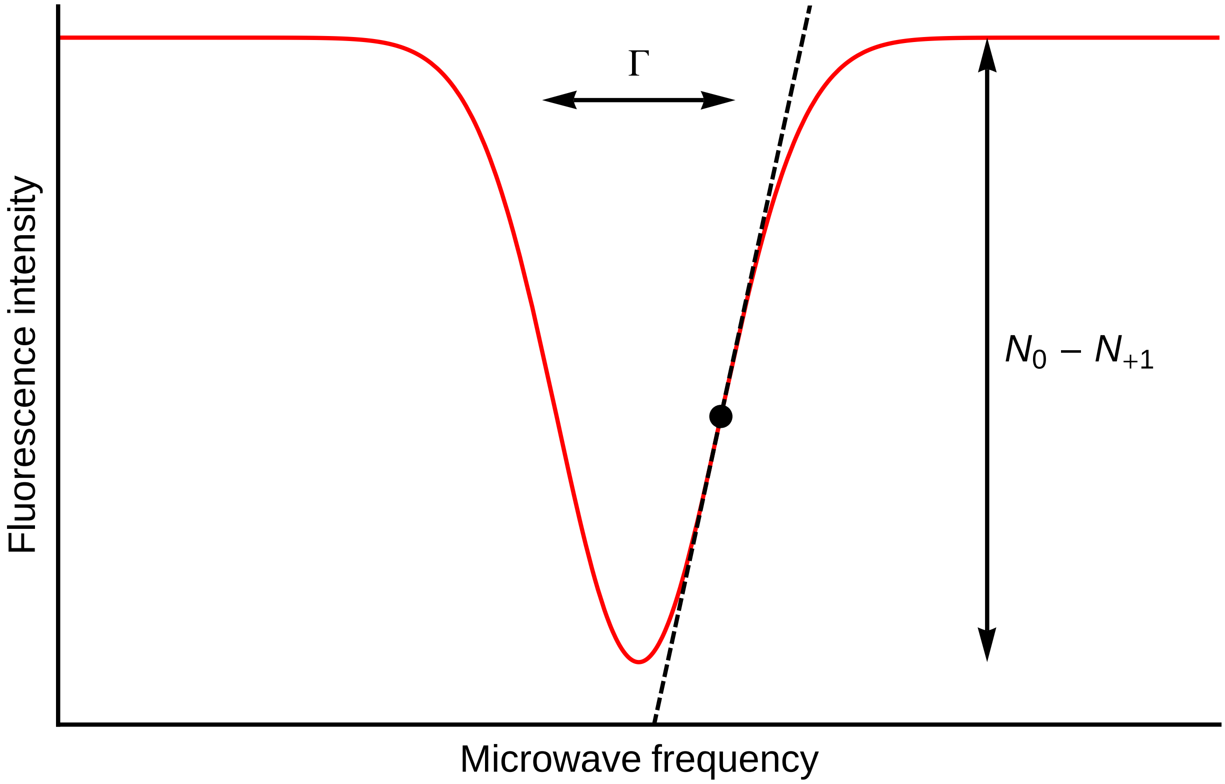

Figure 1.7: A plot illustrating the photon shot noise ODMR sensitivity analysis. The ODMR peak has a FWHM of Γ, an fluorescence difference of $N_0 - N_{+1}$, and a maximum slope of $\sim \frac{N_0 - N_{+1}}{\Gamma}$. If we measure NV fluorescence on the slope of the ODMR peak, changes in magnetic field due to changing magnetic field are proportional to changes in NV fluorescence.

Photon shot noise limits the NV sensitivity to ∼0.1 nT/$\sqrt{\text{Hz}}$ as demonstrated experimentally [45, 46]. Unfortunately, the photon detection efficiency is often $\lesssim$0.1%, making photon shot noise the limiting factor for magnetic sensitivity by many orders of magnitude (assuming laser intensity noise, polarization noise, photodiode dark current noise, and other noise sources are negligible). Furthermore, interrogating the entire diamond volume is difficult because of the optical pump power required. To excite all NVs in a 1 ppm 2 × 2 × 0.3 mm diamond (2×10^{14} NVs) at the saturation intensity (one absorption every 10 ns, the ^3E lifetime), we would need 7.5 kW of 532 nm pump light, which is ∼1000 times more power than what a few-watt continuous-wave pump laser can provide.

NV AC magnetometeters use microwave pulse sequences to accumulate spin precession from a synchronized AC magnetic field (described more thoroughly in Chapter 4). These pulse sequences (Hahn echo, CPMG, XY, Walsh, concatenated, and composite) are borrowed from NMR, and they decouple the NVs from the environment except for magnetic fields the sensing frequency and higher harmonics. This decoupling improves the T_2^* coherence time to a longer time T_2, and also filters out magnetic noise at most frequencies (like a lock-in amplifier). The pump laser is switched off during the pulse sequence to avoid reinitializing the NVs and spoiling the coherence, meaning that the photon shot noise suffers from a reduced illumination duty cycle compared to an experiment with continuous illumination.

NV sensing applications

NV sensors are best suited for sensing applications requiring high spatial resolution. Since NV sensors work in a wide range of conditions (including ambient conditions), this often allows us to put the NVs close to the system being measured (where the fields are stronger). While many experiments demonstrate NV sensitivity or study a well-known target system, perhaps the most exciting projects are those that use NV sensing in a new field. NV widefield magnetic imaging was used to study 50 nm ferromagnetic grains in magnetotactic bacteria, 10-100 μm grains in meteorites, and immunomagnetically-labeled cancer cells [47–49]. Other NV biology experiments have measured the temperature in a living cell and sensed the magnetic field from a firing neuron [15, 46]. NV AFM experiments have examined domain walls and vortices in magnetic thin films [50, 51]. Near-surface NVs can sense paramagnetic and nuclear spins external to the diamond to yield single-molecule NMR (and soon MRI will yield spatial information as well) and paramagnetic spin detection and identification [52, 53]. Finally, NVs are a promising tool for detecting the Meissner effect and magnetic flux vortices in superconductors, including superconducting boron-doped diamond [54, 55].

As described in Chapter 4, NV centers can sense paramagnetic and nuclear spins a few nanometers away, which we observe as reduced NV electronic T_1 or T_2. T_1 relaxation is better suited for sensing GHz-frequency magnetic noise, which lends itself to sensing paramagnetic spins (substitutional nitrogen defect centers, Gd^{3+}, Mn^{2+}, and other NV centers) and magnetic Johnson noise [53, 56–59]. T_2 relaxation is useful for sensing magnetic nuclei (such as ^{1}H, ^{13}C, ^{19}F, and ^{31}P) [60–62]. The eventual goal is to achieve single-molecule MRI, where a nearby NV can sense nearby magnetic nuclei and can distinguish their positions, allowing us to reconstruct the structure of a complex protein. Related schemes for sensing magnetic spins include double electron-electron resonance (DEER) and correlation spectroscopy [60, 63, 64].

While NV sensing borrows many techniques from NMR, NVs are also useful for nuclear spin polarization, which is one of the underlying challenges of NMR. The NV electronic states can be optically polarized, and the polarization can be transferred to nearby nuclei (^{14}N of the NV and ^{13}C in the lattice), often more at reasonable magnetic fields than conventional NMR ($\sim$50 mT compared to $\sim$1-10 T) [65]. The eventual goal is to polarize nuclei using NVs, then transfer the polarization to other nuclei (perhaps protons in water) for diagnostic

MRI. Hartmann-Hahn techniques can also transfer NV polarization to a paramagnetic or nuclear spin bath [66, 67].

NV quantum information

Nuclear spins (^{14}N of the NV or a nearby ^{13}C nucleus) can be initialized, entangled, and read out using NV centers [9, 10, 68]. These are among the candidate technologies for implementing a scalable quantum computer, with other technologies including superconducting qubits, photons, trapped ions, cold atoms, electromagnetically induced transparency, quantum dots, and other crystal defects (^{29}Si or ^{31}P in silicon, silicon-vacancy centers in diamond, defects in silicon carbide, and rare-earth ions) [69–78]. NV quantum information experiments have many similar technical challenges as NV sensing experiments, including preserving qubit superpositions and achieving fast final-state readout with high fidelity.

Both NV sensing and quantum information benefit from many of the same technical improvements. Dynamical decoupling pulse sequences extend T_2, improving sensitivity and qubit coherence time [79]. Improved light collection and readout fidelity also enhances sensitivity and boosts the entanglement success rate for fluorescence photons from different NVs [80, 81]. Quantum error correction protects qubits from decoherence and enables Heisenberg-limited sensitivity scaling [82–84]. Quantum nondemolition measurements allow qubit initialization and enable us to store many NV electronic-state measurements in a long-lived nuclear state without reading them out individually [85, 86].

Figure 1.8 shows an example Rabi oscillation experiment in an NV ensemble. By applying microwave pulses, we a can create arbitrary superpositions between NV electronic sublevels. We can also read out a nuclear sublevel using pulsed ODMR (described in Fig. 1.8b, where the pulse duration is a π-pulse). This enables a CNOT gate (an essential component in quantum computing), where the nuclear state controls whether electronic π-pulse is successful [9].

More traditional quantum information experiments are another branch of NV work, where the eventual goal is building an NV quantum computer or simulator. Quantum information experiments use single NV centers often at cryogenic temperature, and include

- the NV electronic spin as the “ancillary” qubit (used for initialization and readout).
- the NV ^{14}N or nearby ^{13}C nuclear spins as the “system” qubits (used for long-term storage).
- single (indistinguishable) $^3E \to {}^3A_2$ ZPL photons (used to entangle different NV electronic spins).
- $^3E \to {}^3A_2$ photons (used for NV electronic spin readout).

In addition to manipulating the NV electronic state with an AC magnetic field, a second AC field (tuned to the nuclear resonance frequency) can drive Rabi oscillations between nuclear states to create arbitrary superpositions. Cryogenic single-NV experiments have

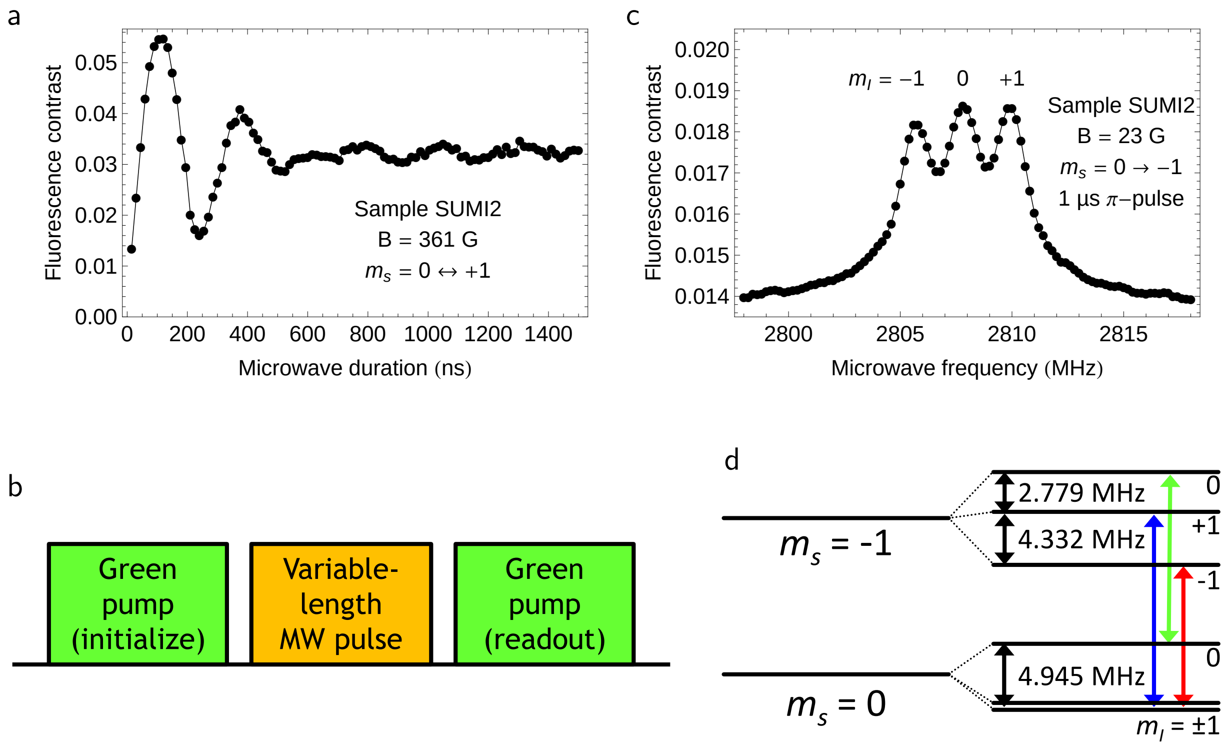

Figure 1.8: (a) Rabi oscillations in an NV ensemble. The microwaves were applied by a microwave wire near the illuminated NVs, and the oscillations decay away partly because the spatially-inhomogeneous magnetic fields at different distances from the wire cause a distribution of NV Rabi frequencies. (b) The pulse sequence used for measuring Rabi oscillation. (c) A pulsed-ODMR measurement. After determining the microwave π-pulse duration on resonance, we apply a π-pulse with variable frequency before reading out the final state. Here we see the three ^{14}N hyperfine peaks (separated by 2.166 MHz [40]). (d) The transitions shown in (c). By choosing the appropriate microwave frequency, we can implement a pulsed-ODMR CNOT gate using the ^{14}N spin as the control bit.

achieved high-fidelity single-shot readout, nuclear-state initialization by repeated measurement, and nuclear qubit entanglement and teleportation between nuclei in different diamonds [10, 68, 81]. Other demonstrations include a 1 second ^{13}C T_2^* at room temperature, multi-qubit quantum error correction, quantum gates, and a planned Bell's inequality test [9, 82–84, 87, 88]. Eventually, this work may extend to larger-scale devices, such as a fluorine-terminated diamond surface as a NV-controlled quantum simulator or implementing waveguides to optically entangle qubits in the same diamond [89, 90].

Like its competing technologies, NV quantum information is still limited. One problem is the slow experiment rate due to poor photon collection efficiency ($\sim$20%) and a small (few-percent) likelihood of an NV emitting a ZPL photon; the experimenters in Ref. [68]

attempted to generate entangled nuclei every 50 μs, but only succeeded every ten minutes. Though there are plans to implement quantum networks with NV dipolar coupling and other means, at most two NV centers were used for entanglement thus far. Despite the promise of being able to build scalable quantum networks and taking advantage of fabrication techniques for a photonics-based implementation, there is still much work to be done before NV quantum technology catches up to more established competitors. The following section further investigates the benefits and drawbacks of NV sensing and quantum computing.

1.3 Advantages and limitations

Advantages

As sensors, NV centers have unprecedented spatial resolution. Most sensors have a spatial resolution roughly as big as the device size (as small as a 1 mm^3 vapor cell, 100 nm diameter nanoSQUID magnetic flux loops, 25 nm with MRFM, 50 μm with a BEC, and 0.1-1 μm with MEMS) [91–95], the NV electronic wave function is constrained to a few atomic lattice sites (∼0.5 nm) [96] and spatial resolution is limited by optical resolution. The spatial resolution can be $\lesssim$1 μm with diffraction-limited optics, while superresolution techniques can distinguish individual NV centers separated by 15 nm [97, 98]. Compared to more established technologies, where incremental improvements become harder to achieve, NV sensing is quite new in comparison, as it has only been pursued for the last decade. Although the absolute sensitivity is still worse than that of other systems (0.1-1 $\mathrm{nT}/\sqrt{\mathrm{Hz}}$), the spin-projection-limited sensitivity is much better (as good as $\mathrm{fT}/\sqrt{\mathrm{Hz}}$), and the promise of improving sensitivity to the spin-projection-noise limit motivates technical innovation. Finally, since NV centers can have four orientations in the diamond, we can extract vector information about the magnetic field, electric field, or compression from an NV ensemble (all in one device).

Other magnetic sensing technologies with better sensitivity require specific environments (such as low temperature, near-zero magnetic field, and ultra-high vacuum). Isolating the sensor in a vacuum or cryogenic environment separates it from the system being sensed, and with the additional distance comes reduced spatial resolution and magnetic field. NV sensors are more versatile and robust, allowing us to compensate for the lower magnetic sensitivity by putting the NV close (nanometers) away from the magnetic field source, where the field is stronger. While some sensitive magnetometers can saturate or can have poor dynamic range and bandwidth, NV magnetometers work at arbitrary (zero to tesla) DC magnetic fields and MHz AC magnetic fields (limited by the maximum Rabi frequency achievable). Enhanced dynamic range (beyond 2π phase accumulation) is also possible for NV electronic and nuclear magnetometry [99, 100].

The most basic NV experimental setup is simple compared to other high-sensitivity magnetometer setups (Fig. 1.4b). The ${}^3A_2 \rightarrow {}^3E$ PSB is broad, meaning pump laser frequency accuracy and stability are less important than in atomic physics experiments (though the 637 nm pump wavelength stability is important if addressing narrow ZPL transitions). Often the pump laser is a common frequency-doubled 532 nm Nd:YAG laser, and high polarization and frequency stability are usually unnecessary. The pump laser intensity stability is important, but intensity fluctuations can be canceled out up to ∼10-100 kHz. Most NV experiments are done at room temperature and do not require cryogens or vacuum. Collecting a large fraction of the NV fluorescence is challenging, the fluorscence intensity is often visible by eye (up to ∼10 μW in high-density diamond samples). Furthermore, NVs are easy to initialize and read out (with optical pumping and fluorescence readout) compared to cold atom or trapped ion setups. These simplifications mean that researchers spend less time engineering the experiment and more time on NV science, and allows a single researcher to build and operate several setups instead of having to share one setup with the rest of the research group. These technical advantages make NV centers easy to work with and allow for rapid prototyping and troubleshooting.

Many advantages come from the diamond material properties themselves. Fluorescent indicators used in biology (reactive dyes and fluorescent proteins) can have their fluorescence intensity quenched after being pumped into a metastable state (photobleaching), limiting the photon-noise sensitivity. Diamond is chemically inert and biocompatible; living cells can rest on top of a diamond substrate and can uptake nanodiamonds without being poisoned. Furthermore, diamond can withstand extreme conditions, and NV centers continue to work at these extremes [7, 8]. NVs have long relaxation times at room temperature because of the strong carbon-carbon bonds in diamond, leading to a high Debye temperature (∼2200 K [12]). This means there are few phonon excitations at room temperature, which contribute to spin decay [56]. For comparison, ^{31}P in silicon, which generated interest as a potentially scalable qubit candidate, needs dilution refrigeration and uses spintronic initialization and readout for individual defects (with deposited wires), yet has comparable cryogenic electronic T_2 to the NV center at room temperature [75]. Finally, with improvements in fabrication and implantation technology, we may be able to deterministically place NV centers in a diamond sample, then entangle them with dipole-dipole interactions or optically with waveguides connecting them. This could lead to a scalable quantum computer, though much development is still necessary.

Ongoing challenges

Despite their advantages, NV centers have many technical challenges to overcome. Diamond has a high refractive index ($n = 2.42$), so most of the fluorescence light emitted from an NV in a flat diamond is not collected since much of the light undergoes total internal reflection. This means that despite the small spin-projection noise, NV experiments are instead limited by photon shot noise (or other noise sources), which is many orders of magnitude larger. Despite the outstanding spatial resolution and low spin-projection noise, NV sensors have worse sensitivity than more established sensors due to photon shot noise.

Inhomogeneous broadening is another problem; local magnetic fields and crystal strains broaden the ODMR resonances, reduce T_2^*, and diminish sensitivity. The best T_2^* at room temperature reported for a single NV (470 μs) and for an NV ensemble (30 μs) are much shorter than the longest ensemble $T_2 = 2$ ms [9, 101, 102]. The microwave field used to drive NV Rabi oscillations may also have a spatial gradient, causing NVs to have location-dependent Rabi frequencies (Fig. 1.8a). Using high-density samples with many NVs may improve ensemble sensitivity, but this comes at the cost of more broadening from radiation damage, nitrogen defects, and crystal strain. For comparison, atomic frequency standards and sensors are independent of the particular device or sample (as long as we understand the systematics), but while every atom is the same, every NV center is different. Diamond samples differ in crystal growth, irradiation, surface treatment, NV-surface distance, and nearby impurities. This complicates NV sensor development because some goals are only achievable in certain samples, and we must invest effort learning how to make good samples reproducibly. Furthermore, it is difficult to quantify sample contents, since the interrogation methods are often indirect. For example, burning a diamond sample yields the nitrogen concentration, but not what form the nitrogen was in, as it could be distributed over NV^-, NV^0, substitutional nitrogen (P1), and other nitrogen-containing defects.

Compared to the preferred atoms and ions used for other atomic physics experiments, which have well-understood basic properties (such as electronic configurations, frequencies, and electric dipole moments), NV centers are poorly understood. The ${}^3A_2 \leftrightarrow {}^3E$ and ${}^1E \leftrightarrow {}^1A_1$ ZPL energies are known, but the relative triplet-singlet energies and their energies compared to the diamond valence and conduction bands are not known directly [31, 103, 104]. The optical pumping mechanism, which all NV experiments take advantage of for initialization and readout, is not completely understood, since it requires a triplet-singlet mixing through the excited vibrational levels. Recent theoretical models for the NV electronic states disagree on the NV state labels and predicted energies, which reflects how challenging such calculations are [26, 27, 29, 34, 105–107]. Four of the six anticipated electronic states are experimentally confirmed, and theorists disagree on the energies of the remaining two. Although three groups calculated the ${}^3A_2$ and ${}^3E$ phonon modes [108–110], this calculation has not yet been extended to the singlet states because of limitations of the density functional theory (DFT) models for the NV electronic states.

The NVs in an ensemble have transverse strain inhomogeneity (up to ∼10 MHz). While we usually use a bias magnetic field to make the Zeeman term dominant, the transverse strain is dominant near $B = 0$, which makes magnetometry at low field challenging. NVs are simultaneously a magnetometer and a thermometer. This means temperature drifts can naively be interpreted as changes in magnetic field (and vice versa). We can mitigate this problem by querying both $m_s = 0 \leftrightarrow \pm 1$ transitions to cancel undesired magnetic or temperature drifts [7, 101, 111, 112].

The four NV orientations can yield vector magnetic field information, but the preferred NV z-axis means that a magnetic field with a transverse component cause the magnetic sublevels to no longer be good quantum numbers, which reduces the optical pumping efficiency [113]. The Zeeman splitting is nonlinear for an off-axis $\vec{B}$, and while we may select one NV orientation with a bias magnetic field to make a linear magnetometer, the three non-aligned orientations contribute background fluorescence that adds to the photon shot noise. Finally, although near-surface NVs are best for sensing external magnetic fields, the NV properties (T_2^* and photostability) deteriorate as the depth decreases because of magnetic noise from unbonded electrons at the diamond surface (∼5-10 nm) [20].

NV centers have drawbacks when used as single-photon sources or qubits. Pump-laser illumination causes fluctuating electric fields through defect ionization and charge trapping, perturbing the ${}^3A_2 \rightarrow {}^3E$ ZPL wavelengths in a phenomenon called spectral diffusion [114]. This complicates creation of NV entanglement by interfering indistinguishable photons, as the emitted ZPL photon wavelengths can drift. Furthermore, most (∼97% at 10 K [37]) of the ${}^3E \rightarrow {}^3A_2$ fluorescence is in the PSB part of the emission spectrum, meaning most photons emitted by different NVs are distinguishable. Together with poor collection efficiency, this reduces the efficiency for generating indistinguishable ZPL photon pairs and NV entanglement.

Addressing these challenges

Researchers are pursuing a variety of solutions to overcome the challenges listed above. High-numerical-aperture microscope objectives, index-matching immersion oil, and solid immersion lenses improve the light collection efficiency. Another approach is to attach detectors on the sides of the diamond sample, which improved the photon detection efficiency from a few percent to ∼40% in one experiment [45]. NVs embedded in diamond nanopillar waveguides can also direct the emitted light in a preferred direction [115].

Another way to improve the photon shot noise is to measure ODMR frequencies by probing the 1042 nm ${}^1E \rightarrow {}^1A_1$ absorption transition. While the ${}^3E \rightarrow^3 A_2$ fluorescence intensity decreases when the microwave frequency is resonant with an NV transition, the microwaves also put more NV population in the metastable ${}^1E$ state, making the diamond more opaque to 1042 nm probe light. This allows us to reduce the photon shot noise by probing 1042 nm absorption with an arbitrarily large number of probe photons and sensing changes in diamond opacity instead of NV fluorescence. However, the metastable ${}^1E$ state requires a large pump intensity to populate, and the ${}^1E \rightarrow {}^1A_1$ absorption cross section is weaker than the ${}^3A_2 \rightarrow {}^3E$ cross section (3.1×10^{-21} m^2 at 532 nm compared to 4×10^{-22} m^2 at 1042 nm) [116, 117]. These problems can be solved by enhancing the 1042 nm absorption path length, either with an optical cavity, a fabricated waveguide, or by total internal reflection [24, 118–120].

Other approaches use $\mathrm{NV}^- \rightarrow \mathrm{NV}^0$ photoionization to measure the NV^- m_s state. One scheme uses m_s-dependent photoionization to convert the NV^- spin state to a charge state, which is then evaluated with 594 nm light [121]. This improves the contrast and photon shot noise, though at the expense of a slower experiment repetition rate. Photocurrent readout with electrodes or graphene is another promising option [122, 123].

Diamond samples grown by CVD along the [100] face contain naturally-forming NVs aligned along two of four possible orientations [124]. Although the NV density is low, this can reduce background fluorescence from the non-aligned NVs. This improvement also works for diamond grown along the [111] surface, where nearly all of the NVs have form along the

[111] direction [125, 126]. Different diamond surface treatments can improve the near-surface NV photostability, coherence time, and yield. Furthermore, putting the NVs near the surface (and increasing the field strength from surface magnetic spins) can outweigh the shorter in T_2^* for near-surface NV sensing [20, 127].

The NV single-photon and quantum information applications also have had recent improvements. Before entangling two NVs by interfering identical ZPL photons, experimenters first query the two ZPL wavelengths, then apply a feedback electric field with nearby electrodes to bring the NVs into resonance [128]. An NV placed inside a resonant diamond photonic crystal can improve the fraction of NV fluorescence in the ZPL, accelerate the fluorescence decay rate by Purcell enhancement, and direct the emitted light to a nearby optical fiber. Furthermore, the NV single-photon source and quantum information investigations have inspired related work on new defects, such as defects in silicon carbide and the silicon-vacancy (SiV) defect in diamond offer improvements in ZPL fluorescence intensity and immunity to spectral diffusion [76, 129].

1.4 Overview of work presented

As described above, it is an interesting time for developing new NV applications and improving sensitivity. However, since our understanding of NV basic properties is limited, it is important to investigate NV basic properties to enable unanticipated applications and research directions. The following chapters include descriptions of three topics motivated by studying NV basic properties and applications. Chapter 2 describes an experiment that searches for the predicted $^1E'$ state and examines the $^1E \rightarrow {}^1A_1$ phonon sideband. Chapter 3 explains how saturation spectroscopy, often used to remove inhomogeneous Doppler broadening in hot atomic vapors, can remove inhomogeneous broadening in the $^3A_2$ magnetic sublevel transitions, leading to improved thermometry and a way to understand the inhomogeneous broadening mechanisms. Chapter 4 explains how we can use NV T_1 relaxation to sense resonant paramagnetic impurities (in this case, spin-1/2 substitutional nitrogen defect centers) and describes how T_1 depends on temperature, magnetic field, and NV density. Chapter 5 includes an overview and details on ongoing experiments.

Chapter 2

NV Singlet Spectroscopy

NV centers in diamond have generated much interest for use in quantum technology. Despite the progress made in developing their applications, many questions about the basic properties of NV centers remain unresolved. Understanding these properties can validate theoretical models of NV, improve their use in applications, and support their development into competitive quantum devices. In particular, knowledge of the phonon modes of the $^1A_1$ electronic state is key for understanding the optical pumping process. Using pump-probe spectroscopy, we measured the optical absorption of the phonon sideband for the $^1E \to {}^1A_1$ electronic transition in the NV center. From this we calculated the $^1E \to {}^1A_1$ one-phonon absorption spectrum and found it to differ from that of the $^3E \to {}^3A_2$ transition, a result which was not anticipated by previous group-theoretical models of the NV electronic states. We identified a high-energy 169 meV localized phonon mode of the $^1A_1$ level.

This work was published in Physical Review B in 2013 [117].

2.1 Introduction

Figure 2.1a shows a simplified NV energy-level diagram as confirmed by experiment. The triplet-triplet ($^3A_2 \leftrightarrow {}^3E$) and singlet-singlet ($^1E \leftrightarrow {}^1A_1$) energy differences are known to be 1.945 eV (637 nm) and 1.190 eV (1042 nm), respectively [28, 29, 105, 130]. However, where these energy states lie with respect to the diamond valence and conduction bands is only known indirectly, as are the triplet-singlet ($^3A_2 \leftrightarrow {}^1A_1$ and $^1E \leftrightarrow {}^3E$) energy differences [31, 103]. Theoretical calculations predict the existence of additional energy states ($^1E'$ and $^1A_1'$), but disagree on their energies (see Refs. [26, 27, 34, 131, 132]] and references therein). Prior experiments and *ab initio* calculations studied the phonon sidebands (PSBs) for the $^3A_2 \to {}^3E$ and $^3E \to {}^3A_2$ transitions [108, 109, 130, 133, 134]. The $^1E \to {}^1A_1$ and $^1A_1 \to {}^1E$ PSBs have not been studied theoretically, and only the $^1A_1 \to {}^1E$ transition had been measured prior to this work [28, 29, 105].

A more complete experimental picture of NV properties can provide insight for applications and validate theoretical models of NV attributes. The 1042 nm infrared $^1E \to {}^1A_1$

zero-phonon line (ZPL) has been used in an absorption-based magnetometer [119], but using the $^1E \rightarrow {}^1A_1$ PSB instead may be more sensitive depending on the PSB structure and cross section. In addition, most NV experiments take advantage of an optical pumping mechanism (which involves the $^1A_1$ excited vibrational states) that drives electrons to the $^3A_2$ $m_s = 0$ state. Therefore, knowledge of the $^1E \rightarrow {}^1A_1$ PSB could improve infrared magnetometry and optical pumping schemes. Moreover, as the NV center develops into a mature quantum system, it is important to know the properties of the singlet states to inspire confidence that we understand this system.

We attempt to fill the gaps in the knowledge of NV properties by measuring the $^1E \rightarrow {}^1A_1$ PSB and searching for previously unobserved transitions. Finding the $^1E \rightarrow {}^1E'$ ZPL would resolve the disagreement on the predicted $^1E'$ energy. The $^1E \rightarrow {}^1A_1$ PSB yields information about the $^1A_1$ phonon modes, which are also of interest. The spin-orbit interaction mixes the ^3E and $^1A_1$ states, resulting in triplet-singlet intersystem crossing (ISC). This enables spin-dependent non-radiative decay from the nominally ^3E state to the nominally $^1A_1$ state. The ISC rate is comparable to the $^3E \rightarrow {}^3A_2$ spontaneous decay rate [35, 39] and is an important factor in the optical pumping process. Measuring the $^1A_1$ phonon modes could allow the optical pumping mechanism to be modeled more accurately and provide insight on NV spin polarization and readout. Furthermore, the accepted group-theoretical model of NV predicts $^3A_2$ and $^1A_1$ to have the same electronic configuration, meaning they should have the same phonon modes. A comparison between the $^3E \rightarrow {}^3A_2$ and $^1E \rightarrow {}^1A_1$ PSBs should be sensitive to differences between the $^3A_2$ and $^1A_1$ configurations.

In this work, we present measurements of the $^1E \rightarrow {}^1A_1$ ZPL and PSB. We describe the PSB absorption features, including a high-energy (169 meV) localized phonon mode that lies outside the diamond lattice phonon density of states. Comparing the $^1E \rightarrow {}^1A_1$ and the $^3E \rightarrow {}^3A_2$ phonon modes, we find that the $^1A_1$ phonon modes are shifted to higher energies, meaning that proper descriptions of the $^1A_1$ and $^3A_2$ states require corrections to their electronic configurations.

2.2 Experiment and results

In our experiment, we populated the metastable ^1E state using pump-laser light and measured transmission of probe-laser light through a diamond sample containing an ensemble of NV centers (Fig. 2.1 and Fig. 2.2). We determined the probe transmission through the diamond with and without NV centers in the ^1E state. A 532 nm frequency-doubled Nd:YVO$_4$ pump laser beam and a 5 mW supercontinuum probe laser beam (wavelength range 450-1800 nm) were combined on a dichroic beamsplitter and focused with a microscope objective (Olympus LUCPlanFL N 40× PH2, 0.6 numerical aperture) onto a cryogenically cooled diamond sample. The transmitted light was collimated and detected with a spectrometer with ∼1 nm resolution. A chopper wheel modulated the pump light and a computer collected a transmission spectrum each time the pump light was blocked and unblocked. Absorption from ^1E appeared as a difference between the "pump blocked" and "pump unblocked" su-

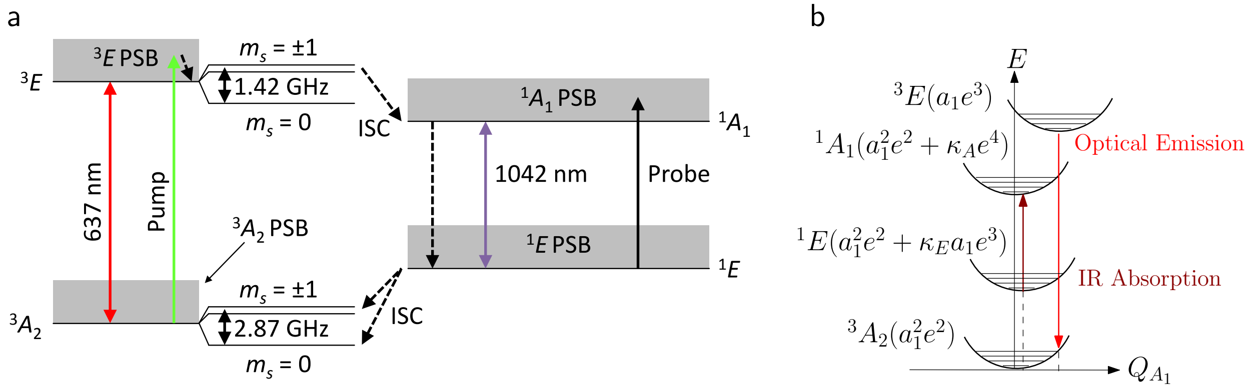

Figure 2.1: (a) The NV energy-level diagram and our pump-probe spectroscopy scheme. The states are labeled by their C_{3v} representations and electron spin multiplicities. Solid arrows are optical and microwave transitions, and dashed arrows are non-radiative transitions. The label "ISC" indicates intersystem crossing, which occurs primarily for the ^3E $m_s = \pm1$ states and is responsible for optical pumping. (b) A configuration coordinate diagram for A_1 phonon modes showing the harmonic nuclear potential wells and phonon energy levels. The configuration for each electronic state is denoted in parentheses, and Q_{A_1} is the normal nuclear coordinate. With no electronic Coulomb repulsion, the $^3A_2$, ^1E, and $^1A_1$ levels are of the $a_1^2e^2$ configuration and the ^3E level is of the a_1e^3 configuration. With Coulomb repulsion included to first order, the ^1E and $^1A_1$ levels couple with the $^1E'$ (configuration a_1e^3) and $^1A_1'$ (configuration e^4) levels, respectively. This coupling is denoted by the parameters κ_E and κ_A.

percontinuum transmitted intensities. In another experiment, we used 912 nm and 1042 nm continuous-wave (cw) lasers as probe sources and replaced the spectrometer with a photodiode.

We focused the pump and probe beams onto the diamond samples to a minimum beam waist smaller than 5 μm. This objective lens is achromatic, which ensures that the pumped NV and probe spatial regions overlap. We used a Janis ST-500 liquid-helium flow cryostat for cooling the diamond sample. Our pump-laser source was a Coherent Verdi-V6, and our cw probe-laser sources included 2 mW of 912 nm light from a Coherent CR 899 Ti:Sapphire laser, 30 mW of 912 nm light from a diode laser (1 nm linewidth), and 1.5 mW of 1042 nm light from an external-cavity diode laser (ECDL). We used a Fianium SC450-2 supercontinuum laser as our broadband probe and an Ocean Optics USB2000+VIS-NIR spectrometer (∼1 nm resolution, optimized for infrared sensing) for detecting transmitted supercontinuum light.

We used the $^3E \rightarrow {}^3A_2$ fluorescence spectrum of a similar diamond sample at 4 K for comparison with our $^1E \rightarrow {}^1A_1$ spectrum. This sample was also illuminated with 532 nm pump light, and the emitted fluorescence was dispersed with a monochromator (0.1 nm resolution) and detected with a photomultiplier with a GaAs photocathode (calibrated with the blackbody spectrum from a 3100 K tungsten bulb). Although we compared spectra from different diamond samples, the spectra from different high-concentration samples are in general consistent.

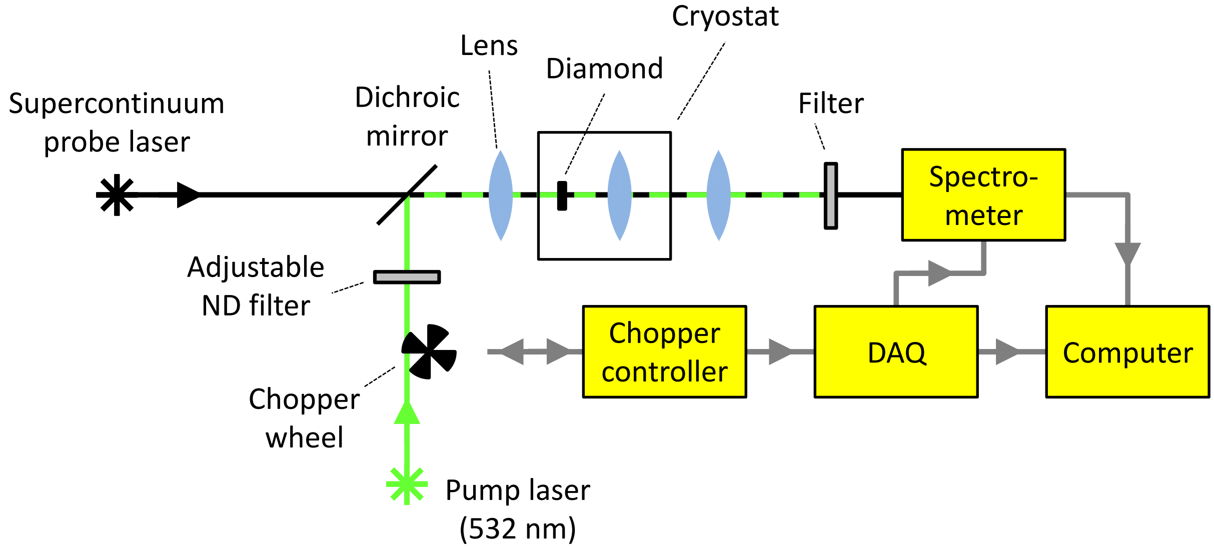

Figure 2.2: The experimental apparatus. The data acquisition device (DAQ) monitors the chopper wheel state and triggers a spectrum acquisition when the pump is blocked or unblocked. The computer collects "pump blocked" and "pump unblocked" transmission spectra.

Figure 2.3a shows the $^1E \rightarrow {}^1A_1$ ZPL and PSB supercontinuum absorption spectrum taken at 10 K with the sample "B8", a synthetic type Ib high-pressure high-temperature (HPHT) diamond with ∼10 ppm NV concentration. The PSB includes narrow absorption lines at 811 and 912 nm and broad absorption features at 872, 922, 931, and 983 nm. In the figure we observe that the 912 and 811 nm lines are 169 meV and 2×169 meV away from the ZPL, respectively. Consequently, we believe the 811 and 912 nm lines are due to a 169.28(4) meV phonon mode and that the other lines are due to a distribution of phonon modes. Figure 2.3b shows the $^3E \rightarrow {}^3A_2$ fluorescence spectrum taken at 4 K with a similar diamond (also ∼10 ppm NV concentration). This PSB has a broader energy range, and has features at 686, 692, and 696 nm. Using these measured spectra and the techniques outlined in Refs. [117, 133, 135], we calculated the $^1E \rightarrow {}^1A_1$ and $^3E \rightarrow {}^3A_2$ Huang-Rhys parameters (0.9 and 3.49, respectively) as well as their one-phonon spectra (Fig. 2.4), which are the rates at which these transitions create one phonon of a given energy. We expect these one-phonon spectra to be comparable, since both come from $E \rightarrow A$ transitions with similar final-state electronic configurations (Fig. 2.1b). The one-phonon spectra show resemblance, and the differences between them are because of electronic Coulomb repulsion corrections to the $^1A_1$ level. These corrections mix the $^1A_1$ level with the higher-energy $^1A_1'$ level. As a result, the $^1A_1$ level contains an admixture of configurations, which results in the difference in the one-phonon spectra [117].

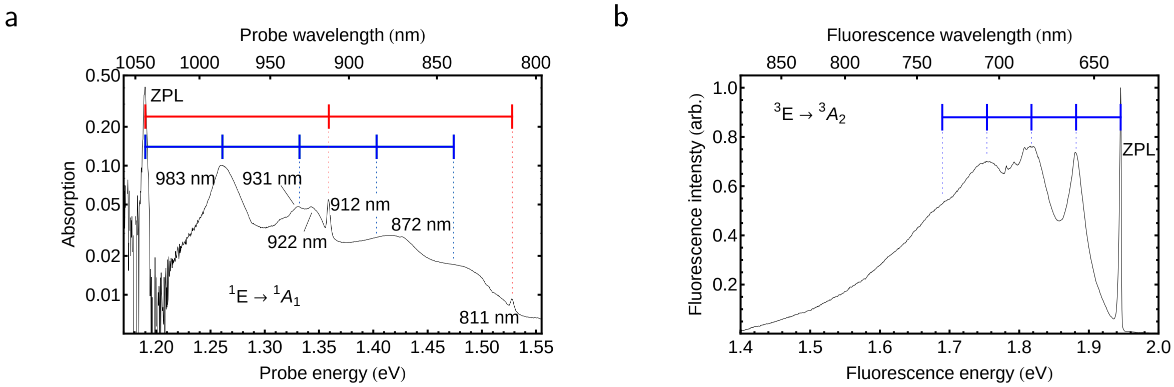

Figure 2.3: (a) The supercontiuum absorption spectrum collected at 10 K for diamond sample B8 using 35 mW of pump-laser light. PSB fluorescence from $^3E \rightarrow {}^3A_2$ is present for wavelengths shorter than 840 nm and has been subtracted out. The vertical ticks indicate the expected PSB absorption energies for 71 and 169 meV phonons, which align with some of the absorption features. (b) The fluorescence spectrum of a similar diamond collected at 4 K. The vertical ticks indicate the expected PSB absorption energies for 64 meV phonons. Although the 686, 692, and 696 nm features are often ignored, they are vital to our comparison of the $^1E \rightarrow {}^1A_1$ and $^3E \rightarrow {}^3A_2$ PSBs, as they give rise to peaks (3)-(5) in Fig. 2.4.

We observed the above $^1E \rightarrow {}^1A_1$ PSB features in several diamond samples, and the absorption was greater in samples with higher NV concentration. The $^1E \rightarrow {}^1A_1$ absorption should increase with pump power and saturate when the pumping rate becomes comparable to the ^1E decay rate. The absorption at room temperature increased linearly with pump power (up to 60 mW focused to a minimum beam waist smaller than 5 μm), indicating that the ^1E population was not saturated. However, the absorption at 10 K saturated at $\sim$15 mW. This saturation is likely due to the prolonged ^1E lifetime at cryogenic temperature [28]. Introducing a static transverse magnetic field to the samples improved the absorption contrast by a few percent. This is because the Zeeman interaction mixes the triplet spin sublevels, which spoils the optical pumping to $m_s = 0$ and increases the ^1E population.

We did not detect a $^1E \rightarrow {}^1E'$ ZPL in the 480-1100 nm range of the supercontinuum transmission spectrum, which means this transition lies outside of this range or was too weak to detect. This wavelength span was limited by the spectrometer.

$^1E \rightarrow {}^1A_1$ zero phonon line cross section estimate

Using experimental decay-rate and pump-laser absorption cross section parameters [39, 116], we constructed a rate-equation model to estimate the fraction of NV centers in the

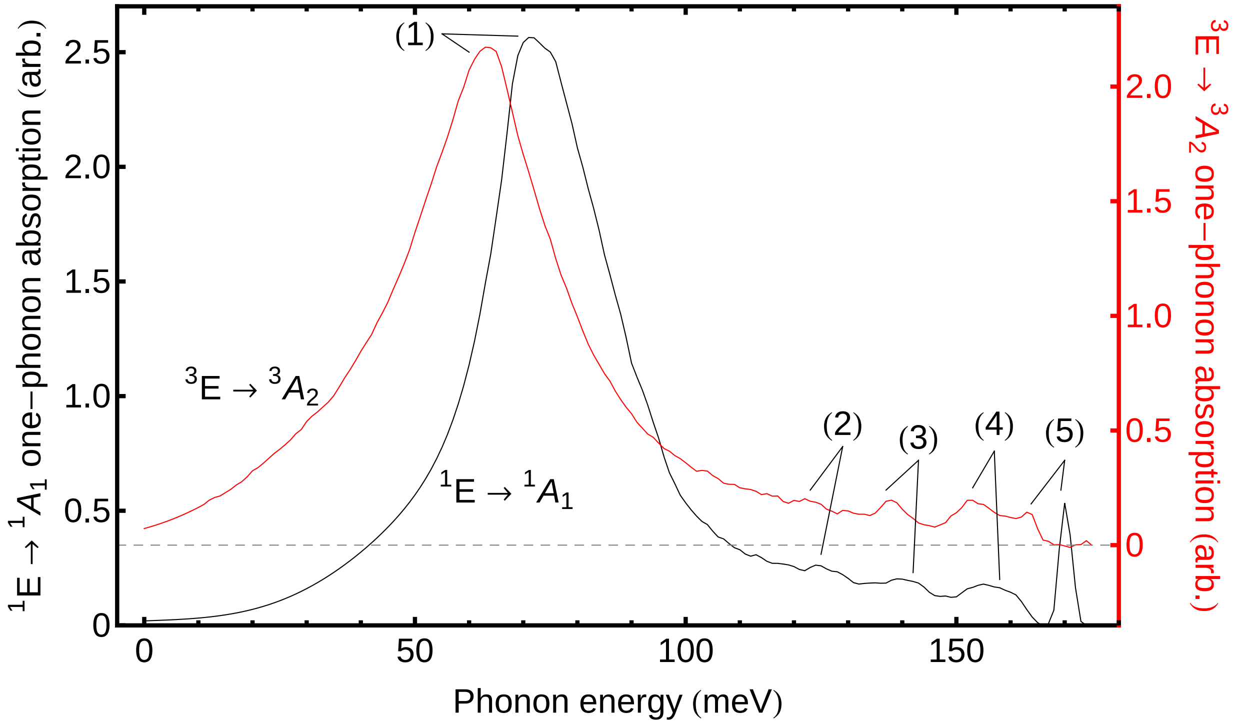

Figure 2.4: The one-phonon spectra for the $^1E \rightarrow {}^1A_1$ and $^3E \rightarrow {}^3A_2$ transitions, extracted from Fig. 2.3. The above spectra are normalized to have equal areas, and the $^3A_2$ curve is vertically offset for clarity. In each spectrum we see five peaks, labeled (1)-(5), though the $^1A_1$ peaks are shifted to higher energies (see Tab. 2.1).

metastable state throughout the diamond sample, from which we estimated the $^1E \rightarrow {}^1A_1$ ZPL cross section at room temperature. Since the Rayleigh range is about 150 μm (compared to a 730 μm thick diamond sample) and the 532 nm optical depth is about 4, our model takes into account the pump beam divergence and absorption in the diamond. Using this calculation of the metastable NV center density and the experimentally determined 1042 nm transmission in sample B8 at various pump powers, we determined the $^1E \rightarrow {}^1A_1$ ZPL cross section. For simplicity, we approximated the probe beam to be a straight line through the pump-beam axis. We estimated the $^1E \rightarrow {}^1A_1$ ZPL cross section to be 4×10^{-22} m^2. This value is consistent with that of Ref. [118]. The accuracy of this cross section estimate is primarily limited by uncertainty in the NV$^-$ concentration; varying the NV$^-$ concentration from 5 to 20 ppm in our model yields estimated cross sections ranging from 3.4 to 5.4×10^{-22} m^2 (compared to 4.0×10^{-22} m^2 with 10 ppm NV$^-$). Uncertainty in the NV center excited-state decay rates [39], the pump-laser absorption cross section [116], the pump beam waist, and the distance between the pump beam focus and the diamond surface contribute an additional uncertainty of about 0.9×10^{-22} m^2.

Temperature dependence of the $^1E \rightarrow {}^1A_1$ ZPL and PSB

We measured $^1E \rightarrow {}^1A_1$ supercontinuum absorption spectra while varying the temperature of sample B8 from 10 to 300 K. Figure 2.5 shows the absorption, linewidths, and integrated areas for the 1042 nm ZPL and the 811, 912, and 983 nm PSB features. These features became weaker and broader with increasing temperature, and the integrated areas decreased. The integrated areas should be independent of temperature [32]. However, the ^1E state has shorter lifetime at higher temperature due to the enhanced electron-phonon decay rate to $^3A_2$ [28]. We believe the decrease in integrated area is because of the consequent reduction in ^1E population at higher temperature.

Peak #	**$^3A_2$ state**	**$^1A_1$ state**
(1)	64 meV	71 meV
(2)	122 meV	125 meV
(3)	138 meV	141 meV
(4)	153 meV	156 meV
(5)	163 meV	169 meV

Table 2.1: The energies of the one-phonon peaks shown in Fig. 2.4. When comparing the energies of the $^3A_2$ and $^1A_1$ phonon modes, we see a systematic shift to higher energy of a few meV.

2.3 912 nm polarization selection rules

We investigated the light-polarization selection rules for 912 nm absorption and compared them to those listed in Table 2.2. An $E \rightarrow A_1$ transition is dipole-allowed for (x, y)-polarized light, while an $E \rightarrow E$ transition is also dipole-allowed for z-polarized light. A difference between the 912 nm selection rules and the expected $E \rightarrow A_1$ ZPL selection rules could indicate that the 912 nm line is an $E \rightarrow E$ transition or that the $^1E \rightarrow {}^1A_1$ selection rules are not strictly obeyed in PSB transitions [28]. We determined the polarization dependence of 912 nm absorption in a room-temperature optically-detected magnetic resonance (ODMR) experiment with diamond sample S2. We singled out the [111]-oriented NV centers with an axial 15 G static magnetic field, exposed the sample to microwaves from a nearby wire, and measured the diode-laser absorption as a function of microwave frequency. Microwaves resonant with $^3A_2$ $m_s = 0 \rightarrow m_s = \pm 1$ transitions spoil the optical spin polarization, increase ^1E population, and enhance probe absorption. By measuring the $m_s = 0 \rightarrow m_s = \pm 1$ absorption in [111]-oriented centers as a function of polarization angle for probe-light

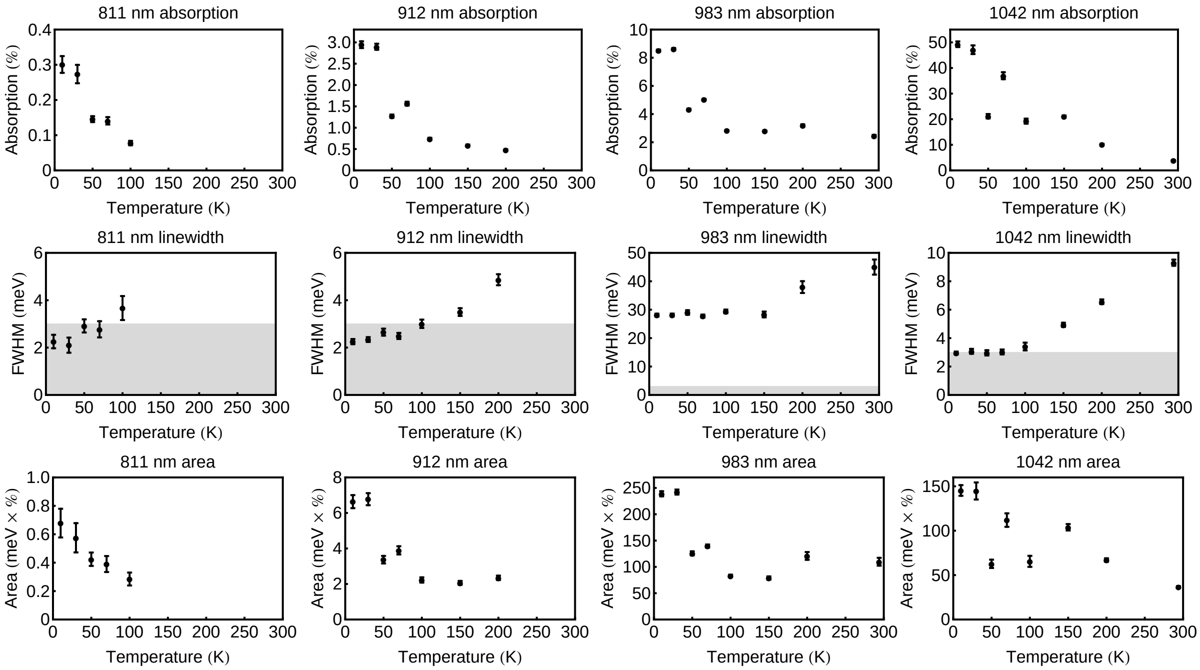

Figure 2.5: The percent absorption, linewidth, and integrated area of ${}^1E \rightarrow {}^1A_1$ absorption features in sample B8 as a function of temperature. The 811 and 912 nm lines vanished in the supercontinuum absorption spectra above 100 and 200 K, respectively. The spectrometer resolution contributes to the apparent linewidths plotted above; the gray region (3 meV) indicates where the spectrometer instrument broadening significantly contributes to the measured linewidths. We believe the 50 K and 90 K measurements to be outliers due to thermal expansion in the cryostat during the measurement. The above error bars are one-sigma statistical errors extracted from the parameter fits of the absorption spectra. We estimate a 1 meV systematic uncertainty on the above linewidths.

wavevector $\hat{k}$ parallel and perpendicular to the [111] z-axis, we found that the 912 nm transition is (x, y)-allowed and z-forbidden (Fig. 2.6). These selection rules indicate an $E \rightarrow A_1$ transition and are consistent with the ${}^1E \rightarrow {}^1A_1$ ZPL selection rules [28]. We performed this experiment at 40 K with the 912 nm Ti:Sapphire laser and obtained consistent results for $\hat{k} \parallel z$, but we were unable to test $\hat{k} \perp z$ because of mechanical constraints.

Using cw probe lasers and a similar diamond sample "S2" (16 ppm NV concentration), we measured the center wavelengths of the 912 and 1042 nm absorption lines at 40 K to be 912.19(2) nm and 1041.96(2) nm. Our ZPL center wavelength is consistent with previous measurements [28, 29]. At low temperatures, the 1042 and 912 nm features have narrow widths (currently limited by the spectrometer resolution). These narrow widths imply that the vibrational mode associated with the 912 nm feature is sharp. By measuring 912 nm

Transition	Dipole-allowed
$A_1 \leftrightarrow A_1$	z
$A_1 \leftrightarrow A_2$	–
$A_1 \leftrightarrow E$	(x, y)
$A_2 \leftrightarrow A_2$	z
$A_2 \leftrightarrow E$	(x, y)
$E \leftrightarrow E$	$(x, y), z$

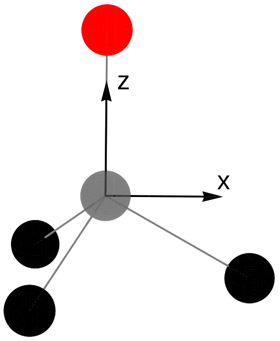

Table 2.2: Photon polarizations for dipole-allowed transitions between C_{3v} electronic states [32]. The notation "(x, y)" implies that any polarization in the x-y plane has the same transition amplitude. The drawing on the right indicates the choice of axes.

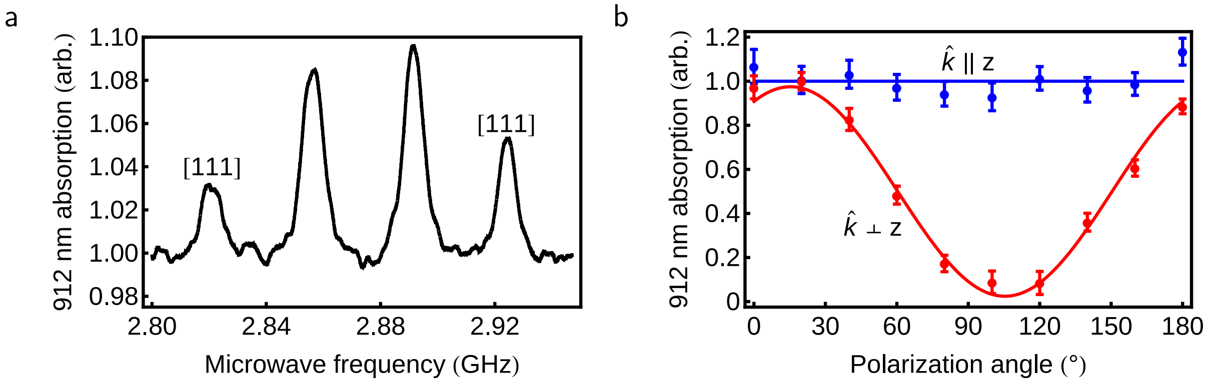

Figure 2.6: (a) A sample ODMR spectrum ($\hat{k} \perp z$) taken at room temperature, with absorption peaks for [111]-oriented centers labeled. The middle two peaks are due to the other three orientations. (b) 912 nm absorption by [111]-oriented centers at different light polarization angles. The $\hat{k} \parallel z$ case is only sensitive to x, y polarization while the $\hat{k} \perp z$ case is also sensitive to z polarization. The constant nonzero $\hat{k} \parallel z$ ODMR peak height and sinusoidal variation to zero in the $\hat{k} \perp z$ data indicate the transition is (x, y)-allowed and z-forbidden.

absorption as a function of light polarization angle, we found that the 912 nm absorption has the same polarization selection rules as the ${}^1E \rightarrow {}^1A_1$ ZPL [28].

A 532 nm pump laser may excite other defects besides NV$^-$ (such as NV^0), meaning we must be cautious when associating the observed infrared absorption features with the NV ${}^1E \rightarrow {}^1A_1$ transition. Selective excitation of infrared fluorescence using 637 nm pump light was shown in Ref. [105], meaning that while the 1042 nm ZPL is surely related to NV, we must convince ourselves that the other infrared absorption features are also part of this electronic transition. The one-phonon absorption spectrum (Fig. 2.4), the optically-detected magnetic resonance test of the 912 nm selection rules, and the fact that a transverse magnetic field enhances the infrared absorption all confirm that our absorption spectrum belongs to the NV $^1E \to {}^1A_1$transition.

2.4 Analysis and discussion

Comparing the $^1E \to {}^1A_1$ absorption PSB in Fig. 2.3a with previous observations of the $^1A_1 \to {}^1E$ fluorescence PSB [29, 105], it is evident that these PSBs differ significantly. This difference is due to the anharmonicity of the ^1E vibronic levels induced by the dynamic Jahn-Teller effect, which is not present in $^1A_1$ [105]. In the low-temperature limit, the PSB features of $A \to E$ electronic transitions exhibit anharmonicity, while the PSB features of $E \to A$ transitions are harmonic [136]. Consequently, it is appropriate to compare the $^1E \to {}^1A_1$ absorption PSB with the $^3E \to {}^3A_2$ fluorescence PSB. Furthermore, $^1A_1$ and $^3A_2$ have the same electronic configuration ($a_1^2e^2$) when electronic Coulomb repulsion is ignored, meaning they should have similar nuclear equilibrium positions and phonon modes. Since their initial states are different, the $^1E \to {}^1A_1$ and $^3E \to {}^3A_2$ transitions may couple to a different number of phonon modes and have different Huang-Rhys parameters, but the $^1A_1$ and $^3A_2$ one-phonon spectra should be similar.

As mentioned above, we extracted the one-phonon spectra from the PSBs shown in Fig. 2.3. The n-phonon spectrum is the convolution of the (n-1)-phonon and one-phonon spectra, and the sum of all n-phonon spectra generates the transition PSB. The one-phonon spectra are also related to the $^1A_1$ and $^3A_2$ phonon density of states (DOS). As seen in Fig. 2.4, we found similarities between the one-phonon spectra; both spectra have one large feature and four small features. However, all of the $^1E \to {}^1A_1$ features are displaced to higher energies (Tab. 2.1).

Introducing a point defect into a lattice alters the vibrational motion of the defect and its neighbors from what it would have been with ordinary atoms in the lattice. This is because the parameters that determine the frequencies of the vibrational motion for these atoms (the masses and effective spring constants) are modified. When the frequencies of the local oscillations of the defect lie within the spectrum of allowed vibrational modes of the remaining crystal, the local modes hybridize with the lattice modes and are called “quasilocal” (quasilocal because the nuclear oscillation amplitudes fall off slowly with increasing distance from the defect) [109, 135]. The ~71 meV phonon modes we observed appear to be from a quasilocal mode of NV in the $^1A_1$ state. The diamond lattice phonon DOS is appreciable at 71 meV [137, 138], and since the NV 71 meV mode couples strongly to the diamond lattice modes, the peaks of the 71 meV mode are consequently broadened.

In contrast to the quasilocal mode case, a “localized” mode occurs when the frequency of the local oscillations of a defect lies outside the lattice phonon DOS. In this instance, the oscillations of the defect couple poorly to the oscillations of the rest of the crystal, the vibrational motion is confined to the region of the defect, and the local phonon mode energy is unbroadened. This is the case for the 169 meV mode. The diamond lattice phonon DOS has an upper limit of 168 meV [12, 137, 138]. The NV 169 meV mode falls outside the diamond lattice phonon spectrum and couples poorly to the lattice modes, consequently making the peaks of the 169 meV mode in Fig. 2.3a sharp.

The existence of a 169 meV local phonon mode and the differences between the $^1E \rightarrow {}^1A_1$ and $^3E \rightarrow {}^3A_2$ one-phonon spectra are surprising for several reasons. *Ab initio* calculations for the NV triplet-state vibrations do not predict the existence of high-energy local phonon modes [108–110], and the $^1E \rightarrow {}^1A_1$ PSB is the only NV PSB to contain such a feature. Due to the discrepancy in one-phonon spectra, we conclude that the $^1A_1$ level has electronic Coulomb repulsion corrections that modify its phonon modes from those of the $^3A_2$ level. Since the features in the one-phonon spectrum are shifted to higher energies, we can determine that the nearby atoms are more tightly bonded in the $^1A_1$ level than in the $^3A_2$ level.

2.5 Summary

In summary, we measured the $^1E \rightarrow {}^1A_1$ absorption spectrum of the NV center using pump-probe spectroscopy. In the $^1E \rightarrow {}^1A_1$ PSB and one-phonon absorption spectrum we found several phonon modes, one of which lies outside the diamond lattice phonon DOS. The $^1E \rightarrow {}^1A_1$ and $^3E \rightarrow {}^3A_2$ one-phonon spectra show general similarity, but the $^1A_1$ phonon modes are shifted to higher energies, which is from corrections to the $^1A_1$ orbital configuration due to electronic Coulomb repulsion (not included in other theories). Our measurement of the $^1E \rightarrow {}^1A_1$ absorption spectrum shows that the ZPL is more absorptive than the PSB, and hence the ZPL offers greater sensitivity for infrared-absorption-based magnetometry than the PSB wavelengths. Furthermore, the NV ISC and optical pumping process can be modeled more precisely using our measured $^1A_1$ vibronic structure.

We searched for the $^1E \rightarrow {}^1E'$ ZPL for energies up to 2.0 eV at cryogenic temperature and 2.6 eV at room temperature, but we did not detect it. The $^3A_2 \rightarrow {}^3E$ and $^1E \rightarrow {}^1E'$ should have similar cross sections because they are transitions from electronic configuration $a_1^2e^2$ to a_1e^3 (neglecting Coulomb coupling). Since the $^1E \rightarrow {}^1A_1$ ZPL cross section is smaller than that of $^3A_2 \rightarrow {}^3E$ (see Ref. [116]), the $^1E \rightarrow {}^1E'$ transition should have a similar or larger cross section compared to the $^1E \rightarrow {}^1A_1$ transition. This means the $^1E \rightarrow {}^1E'$ ZPL would likely have been detected in our absorption measurements if its energy was less than 2.0 eV. This suggests that the $^1E \rightarrow {}^1E'$ ZPL energy is greater than 2.0 eV. Follow-up experiments will extend the search for the $^1E \rightarrow {}^1E'$ ZPL to higher energies with improved sensitivity.

The above NV singlet absorption spectroscopy work improved our theoretical understanding of NV properties and supported NV sensing. Our measurements can be used as validation tools for predicted $^1E \rightarrow^1 E'$ ZPL energies and $^1A_1$ vibration modes, the latter of which are important for explaining how NV optical pumping works. This work also aided the ongoing NV infrared absorption magnetometer development, which aims to reach spin-projection-noise-limited sensitivity [119].

Chapter 3

NV Saturation Spectroscopy

NV sensitivity improves when their ground-state microwave transitions are narrow, but these transitions suffer from inhomogeneous broadening, especially in high-density NV ensembles. To better understand and remove the sources of broadening, we demonstrate room-temperature spectral "hole burning" of the NV ground-state transitions. We find that hole burning removes the broadening caused by magnetic fields from ^{13}C nuclei and demonstrate that it can be used for magnetic-field-insensitive thermometry.

This work was published in Physical Review B in 2014 [112].

3.1 Introduction

The NV^- ground-state sublevels can be optically accessed and have long spin-relaxation times at room temperature [102], making them useful for sensing magnetic field and temperature. When limited by spin-projection noise, the sensitivity is proportional to $\sqrt{\Gamma/N_{\mathrm{NV}}t}$, where Γ is the optically-detected magnetic resonance (ODMR) linewidth, N_{NV} is the number of NV centers probed, and t is the measurement duration [4, 16]. In practice, the transitions are inhomogeneously broadened due to differences in the NV local environments, limiting the ensemble sensitivity. Diamond samples with more paramagnetic impurities also have more inhomogeneous broadening, meaning that larger N often comes with larger Γ. Furthermore, NVs with different Larmor frequencies dephase, which is a limitation in some applications. Although refocusing pulse sequences (such as Hahn echo) can restore the coherence, identifying the sources of ODMR linewidth broadening is essential for NV applications and for understanding the underlying diamond spin-bath and crystal-strain physics.

In this work we demonstrate novel use of saturation spectroscopy (also called "hole-burning") techniques in an NV ensemble. This is motivated by saturation spectroscopy in atoms, where a spectrally-narrow pump laser selects atoms of a particular velocity class by removing them from their initial state, allowing one to recover narrow absorption lines with a probe laser [139].

Optical hole-burning in solids has also been used for spectroscopy, photochemistry, and laser stabilization [140, 141]. Past experiments have demonstrated hole-burning and electromagnetically induced transparency (EIT) with NV centers (see Refs. [142, 143] and references therein) at low temperature using optical fields. Our work is at room temperature, where NVs are most often used in applications, and employs microwave (MW) fields instead. Moreover, the hole-burning method in Ref. [142] relies on Raman heterodyne detection and is only feasible at magnetic fields near 1000 G at 5 K temperature. Our saturation spectroscopy techniques are complementary to the previous efforts and work at any magnetic field.

We present two hole-burning schemes. The analytically simpler scheme ("pulsed hole-burning") is depicted in Fig. 3.1a. This scheme addresses a two-level subsystem ($m_s = 0$ and $+1$) and uses a modified pulsed-ODMR sequence (similar to that of Ref. [144]). A spectrally-narrow pump π-pulse first shelves a fraction of the NVs into the $m_s = +1$ state, after which a probe π-pulse reads out its effect on the NV population distribution. Figure 3.1b shows that using this method can yield hole widths significantly narrower than the inhomogeneous linewidth of this transition.

The other hole-burning scheme uses all three magnetic sublevels and continuous-wave MW fields ("CW hole-burning"). Here we pump the $m_s = 0$ to $+1$ transition and probe the $m_s = 0$ to -1 transition. Again, one observes narrower linewidths than with ordinary ODMR. Figure 3.2 shows ODMR spectra obtained without a CW pump field, with a pump, and a spectrum obtained by modulating the pump amplitude and using lock-in detection. The ODMR linewidth, which is largely determined by inhomogeneous magnetic fields from ^{13}C nuclei (1.1% natural abundance) and other sources such as substitutional nitrogen atoms (P1 centers), is reduced in CW hole-burning experiments to a smaller linewidth where the ^{13}C contribution is removed. We use CW hole-burning to study the causes of ODMR broadening in an NV ensemble and to demonstrate a magnetic-field-insensitive thermometer.

In pulsed hole-burning experiments, we pump and probe the same transition because it yields better fluorescence contrast than with different transitions. This choice is favorable in an NV experiment with poor signal-to-noise. However, applying CW MW fields on the same transition can result in coherent population oscillation (CPO), where the state populations of a quantum system oscillate at the beat frequency between the pump and probe fields [145, 146]. We use two transitions in CW hole-burning to avoid CPO, and because this choice is useful for determining the dominant source of inhomogeneous broadening. We also show that this more complex hole-burning scheme has applications, a specific example being improved NV thermometry.

3.2 Methods and results

Figure 3.3 shows a confocal microscopy setup, where the NV fluorescence (637-900 nm) is collected with the same lens as is used for excitation and optical pumping (done with 532 nm laser light). We exposed the diamond samples to the pump and probe MW fields with a nearby wire. The pump burns a hole in the $m_s = 0$ population by driving resonant NV centers into the $m_s = +1$ state, which spoils the ODMR contrast. In CW hole-burning

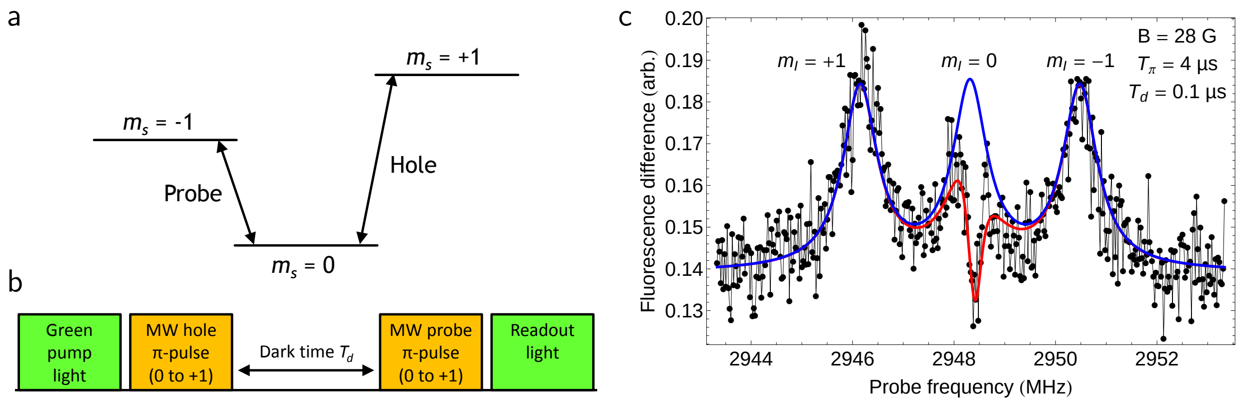

Figure 3.1: (a) A simplified $^3A_2$ energy-level diagram showing the transitions used for CW hole burning. (b) The pulse sequence used for pulsed hole burning. (c) The result of a pulsed-hole experiment in sample CVD1 (see Tab. 3.1). The 0.3 MHz FWHM hole is Fourier-limited and is narrower than what was achieved with CW hole-burning (Tab. 3.1) The model for the fit is described in the text.

Sample	**[N] (ppm)**	**[NV$^-$] (ppm)**	**ODMR FWHM**	**Hole FWHM**
HPHT1	<200	1-10	1.7 MHz	1.4 MHz
HPHT2	50	1-10	1.2 MHz	0.7 MHz
CVD1	1	0.01	1.2 MHz	0.5 MHz CW, 0.3 MHz pulsed
CVD2	<1	0.01-0.1	0.9 MHz	0.6 MHz

Table 3.1: Details of the diamond samples tested and the smallest linewidths measured (extrapolated to zero MW power). The above widths are for the ^{14}N hyperfine components of the NV transitions (0.1 MHz accuracy). Each sample has 1.1% ^{13}C concentration. HPHT samples were grown with high-pressure high-temperature crystal formation, and CVD samples by chemical vapor deposition.

measurements, we amplitude-modulated the pump and used lock-in detection to determine the hole linewidths more easily (Fig. 3.2c) [147].

Determining the source of inhomogeneous broadening using continuous-wave hole-burning

The relevant NV electronic ground-state Hamiltonian (in units of hertz) is

$$H = (D + d^{\parallel}\delta\epsilon)S_z^2 + \gamma(B + \delta B)S_z, \tag{3.1}$$

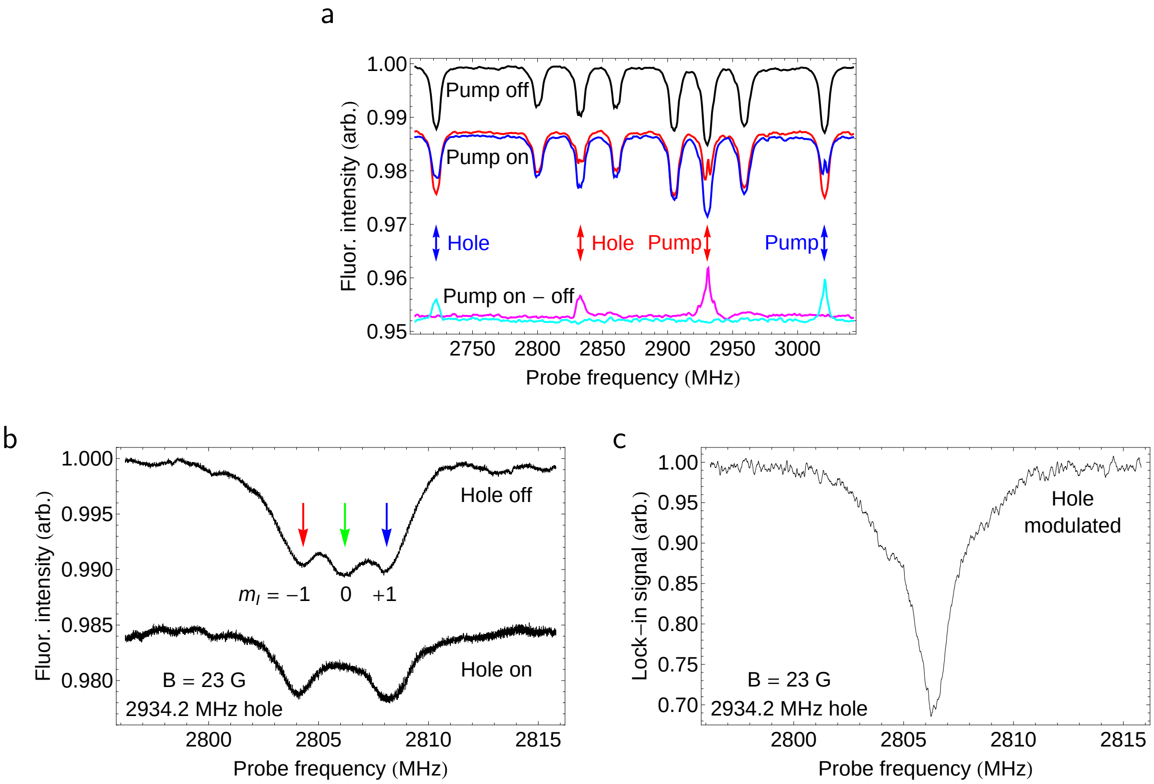

Figure 3.2: (a) CW ODMR spectra in sample HPHT1 with a static magnetic field along an arbitrary direction, which splits the resonances of the four NV-axis alignments into four pairs of frequencies. Burning a hole at any frequency only affects NVs of the associated alignment. The slight asymmetries in ODMR contrast are likely due to differences in MW power delivered to the NVs. (b) ODMR spectra of the $m_s = 0$ to $+1$ transition, now with an axial magnetic field. (c) Here we amplitude-modulate the pump field and perform lock-in detection on the NV fluorescence intensity.

where S_z is the dimensionless spin projection operator, D is the zero-field splitting, $\gamma = 2.8$ MHz/G is the gyromagnetic ratio, B is the axial magnetic field, and $d^{\parallel}$ is related to the axial electric dipole moment. Each NV has different local axial magnetic field (δB) and strain ($\delta\epsilon$) values, the distributions of which (with respective widths ΔB and $\Delta\epsilon$) cause inhomogeneous broadening. A hole-burning test can determine the dominant source of inhomogeneous broadening in a diamond sample. The MW transition frequencies for a specific NV are $f_\pm = D + d^{\parallel}\delta\epsilon \pm \gamma(B + \delta B)$. If the NV ensemble experiences a distribution of magnetic fields (either from a gradient in the applied magnetic field or from magnetic spins in the diamond) and $\delta\epsilon \approx 0$, then the pump at f_+ selects the NVs with a particular δB and the spectral hole appears at

$$f_- = 2D - f_+. \tag{3.2}$$

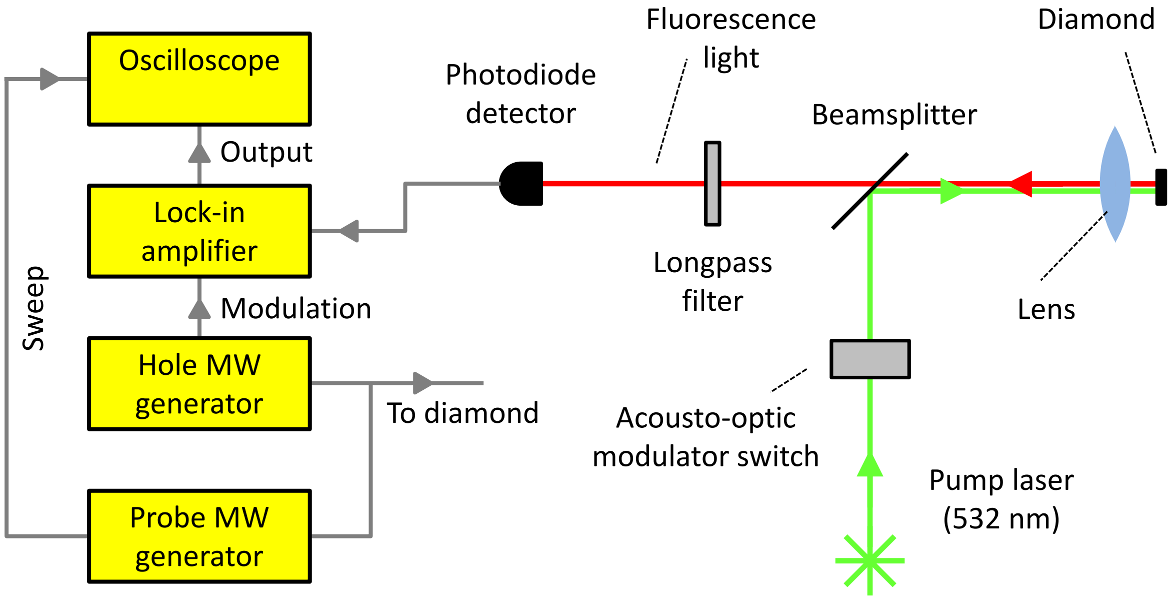

Figure 3.3: The experimental apparatus for CW hole-burning. We amplitude-modulated the hole MW field at 1.3 kHz. In a pulsed hole-burning experiment, the hole MW field is not modulated and there is no lock-in amplifier.

Alternatively, if the ensemble experiences a distribution of axial strains and $\delta B \approx 0$, then f_+ selects the NVs with a particular $\delta\epsilon$ and

$$f_- = f_+ - 2\gamma B. \tag{3.3}$$

Since Eqs. (3.2) and (3.3) predict how f_+ and f_- are correlated in different physical situations, we can test this correlation to learn whether the effect of ΔB or $\Delta\epsilon$ is dominant. As seen in Fig. 3.4a, varying f_+ causes f_- to shift with the opposite sign, meaning that differences in magnetic field cause the inhomogeneous broadening.

Since f_- depends only on f_+ and D, it is resistant to changes in B, as shown in Fig. 3.4b. Varying B by ± 0.9 G preserves f_- to within ± 0.2 MHz while the transition frequencies vary by ± 2.5 MHz (shown by dashed lines). If f_+ lies on a slope of the $m_s = 0$ to $+1$ lineshape, f_- will be shifted by a "frequency pulling" effect due to a product of the pump and $m_s = 0$ to $+1$ lineshapes. The residual ± 0.2 MHz spread in f_- comes from the magnetic field dependence of the $m_s = +1$ sublevel and the frequency pulling effect.

Magnetic-field-insensitive thermometry with CW hole-burning

Hole-burning is useful for thermometry because the hole width is narrower than the ordinary ODMR width, f_- is protected against changes in magnetic field, and f_- shifts

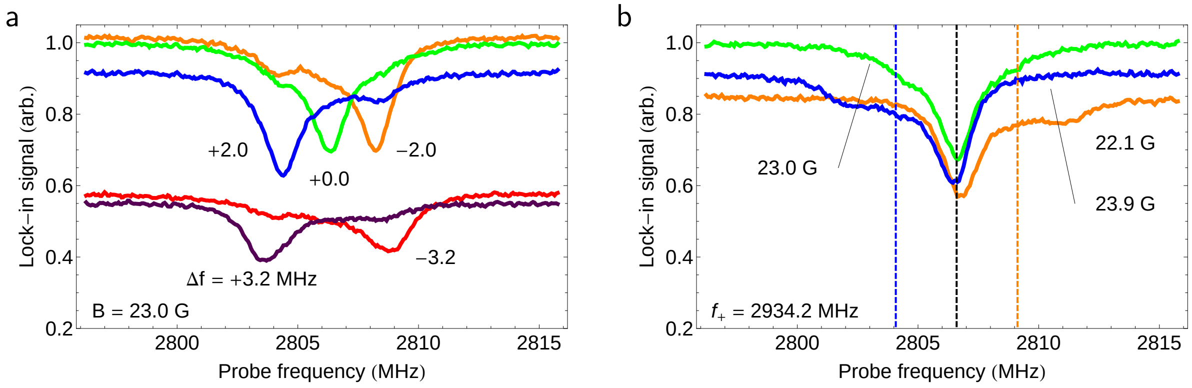

Figure 3.4: (a) The effect of changing the pump frequency ($f_+ = 2934.2$ MHz $+ \Delta f$) on the hole center frequency f_- (diamond sample HPHT1). The lock-in signal when the probe is off resonance is due to the NV fluorescence being modulated by the pump MW at the lock-in frequency and is a measure of the pump absorption. Varying f_+ confirms the prediction made in Eq. (3.2). (b) Here we keep f_+ constant but vary B near 23 G. Frequency pulling causes a ±0.2 MHz shift when B changes by ±0.9 G (dashed lines). Additional data are included in Ref. [112].

by twice as much when the temperature changes compared to ordinary ODMR. At room temperature, D shifts by $\alpha = -74.2$ kHz/K [6]. Using fixed f_+ and B, we varied the temperature of diamond sample HPHT2 (Fig. 3.5). From Eq. (3.2) we nominally expect $df_-/dT = 2\alpha$. To anticipate the aforementioned frequency pulling on f_-, we used the fit function

$$f_-(T) = c_1 + 2\alpha T + c_2 \sin\left[2\pi \times \frac{\alpha}{A} T + c_3\right], \tag{3.4}$$

where the c_i are free parameters, T is temperature, and the sine function models the frequency pulling caused by the ^{14}N hyperfine peaks in the ODMR spectrum (separated by $A = 2.166$ MHz [40]). Repeating this experiment with many f_+ frequencies yielded a mean $2\alpha = -151$ kHz/K with a spread of 2 kHz/K (probably due to the remaining effect of frequency pulling), which is consistent with the expected value of -148 kHz/K.

Frequency pulling may limit the thermometer accuracy; however, choosing f_+ and f_- wisely can minimize this effect and even improve the sensitivity, as frequency pulling boosts the local slope by up to 30%. Other methods for making NV magnetometers, thermometers, and clocks more stable in fluctuating thermal and magnetic environments have been developed [7, 15, 101, 148, 149]. These methods use MW pulses to create $m_s = \pm 1$ superpositions, canceling deleterious phase accumulation from unwanted temperature or magnetic field drifts. While a CW hole-burning thermometer also uses the $m_s = \pm 1$ states, it does not require superpositions or MW pulses.

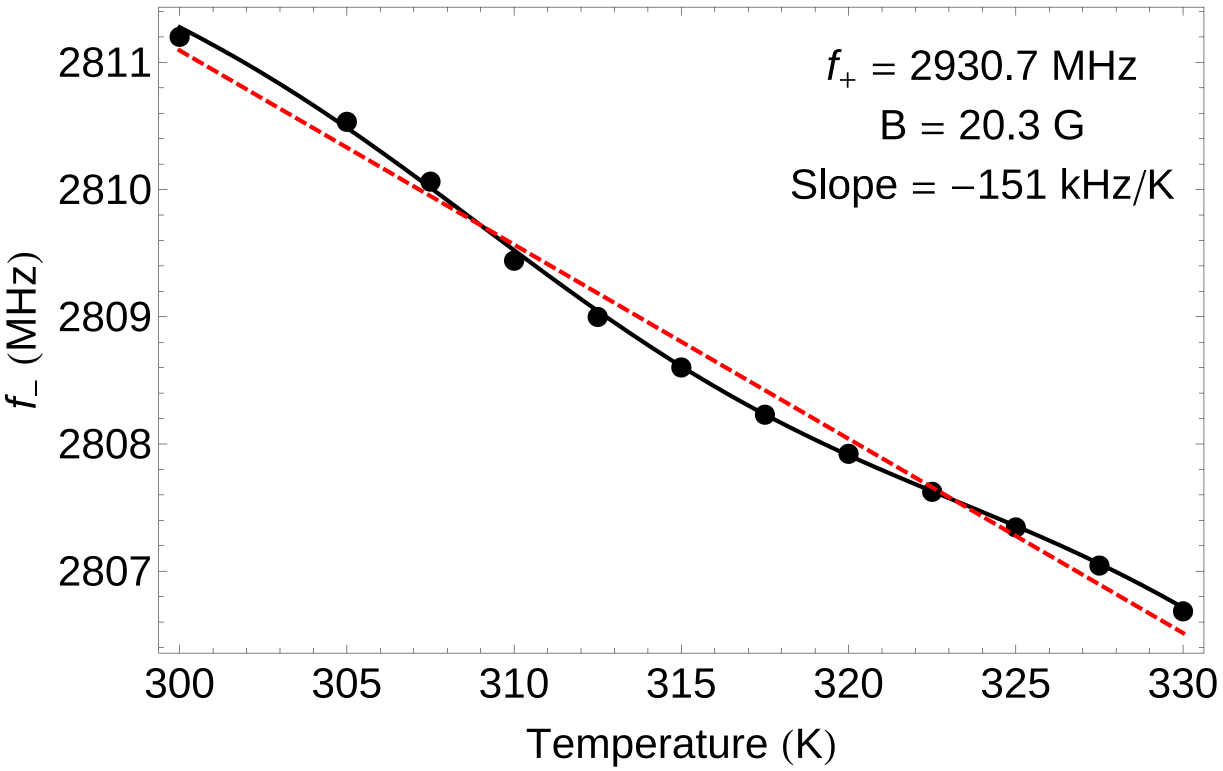

Figure 3.5: Temperature dependence of f_- in sample HPHT2. The solid line is a fit done with Eq. (3.4), and the dashed line is the linear part of this fit. Note that the oscillation period is not an independent free parameter, but is fixed by the model. Each point corresponds to a 20 MHz ODMR scan taken over 10 s.

3.3 Analysis and discussion

Magnetic inhomogeneity and spin bath

Figure 3.4a shows that differences in local magnetic field are the main broadening source of the NV ODMR transitions. The diamond samples contain ^{13}C nuclei and paramagnetic impurities (such as P1, NV^0, and NV$^-$). From their magnetic dipole moments and densities, one can estimate that ^{13}C nuclei and P1 centers are the main contributors to local magnetic-field inhomogeneity, in roughly equal proportions. These CW hole-burning experiments (with 1.3 kHz modulation frequency) remove the linewidth contribution from ^{13}C nuclei.

To reach this conclusion, we compared the ODMR and CW hole linewidths in different diamond samples. The ^{13}C spin bath fluctuates with a correlation time τ_c of ∼10 ms [150], which is slow compared to the (1.3 kHz)$^{-1}$ time scale of a CW hole-burning experiment. This means that the ^{13}C magnetic fields are static for the duration of the experiment. Furthermore, Ref. [151] reports that ^{13}C nuclei are the primary source of broadening (∼0.2 MHz) in samples with few paramagnetic impurities. In Tab. 3.1, the hole width is roughly 0.5 MHz smaller than the ODMR width, an improvement which is comparable to what Ref. [151] suggests. The 1.3 kHz modulation frequency is slow compared to the P1 τ_c ($\sim$10 μs [152–154]), meaning P1 centers still contribute to the CW hole linewidth. Since hole burning removes the influence of ^{13}C nuclei, it effectively leaves a diamond without ^{13}C. Some experiments avoid the effect of ^{13}C nuclei with a more "brute force" approach by using isotopically pure (^{13}C-depleted) synthetic diamonds [9, 19, 60, 155].

For short times (faster than any τ_c and the NV T_1), pulsed hole-burning experiments can create spectral holes that are narrower than what was achieved in the slower CW hole-burning experiments described above. Figure 3.1c shows a 0.3 MHz hole in the ODMR spectrum of sample CVD1, which is narrower than the 0.5 MHz hole we achieved using lock-in detection. This hole width is Fourier-limited and can be reduced to about 0.15 MHz. If the inhomogeneous magnetic fields are constant for τ_c, the spectral hole vanishes for dark times $T_d > \tau_c$. Extending the π-pulse duration can reveal what limits the hole width and determine τ_c for different spin-bath species. Previous experiments have measured NV decoherence in pulsed-microwave experiments to study the P1 and ^{13}C τ_c [150, 152–154]. In comparison, investigating τ_c with pulsed hole-burning does not require coherent superpositions, which is useful when τ_c is longer than the NV T_2.

Fluorescence in pulsed hole-burning experiments - an intuitive picture

Following Fig. 3.1, we compare the outcomes of two pulsed hole-burning experiments. In the first (experiment 1), the pump and probe drive the $m_s = 0$ to $+1$ transition, while the pump instead drives the $m_s = 0$ to -1 transition in the second (experiment 2). Assuming that a π-pulse resonant with one of the hyperfine components of an NV transition causes a change ΔF in fluorescence and that the hole frequency f_h is resonant with the $m_I = 0$ hyperfine component, we consider the following illustrative cases for the readout frequency f_r for each experiment:

I $f_r \approx f_h$.

II $f_r \neq f_h$ and is not resonant with other NV transitions.

III $f_r \neq f_h$, but is resonant with other NV transitions.

The final-state populations for the above experiments and cases are portrayed in Fig. 3.6. Figure 3.7a shows the result when the hole pulse is disabled, which is identical to an ordinary pulsed-ODMR experiment. When on resonance with a hyperfine component, the probe drives NVs into the $m_s = +1$ state, causing a change ΔF in fluorescence. In experiment 1 (expected spectrum shown in Fig. 3.7b), the probe returns all of the NV population to the $m_s = 0$ state in case I, and the fluorescence is maximal. In case II, the probe has no effect, but the NV fluorescence is reduced by ΔF since some NVs remain in the $m_s = +1$ state. The

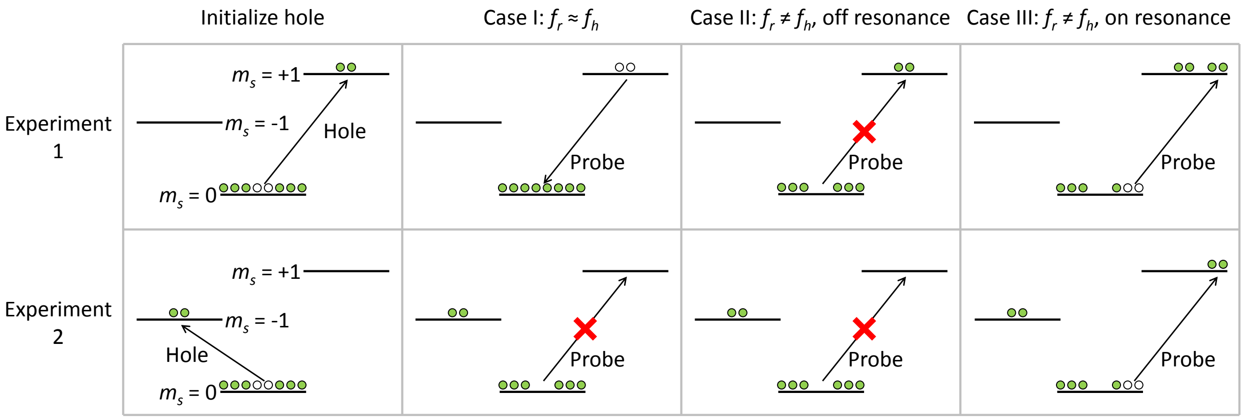

Figure 3.6: The actions of the π-pulses on the sublevel populations. After being initialized into the $m_s = 0$ state, two π-pulses are applied, yielding different final-state populations depending on the experiment and f_r. Open circles represent NVs removed by the π-pulse, and filled circles represent NV population after the pulse has acted. A red cross indicates that the probe does not affect the populations. Note that in case I of experiment 2, the NVs that were pumped are detected at $f_r = 2D - f_h$.

fluorescence is further reduced in case III, as the probe brings more NVs to the $m_s = +1$ state.

Experiment 2 (Fig. 3.7c) has a similar result to that of experiment 1 with one exception. In case I the probe has no effect because the NVs it is resonant with are in the $m_s = -1$ state. Comparing this result to that of experiment 1, we see that experiment 1 is preferable, since the hole pulse has a larger effect on the NV population. We therefore pursued experiment 1 to burn narrow holes, as this scheme has a better signal-to-noise ratio.

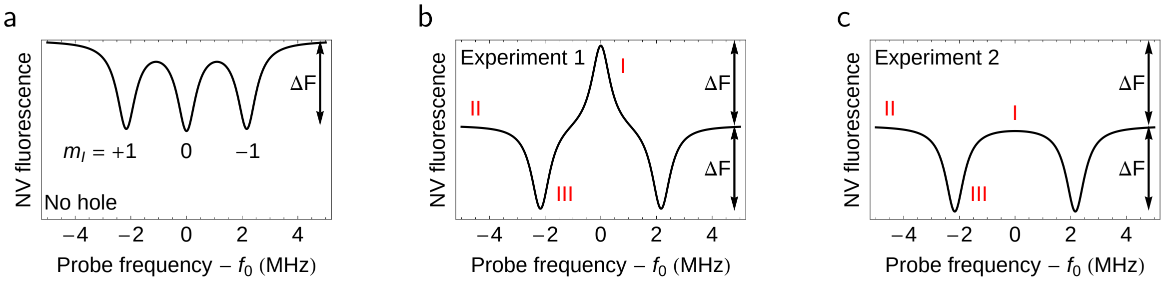

Figure 3.7: The expected results of pulsed-ODMR (a) and pulsed hole-burning experiments 1 (b) and 2 (c). We assume that the $m_s = 0$ to $+1$, $m_I = 0$ transition has frequency f_0. The red labels identify the expected fluorescence for the above three cases.

Fluorescence in CW hole-burning experiments

The above description also aids in understanding differences in CW hole-burning contrast. Assuming a strong pump (which saturates the $m_s = 0$ to $+1$ transition) and a weak probe, we again consider three cases:

I The probe is resonant with either of the MW transitions, and the pump is off.

II The probe is resonant with the $m_s = 0$ to $+1$ transition, and the pump is on.

III The probe is resonant with the $m_s = 0$ to -1 transition, and the pump is on.

The expected ODMR plots are shown in Fig. 3.8. In case I, the probe suppresses the NV fluorescence by $\Delta F \propto N_{\text{NV}}$, where N_{NV} the number of resonant NVs in the $m_s = 0$ state. When the pump is switched on, the NV fluorescence is reduced by a fixed amount because the pump puts half of the resonant NVs in the $m_s = +1$ state. This is the reason for the offsets in the fluorescence intensities in Fig. 3.2 and Fig. 3.8. The probe has no additional effect on the NV fluorescence in case II because the $m_s = 0$ to $+1$ transition is saturated, and the fluorescence returns to the off-resonant intensity when the probe has the same frequency as the pump. In case III, the pump has removed half of the resonant NVs from the $m_s = 0$ state, but since there is no population in the $m_s = -1$ state, the probe further reduces the fluorescence by $\Delta F/2$ when on resonance. Although we again see a larger effect when pumping and probing the same transition (a “hole depth” of ΔF compared to $\Delta F/2$), analyzing case II is more challenging because of CPO (see references in the main text), which we leave for future work. Instead, we pursued case III as it has interesting physics and applications that are not possible with case II.

Pulsed hole-burning model

The earlier sections provided an intuitive description of the final-state population distributions expected in a pulsed hole-burning experiment. We now form a more complete model to fit pulsed hole-burning data. Furthermore, as the π-pulse spectral width decreases, the hole width decreases, but since narrow pulses transfer less NV population, the hole also becomes less visible. This model provides an estimate of the smallest achievable hole width.

For simplicity, we analyze here the two-state pulsed-hole scenario. As the π-pulse Fourier width is not the main source of limitation, we expect that the results of the simpler scenario are relevant to the more complex CW case as well.

Consider a MW transition ($m_s = 0$ to $+1$, $m_I = 0$) in a pulsed hole-burning experiment. We assume that the sources of inhomogeneous broadening are static. The inhomogeneous lineshape is a Lorentzian with HWHM γ_i, and for simplicity we consider the π-pulse frequency spectrum to also be a Lorentzian with HWHM γ_π. When optically pumped into the $m_s = 0$ sublevel, the probability density function (PDF) for finding an NV with a particular

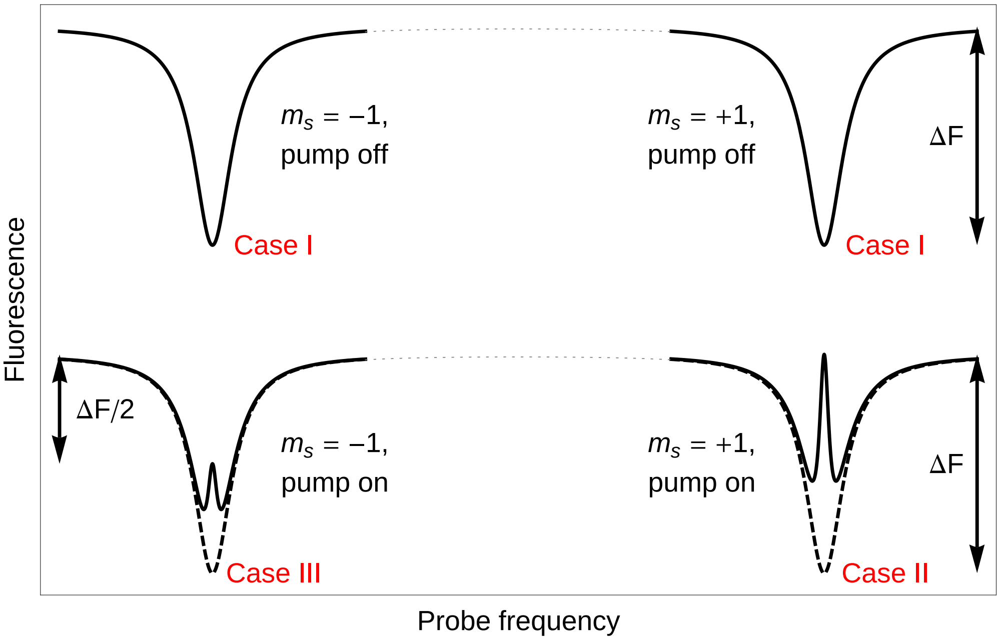

Figure 3.8: An illustrative picture of CW ODMR. Here we compare the differences in NV fluorescence when probing the $m_s = 0$ to $+1$ and $m_s = 0$ to -1 transitions, ignoring the effect of CPO. From this we see that pumping and probing the same transition produces a more prominent feature in the ODMR spectrum.

transition frequency f to the $m_s = +1$ state is

$$\frac{1}{\pi}\frac{\gamma_i}{\gamma_i^2 + f^2}. \tag{3.5}$$

Here we use a frequency scale such that the center frequency of the above Lorentzian corresponds to $f = 0$. A MW π-pulse, centered at frequency f_{MW}, transfers a fraction of the NV population (with resonance frequency f) equal to

$$\frac{\gamma_\pi^2}{\gamma_\pi^2 + (f - f_{MW})^2}. \tag{3.6}$$

Note that the PDF is normalized to have a total population of 1 and the π-pulse transfers 100% of the NV population that has resonance frequency f_{MW}. After the hole π-pulse (which burns a hole at $f = 0$), the $m_s = 0$ and $+1$ PDFs are

$$p_0^{\text{hole}}(f) = \frac{1}{\pi}\frac{\gamma_i}{\gamma_i^2 + f^2} - \frac{1}{\pi}\frac{\gamma_i}{\gamma_i^2 + f^2} \times \frac{\gamma_\pi^2}{\gamma_\pi^2 + f^2}, \tag{3.7}$$

$$p_{+1}^{\text{hole}}(f) = \frac{1}{\pi}\frac{\gamma_i}{\gamma_i^2 + f^2} \times \frac{\gamma_\pi^2}{\gamma_\pi^2 + f^2}. \tag{3.8}$$

After the readout π-pulse (with center frequency f_r), the PDFs are

$$
\begin{aligned}
p_0^{\mathrm{read}}(f) &= p_0^{\mathrm{hole}}(f) + \left[p_{+1}^{\mathrm{hole}}(f) - p_0^{\mathrm{hole}}(f)\right] \times \frac{\gamma_\pi^2}{\gamma_\pi^2 + (f - f_r)^2}, &(3.9)\\
p_{+1}^{\mathrm{read}}(f) &= p_{+1}^{\mathrm{hole}}(f) + \left[p_0^{\mathrm{hole}}(f) - p_{+1}^{\mathrm{hole}}(f)\right] \times \frac{\gamma_\pi^2}{\gamma_\pi^2 + (f - f_r)^2}. &(3.10)
\end{aligned}
$$

In practice, we vary f_r and determine the population fraction in $m_s = 0$ from the fluorescence intensity. To determine the fraction of NVs in each sublevel as a function of f_r after the readout pulse, we integrate over f to get

$$
\begin{aligned}
P_0(f_r) &= \frac{f_r^4\gamma_i + f_r^2\left(\gamma_i^3 + \gamma_\pi\gamma_i^2 + 3\gamma_\pi^2\gamma_i + \gamma_\pi^3\right) + 4\gamma_\pi^2\left(\gamma_i + \gamma_\pi\right)\left(\gamma_i^2 + \gamma_\pi\gamma_i + \gamma_\pi^2\right)}{\left(\gamma_i + \gamma_\pi\right)\left(f_r^2 + 4\gamma_\pi^2\right)\left[f_r^2 + \left(\gamma_i + \gamma_\pi\right)^2\right]}, &(3.11)\\
P_{+1}(f_r) &= \frac{\gamma_\pi\left(2f_r^2\left(\gamma_i^2 + 2\gamma_\pi\gamma_i + 2\gamma_\pi^2\right) + f_r^4 + 4\gamma_\pi^2\gamma_i\left(\gamma_i + \gamma_\pi\right)\right)}{\left(\gamma_i + \gamma_\pi\right)\left(f_r^2 + 4\gamma_\pi^2\right)\left[f_r^2 + \left(\gamma_i + \gamma_\pi\right)^2\right]}. &(3.12)
\end{aligned}
$$

We used a generalized version of Eq. (7), where the hole center frequency is a free parameter, to fit the data in Fig. 3.1c. The width and contrast of the narrow feature are not free parameters because the π-pulse duration determines γ_π and the model predicts the contrast. As seen in the figure, the fit describes the hole width and lineshape well. We also investigated a second model where the π-pulse spectrum is a sinc^2 function instead of a Lorentzian, which more accurately describes our π-pulses. The Lorentzian and sinc^2 results are similar, meaning the simpler Lorentzian model is sufficient.

As seen in Fig. 3.9a, the effect of the hole on the NV population vanishes as γ_π approaches 0. To estimate the minimum achievable hole width, we determine γ_π for which the population deviates by 0.1 when $f_r = 0$. We select 0.1 as a figure of merit; in practice the experimental sensitivity to changes in fluorescence regulates the smallest visible hole width. Solving $P_{+1}(0) = \frac{\gamma_\pi\gamma_i}{(\gamma_\pi+\gamma_i)^2} = 0.1$ yields $\gamma_\pi \approx 0.13\gamma_i$. The widths of the narrow peaks in Fig. 3.9a are roughly $2\gamma_\pi$ (since there are two π-pulses). The inhomogeneous FWHM in sample CVD1 (Fig. 1c) is about 600 kHz, meaning the smallest hole we can burn with this method has a FWHM of about 150 kHz.

Sensitivity considerations for hole-burning experiments

We measure NV fluorescence to detect changes in ODMR transition frequency f, from which we can detect changes in parameters such as temperature. For a single measurement, the frequency noise due to spin projection noise is

$$\delta f_{\mathrm{spin}} \approx \sqrt{\frac{\Gamma}{N_{\mathrm{NV}}t}}, \tag{3.13}$$

where N_{NV} is the number of NV centers probed, Γ is the ODMR resonance width, and t is the measurement duration.

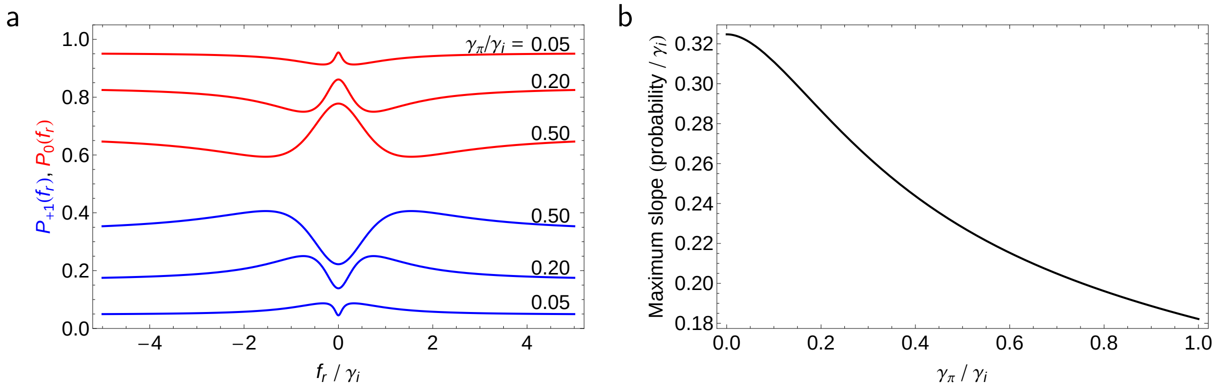

Figure 3.9: (a) Final-state population fractions $P_0(f_r)$ and $P_{+1}(f_r)$ for $\gamma_\pi/\gamma_i = 0.05$, 0.20, and 0.5. (b) The maximum slope achievable for a pulsed hole-burning experiment, where the readout π-pulse probes the $m_s = 0$ to -1 transition. The slope increases with narrower pulse widths, improving the spin-projection noise and photon shot noise.

The noise contributed from photon detection is written as

$$\delta f = \frac{\delta N_{\text{phot}}}{dN_{\text{phot}}/df} \approx \frac{\delta N_{\text{phot}}}{CN_{\text{phot}}/\Gamma}, \tag{3.14}$$

where N_{phot} is the number of photons detected and C is the fluorescence contrast (the fractional difference between on-resonance and off-resonance fluorescence intensity). For photon shot noise, $\delta N_{\text{phot}} = \sqrt{N_{\text{phot}}}$ and

$$\delta f_{\text{shot}} \approx \frac{\Gamma}{C}\frac{1}{\sqrt{N_{\text{phot}}}}. \tag{3.15}$$

For electronic white noise (such as photodiode dark current noise), δN_{phot} is a constant α and

$$\delta f_{\text{white}} \approx \frac{\Gamma}{C}\frac{\alpha}{N_{\text{phot}}}. \tag{3.16}$$

Finally, $\delta N_{\text{phot}} = \beta N_{\text{phot}}$ for technical noise on the laser intensity, where β is the fractional intensity deviation of the pump laser,

$$\delta f_{\text{tech}} \approx \frac{\Gamma}{C}\beta. \tag{3.17}$$

Saturation spectroscopy reduces both Γ and N_{NV}, which have competing effects on δf_{spin}. However, δf_{shot}, δf_{white}, and δf_{tech} depend on $s = C/\Gamma$, the maximum slope of the ODMR spectral feature, meaning we can analyze whether saturation spectroscopy yields steeper s to see if sensitivity improves. To do this, we modify the pulsed hole-burning experiment to instead probe the $m_s = 0$ to -1 transition (a scheme that could be used for thermometry) and calculate the final-state populations to determine whether narrower γ_π improves s. This is a useful assessment method because it models a real experiment and only γ_π and s are variables, leaving no ambiguity about how other parameters affect the noise. Figure 3.9b depicts the maximum slope (in units of probability per frequency) of the resulting pulsed-ODMR spectrum, which demonstrates that narrower γ_π yields better δf_{shot}, $\delta f_{\mathrm{white}}$, and δf_{tech}.

3.4 Summary

In summary, we have demonstrated CW and pulsed hole-burning in NV ensembles in diamond. Using CW hole-burning tests, we distinguished between dominant sources of ODMR broadening and showed that broadening comes mainly from differences in magnetic fields (rather than differences in axial strain). The lock-in detection method eliminates the linewidth contribution from slowly-fluctuating ^{13}C nuclei, while the rapidly-fluctuating magnetic fields from P1 centers and other sources contribute to a reduced linewidth. We also demonstrated a promising temperature sensor that is resistant to magnetic field fluctuations. With pulsed hole-burning, we created narrower spectral holes with Fourier-limited widths, which may be used to study spin-bath dynamics.

Saturation spectroscopy reduces both the ODMR linewidth and the number of NVs addressed, which have competing effects on the spin-projection noise. However, MW π-pulses with narrower spectral widths improve the sensitivity when a pulsed hole-burning experiment is limited by other noise sources such as photon shot noise.

NV researchers prefer ^{13}C-depleted diamond samples, which have better coherence time and sensitivity at the expense of limited availability and greater cost. Since hole burning eliminates the linewidth contribution from ^{13}C nuclei, this may alleviate the need for ^{13}C-depleted samples in certain applications. Conversely, hole burning may yield a larger relative improvement in linewidth with ^{13}C-enriched samples. This may enable high-resolution microwave spectroscopy despite significantly inhomogeneously broadened linewidths, with benefits to ^{13}C-based NMR and gyroscopy [65, 156]. In future work, we will search for interactions between NVs with different orientations by pumping NVs in one alignment and probing another, which may help explain the enhanced NV T_1 relaxation rate at low magnetic field [56].

Chapter 4

NV Relaxation and Decoherence Spectroscopy

In addition to sensing DC and coherent AC magnetic fields, NV centers can also sense incoherent magnetic noise, which cause the NV $^3A_2$ magnetic sublevels to relax more rapidly. Magnetic noise contributes to longitudinal (T_1) and transverse (T_2) relaxation, depending on the noise frequency and the particular experiment. Previous experiments can sense the presence of optically-dark magnetic spins (electrons and nuclei) a few nanometers away and can identify the spin species and density from the noise frequency and amplitude. In this section, I present my work on NV cross-relaxation with paramagnetic substitutional nitrogen (P1) centers, which is an example of how NV T_1 relaxation can be an electron paramagnetic resonance (EPR) detector for unpolarized paramagnetic spins.

We can label the accelerated NV electronic T_1 relaxation due to magnetic dipole transitions as being from "cross-relaxation" or "magnetic noise." The former refers to energy-conserving "flip-flop" transitions between two spin species on resonance (such as NV-P1 resonance near 500 G), which we can think of as magnetic noise (dipole-dipole relaxation) at a well-defined frequency. The latter refers to NV relaxation from a broadband spectrum (such as Gd^{3+}, a spin-7/2 paramagnetic ion with a ∼10 GHz relaxation rate) [57]. Similarly, we can think of this as cross-relaxation with poorly-defined Gd^{3+} sublevels. In this chapter I use the above terms interchangeably, as the T_1 experimental methodology is similar for both cases.

A previous experiment studied NV T_1 relaxation as a function of temperature and magnetic field [56]. This experiment found that T_1 is reduced near 500 G because of cross-relaxation with P1 centers. However, this measurement scanned the applied magnetic field in coarse steps, meaning possible cross-relaxation with other paramagnetic centers and detailed structure of the NV-P1 cross-relaxation were hidden. We extended this work by examining NV T_1 at 500 G with high magnetic field resolution (0.1 G) and enhanced T_1 decay due to multiple NV-P1 level crossings. Together with a theoretical framework for turning T_1 into a magnetic noise power spectral density, this work shows how NVs can serve as a "magnetic noise spectrometer" at GHz frequencies.

The NV-P1 cross-relaxation measurements were done in collaboration with the group of L. Hollenberg (Melbourne), the results of which are available in Ref. [59].

4.1 Magnetic noise sensing by NV relaxation

T_1 relaxation

After initializing a spin ensemble to some magnetization vector $\vec{M}$, the longitudinal spin relaxation time T_1 describes the rate at which the longitudinal magnetization component M_z decays to the thermal equilibrium magnetization (set by temperature and magnetic field). We can write this as $M_z(t) = M_z^{eq} + (M_z^i - M_z^{eq})e^{-t/T_1}$, where M_z^i is the initial magnetization and M_z^{eq} is the thermal (final) magnetization. For NV centers, two-phonon Raman and Orbach decay and magnetic dipole transitions contribute to NV T_1 decay at room temperature. Most diamond samples (except those with very high NV density) have comparable room-temperature T_1 ($\sim$5 ms) because phonon-induced decay dominates. However, T_1 saturates at a sample-dependent maximum value at cryogenic temperatures, an effect which is perhaps related to NV concentration [56].

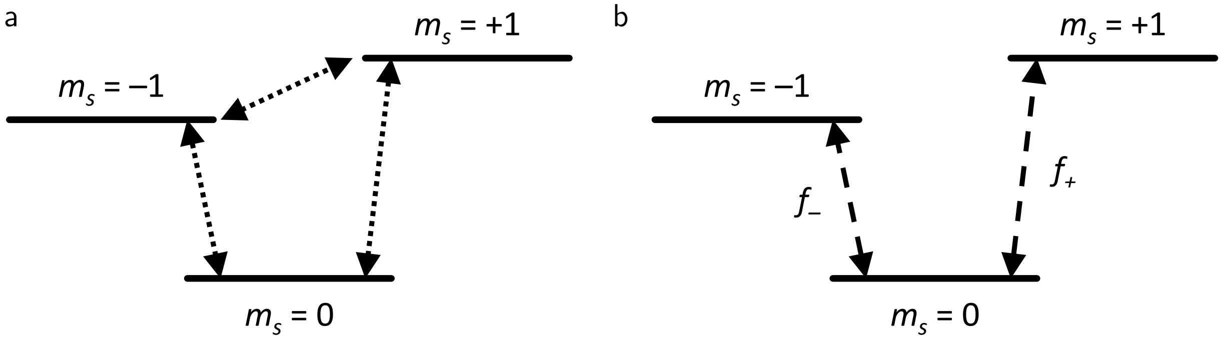

Figure 4.1: (a) T_1 decay from phonons. Here, each m_s state has a comparable lifetime. (b) T_1 decay from magnetic-dipole transitions, which conserve m_s. Depending on the magnetic noise frequency power spectrum, one or both frequencies transitions can have enhanced decay, and the individual m_s states can have different lifetimes.

In addition to exploring NV T_1 properties, previous experiments have used T_1 decay to sense GHz-frequency magnetic noise, such as from paramagnetic defects (P1, Gd^{3+}, Mn^{2+}, and other NV centers) and magnetic Johnson noise [53, 56–58]. The magnetic noise drives ${}^3A_2$ magnetic dipole transitions between $m_s = 0$ and ±1, spoiling the polarization. We can tune the ${}^3A_2$ transition frequencies by adjusting a bias magnetic field, allowing us to sense magnetic noise at arbitrary frequencies. However, ${}^3A_2$ is a three-level system, making theoretical descriptions more complicated. With white noise, both transitions respond to roughly the same magnetic noise amplitude. Alternatively, one transition may experience both cross-relaxation and phonon decay while the other has only phonon decay.

T_2 relaxation

The transverse relaxation time T_2 describes the decay rate for a transversely-magnetized spin ensemble. This is written as $M_\perp(t) = M_\perp^i e^{-t/T_2}$, where $M_\perp(t)$ is the transverse magnetization (which decays to zero at thermal equilibrium) and $M_\perp^i$ is the initial transverse magnetization. In principle, T_2 can be as long as $2T_1$, but often in practice $T_2 \leq T_1$ [41]. The longest NV ensemble T_2 achieved have been roughly half of T_1 (2 ms at room temperature, 0.6 s at 77 K), and this is easiest to achieve in ^{13}C-depleted diamond samples with few defects [102, 155]. In diamond samples with the natural ^{13}C abundance (1.1%), T_2 is often ∼10-50 µs for HPHT samples and hundreds of µs for CVD samples, depending on the experiment and sample.

As discussed in Chapter 3, magnetic spins may have different Larmor precession frequencies caused by local environment inhomogeneity. Since each spin precesses at a slightly different frequency, the ensemble $M_\perp$ will decay more rapidly than the individual $M_\perp$ as the magnetizations from the out-of-phase ensemble spins destructively interfere with each other in the lab frame. This is written as the inhomogeneously-broadened transverse relaxation time T_2^*, and the inhomogeneity can be caused by a static magnetic-field gradient or by different magnitudes and phases of AC magnetic fields from other magnetic sources. The inhomogeneity spoils the overall coherence faster than the constituent coherences. We can cancel out this inhomogeneity using NMR dynamical decoupling (DD) pulse techniques (the simplest of which is Hahn echo), which compensates for the DC and AC field inhomogeneity. Applying periodic π-pulses refocuses the spread in NV Larmor precession and removes the ensemble inhomogeneity, extending T_2^* (as measured with Ramsey spectroscopy) to T_2, a quantity that depends on the magnetic inhomogeneity environment and pulse sequence used. When synchronized with an external AC magnetic field, DD pulse sequences are used for NV AC magnetometry [4]. These pulse sequences are tuned to a particular frequency by choosing the duration between microwave pulses, and the frequency selectivity works much like a lock-in amplifier. The longer the AC magnetometry experiment (with more pulses), the narrower the AC magnetometry frequency selectivity.

Decoupling pulse sequences remove noise at most frequencies (and can act like a band-pass filter or lock-in detector). When sensing a coherent field, the experiment and the AC magnetic field are synchronized so that the NVs get the largest phase accumulation. However, DD sequences are also sensitive to asynchronous AC magnetic noise at particular frequencies (Fig. 4.2). This is called electron spin echo envelope modulation (ESEEM) in EPR, and Fig. 4.2 shows examples of extra-rapid NV T_2 decay due to ^{13}C spin-bath precession (1070.8 Hz/G) or 707 kHz applied magnetic noise [41, 157].

Although nuclear spin noise is a limitation when trying to extend NV T_2 and improve coherence and sensitivity, we can use DD to sense and identify these nuclear spins, especially near the diamond surface [60–62]. A similar scheme for detecting paramagnetic spins uses

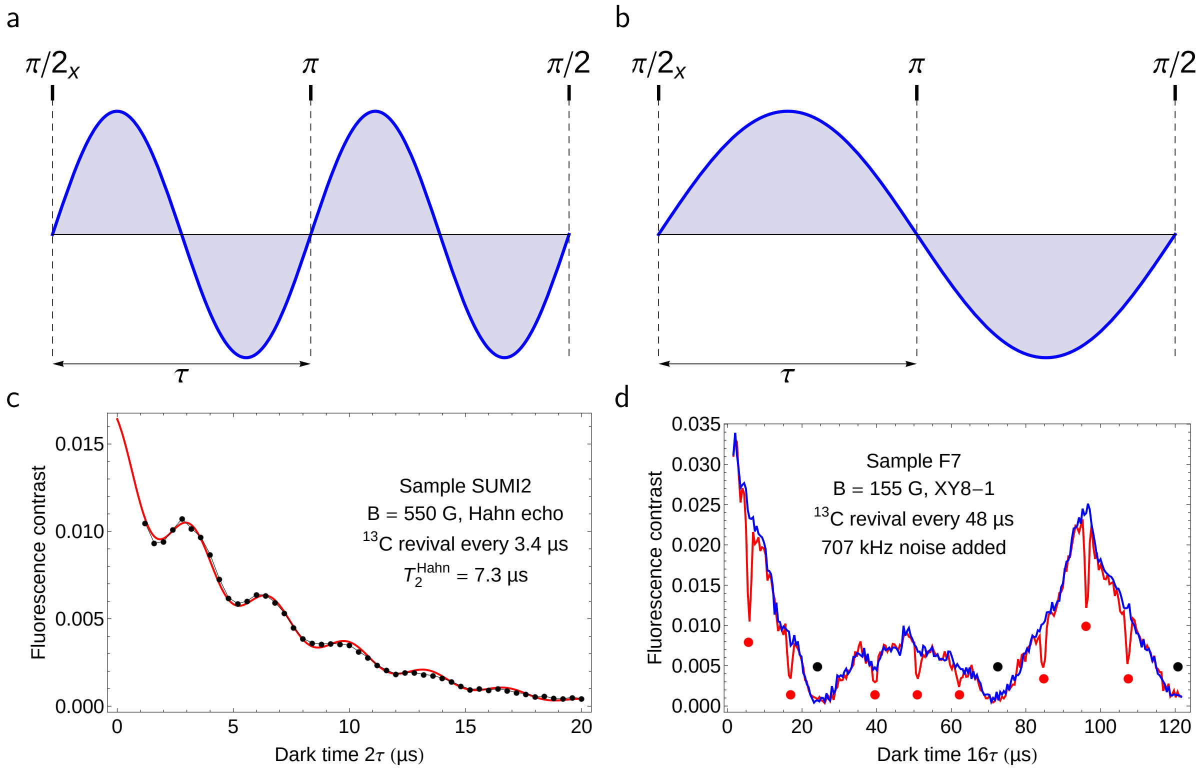

Figure 4.2: (a) An example decoupling sequence (Hahn echo) shown with an AC field from a nucleus. Here, $\tau = 1/f_{AC}$, and the phase accumulation cancels regardless of the relative phase and amplitude. This makes the NVs immune to the ^{13}C spins, restoring coherence for this particular τ (ESEEM). (b) If we instead choose $2\tau = 1/f_{AC}$, then T_2 is maximally spoiled. If the AC field is synchronized with the pulse sequence, this is useful for AC magnetometry, as the additional precession due to the AC field accumulates. (c) Results of a Hahn echo experiment with sample SUMI2 at 550 G ($m_s = 0 \leftrightarrow -1$), showing the ESEEM coherence revivals. To avoid showing a constant offset in NV fluorescence, the difference between Hahn echo experiments ending at $m_s = 0$ and -1 are shown. (d) Results of an XY8-1 experiment with sample F7 ($m_s = 0 \leftrightarrow +1$, blue data), where the coherence is most strongly spoiled for dark times indicated by the black circles. In the red data, we applied 707 kHz magnetic noise, which further spoils the coherence for dark times indicated by the red circles.

double electron-electron resonance (DEER) spectroscopy, where a second microwave π-pulse removes the decoherence effect of on-resonance paramagnetic spins [158].

One disadvantage is that the maximum interrogation time (or minimum Fourier-limited linewidth) is set by the longest-achievable T_2, which is often much shorter than T_1, especially in samples with many paramagnetic or nuclear spins. One way to avoid this is to use correlation spectroscopy techniques instead, which encode the phase accumulation from nuclear spins into M_z and extend the interrogation time to T_1 [64]. Spin noise detection with DD is sensitive to a fundamental frequency and higher harmonics. This can be a problem if trying to sense ^{1}H, as the ^{13}C and ^{1}H gyromagnetic ratios differ by roughly a factor of four, meaning the fourth harmonic of the ^{13}C Larmor frequency can be interpreted as ^{1}H [159]. Correlation spectroscopy is immune to this problem.

Comparison between T_1 and T_2 sensing

Table 4.1 compares the differences between sensing magnetic noise with NV T_1 and T_2. For T_1 sensing, the NV $m_s = 0$ to ± 1 transition frequencies (which are the frequencies at which we listen to magnetic noise) are MHz to GHz, which we tune with an applied magnetic field. A T_2-based dynamical decoupling experiment can only sense frequencies as fast as we can apply microwave π-pulses ($\gtrsim$50 ns), meaning we can sense AC fields with kHz-MHz frequencies. The former lends itself to paramagnetic spin sensing, while the latter is appropriate for nuclear spin sensing with fields of 100-1000 G. Both schemes have limitations; NV T_1 decay sensing competes with phonon-induced decay at room temperature, making sensing additional decay rates weaker than $1/T_1 \approx (5\text{ ms})^{-1}$ challenging. Although longer DD sequences with more pulses yield narrower frequency selectivity and longer T_2, this comes at the expense of decreased final-state fluorescence contrast, since the π-pulses are unable to transfer all NVs with perfect efficiency.

T_1 noise detection	**T_2 noise detection**
Detect MHz-GHz noise	Detect kHz-MHz noise
Sense paramagnetic spins	Sense nuclear spins
Tune by adjusting B	Tune by varying π-pulse spacing
Comparable room-temperature T_1 between samples (few ms)	T_2 depends on sample and pulse sequence (few ms at best)
Compete with phonon-induced decay at room temperature	Lose fluorescence contrast with more π-pulses
Listening to both $m_s = 0 \leftrightarrow \pm 1$	Listening to fundamental and harmonics

Table 4.1: NV T_1 and T_2 magnetic noise detection comparison.

4.2 Previous NV electronic T_1 work

Previous experiments have sensed magnetic noise with NV electronic T_1 [53, 56–58]. Motivated by improving NV ensemble sensitivity, we now seek to understand and characterize T_1 from a basic-physics perspective. A previous experiment [56] studied how T_1 depends on magnetic field, temperature, and sample. Using a bias field along the [111] direction to select one NV orientation, this experiment measured the decaying population differences between $m_s = 0$ and ± 1 states. Since the non-[111] NVs and other defects also fluoresce, this experiment used a common-mode rejection technique (Fig. 4.3), which compared the fluorescence difference for each microwave transition pair ($m_s = 0 \leftrightarrow +1$ and $m_s = 0 \leftrightarrow -1$). This allows us to keep only the fluorescence decay from one transition, rejecting fluorescence decay from other sources and allowing us to use an exponential fit with two free parameters (T_1 and initial amplitude).

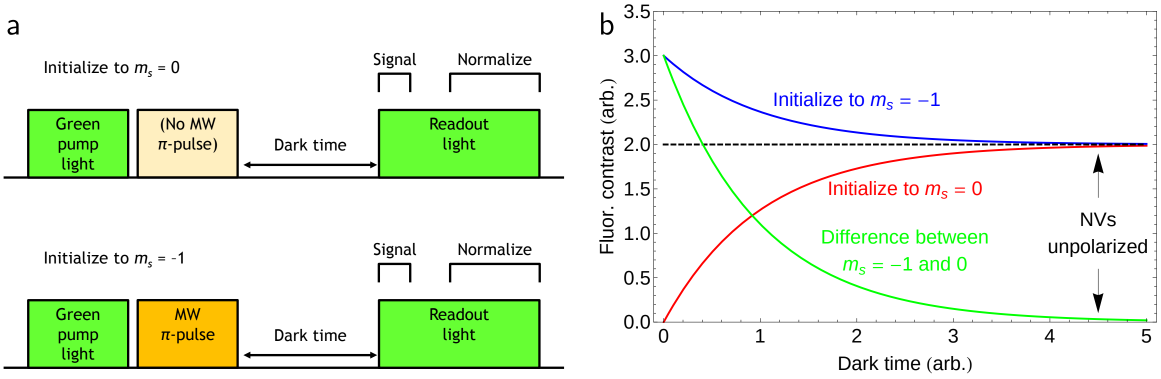

Figure 4.3: (a) An illustration of the T_1 common-mode rejection scheme, where we determine the population relaxation between the $m_s = 0$ and -1 states. (b) Without common-mode rejection (green curve), we would need to include fluorescence offset (when the NVs are depolarized) in the fitting. By taking the difference, we avoid having to include the fluorescence offset or any other fluorescence decay. In addition, common-mode rejection prevents potential systematics from variable π-pulse efficiency.

This experiment showed that the NV $m_s^{NV} = 0 \leftrightarrow -1$ population difference is spoiled when this transition is resonant with the P1 $m_s^{P1} = -1/2 \leftrightarrow +1/2$ transition (near 500 G) or when the [111] and non-[111] NVs are resonant (at 0 G and ~595 G) [56]. However, this experiment used a permanent magnet to set the magnetic field, which had to be physically moved and realigned to change the field. This meant that the B field scan was quite coarse, meaning other possible paramagnetic resonances or fine structure were potentially hidden.

In contrast to the NV center, the P1 center is an optically dark defect with a spin-1/2 electronic ground state and 114 MHz and 81 MHz ^{14}N parallel and perpendicular hyperfine terms [160]. P1 centers are oriented along one of the four diamond orientations due to the Jahn-Teller effect [161]. Figure 4.4 shows the $m_s^{NV} = 0 \leftrightarrow -1$ and $m_s^{P1} = -1/2 \leftrightarrow +1/2$ transition frequencies. For B along the [111] direction, this yields different behavior for the [111]-aligned P1s and the three degenerate non-[111] P1 orientations. The above transitions conserve P1 ^{14}N nuclear spin (m_I^{P1}), though non-m_I^{P1}-conserving transitions are also possible. A previous experiment measuring NV fluorescence as a function of magnetic field also saw evidence of NV-P1 cross-relaxation manifested as reduced NV optical pumping efficiency near 514 G (since the polarization was leaking into the P1 centers) [113]. We now repeat this by studying the NV-P1 cross relaxation directly by measuring the NV T_1 near 500 G and comparing to a first-principles theoretical model for how P1 should cause NV cross-relaxation.

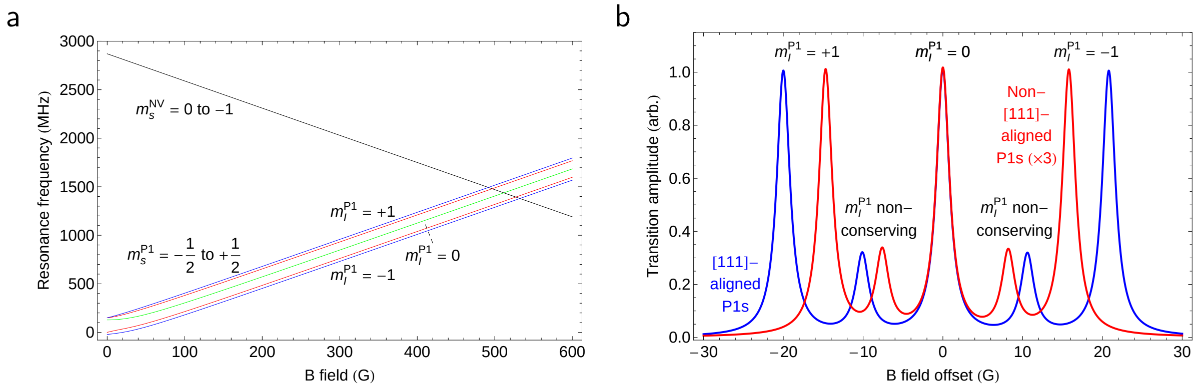

Figure 4.4: (a) Magnetic sublevel transition frequencies for NV and P1 centers as a function of axial magnetic field (B), which cross near 514 G. The m_I^{P1}-conserving transitions for [111]-aligned and non-[111]-aligned P1 centers are shown. The NV ^{14}N hyperfine structure (∼2.2 MHz) and ^{14}N Zeeman splitting (<1 MHz). (b) A drawing of NV-P1 resonance amplitudes, including non-m_I^{P1}-conserving transitions. The transition amplitudes for the non-[111]-aligned P1 centers should be stronger, as these P1s are three times more common.

Our T_1 B-dependence measurements had the following improvements and goals:

- By replacing the permanent magnet with a solenoid driven with a computer-controlled current source, we can vary the axial magnetic field from 0 to 560 G in 0.1 G steps. This lets us map the NV-P1 crossing with high frequency resolution and search the 0-500 G region for NV T_1 relaxation from other paramagnetic centers. We measured T_1 as a function of B at room-temperature and at cryogenic temperature (77 K).

- By adjusting the applied magnetic field, we can use NV T_1 decay to listen to different noise frequencies as a "noise spectrometer." By comparing theoretical predictions for how P1 contributes to NV T_1 decay with our experimental data, we can check how well an NV noise spectrometer is able to sense an arbitrary magnetic noise spectrum [53, 162].

- While NV T_1 decay is appealing as a sensing tool, our understanding of NV T_1 and our methods for measuring it in an ensemble are incomplete. Although we use common-mode rejection to query one of the NV sublevel transitions, $^3A_2$ is really a three-level system, meaning the $m_s = 0$ to $+1$ population is affected when the $m_s = 0$ to -1 transition experiences cross-relaxation with P1. Measuring individual m_s lifetimes would be more ideal, as this simplifies how we extract the magnetic noise amplitude at each transition frequency. However, this is challenging to implement in an ensemble. Furthermore, while we suspect that cryogenic T_1 and T_1 at $B = 0$ depend on NV density, we do not fully understand why. Understanding NV T_1 is important, as it is an ultimate limitation for NV T_2 and sensitivity.

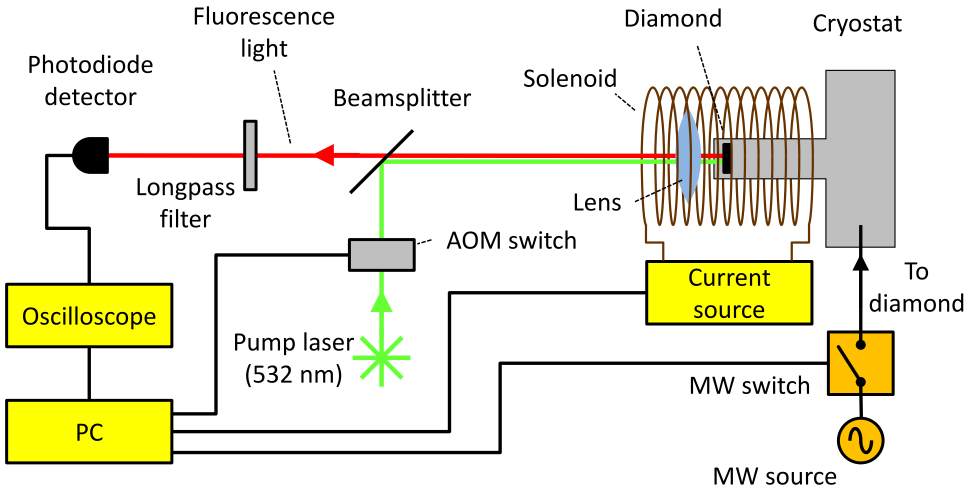

Figure 4.5: Schematic for NV T_1 measurements. The cryostat is a Janis ST-500 continuous flow cryostat, and the microwave wire is not shown. The AOM and MW switch are controlled by TTL pulses. The diamond sample is polished along the [111] plane, and the solenoid applies a magnetic field along the N-V axis for one NV subensemble.

4.3 Experimental details and results

Equipment and samples

We tested two HPHT diamond samples (SUMI2 and F10), described in Tab. 4.2. The samples were mounted on a cryostat cold finger (cooled with liquid nitrogen) with thermally-conductive indium (Fig. 4.5). The cryostat allows optical access through a 1 mm glass window, and we used lenses with few-mm working distance outside the cryostat in the confocal setup. A solenoid driven by a computer-controlled current source (B&K Precision 9123A) surrounded the sample, which set the magnetic field. The acousto-optic modulator (AOM) and microwave switch (Mini-Circuits ZASWA-2-50DR+) were controlled by a TTL pulse generator (programmed with LabVIEW). A fast photodiode (ThorLabs APD110A, 50 MHz bandwidth) measured the NV fluorescence, which was read and averaged with an oscilloscope. For low-density samples, we used a fiber-coupled single-photon counter module (Excelitas SPCM-AQRH-12-FC) and a National Instruments DAQ for acquisition. All measurements were photon-noise limited.

Sample	**[N] (ppm)**	**[NV$^-$] (ppm)**
SUMI2	50	1-10 (gradient)
F10	<200	∼1

Table 4.2: Sample specifications for T_1 and T_2 measurements near 500 G. Sample SUMI2 was unevenly irradiated and has a gradient in NV density.

T_1 measurements

I used the following algorithm to set up NV electronic T_1 measurements:

1. After building and aligning the setup, I measured the NV optical pumping time by using the AOM to turn on the 532 nm pump light for 100 µs and collecting the NV fluorescence intensity. The NVs are fully pumped to the $m_s = 0$ state when the fluorescence saturates to a maximum. After pumping, I turned off the AOM for 20 ms ($\gg T_1$) to allow the NVs to randomize before repeating. After establishing the optical pumping time, I set the "signal" and "normalization" time windows (Fig. 4.3a) in the acquisition software to read out the NV final states at the end of an experiment. We obtained ∼10 µs optical pump time with ∼10 mW of 532 nm laser light.

2. Next I set up CW ODMR experiments, where I aligned the solenoid magnetic field along the [111] direction. To do this, I tilted the coil until the three non-[111] ODMR peaks became degenerate. A non-degenerate orientation with a different transition frequency indicates that the field is not the same for all three non-[111] orientations. Overlapping these peaks signifies that all three orientations experience the same $\vec{B}$, meaning that $\vec{B}$ is along the [111] direction for the fourth orientation (being tested). While there are other alignment methods [113, 163], the above method proved sufficient; intentionally misaligning $\vec{B}$ did not significantly change our T_1 results.

3. I then calibrated the coil magnetic field to yield a gauss/amp conversion and to calculate NV transition frequencies as a function of coil current. I did this either with a "pulsed-Rabi" experiment, where I adjusted the microwave frequency until the Rabi oscillations on the oscilloscope screen were optimized, or by doing CW ODMR experiments at different coil currents. This calibration was included in the T_1 acquisition software to anticipate the NV transition frequencies at each coil current.

4. Given the coil calibration, I did pulsed-Rabi experiments to calibrate the π-pulse duration as a function of current. This was important for getting good fluorescence contrast

in the $m_s = \pm 1$ states (especially near 500 G, which has poor optical pumping efficiency) because our microwave setup had frequency-dependent power delivered to the NVs due to etaloning. This calibration is also used in the T_1 experiments.

5. After finishing the calibrations, I started the NV T_1 measurements. The acquisition software stepped through the run parameters as follows: pick a current, pick a microwave frequency (if measuring multiple transitions), pick a dark time, pick if the π-pulse is enabled or disabled (to initialize to each m_s state), and measure the resulting fluorescence contrast. The experiment was automated and continued until T_1 data was collected for each current. The resulting data (fluorescence contrasts at different dark times) were analysed in post. The water-cooled solenoid dissipated ∼100 W at the highest currents, and the control software monitored the coil temperature and paused the experiment if the coil became too warm, turning off the coil current and allowing it to cool before continuing.

For each T_1 experiment, the program compares the fluorescence between $m_s = 0$ and $m_s = \pm 1$ initial states (MW π-pulse off and MW π-pulse on) for a list of dark times. I chose the dark times to range as long as $5T_1$, which requires a prior guess for T_1. If the guess is too short, the measurements will not have much fluorescence contrast decay, and the resulting exponential fit will be challenging. Similarly, if the guess is too long, most of the measurements will yield near-zero fluorescence contrast, and fitting will also be challenging. To solve this, I used an "adaptive T_1" scheme, which works as follows:

- Make initial guesses for T_1 at each magnetic field.
- Using these guesses, generate lists of dark times up to $5T_1$ and measure T_1 at each magnetic field.
- Fit these measurements to extract T_1 as a function of B for the newest experiment.
- Repeat until the resulting T_1 measurements converge.

Theoretical overview for NV-P1 crossing

We collaborated with the group of L. Hollenberg (Melbourne) to interpret the NV T_1 data from a theoretical perspective [59]. According to their model, a P1 center causes additional T_1 decay with rate

$$2B_\perp^2 \frac{\Gamma_2}{\delta^2 + \Gamma_2^2}, \tag{4.1}$$

where δ is the difference between the NV and P1 transition frequencies, $\Gamma_2 = 1/T_2^*$ is the NV dephasing rate, and $B_\perp$ is the transverse magnetic field the NV experiences from the P1 (in units of hertz). The NVs thus act as a tunable filter function (with width T_2^*) for GHz-frequency magnetic noise.

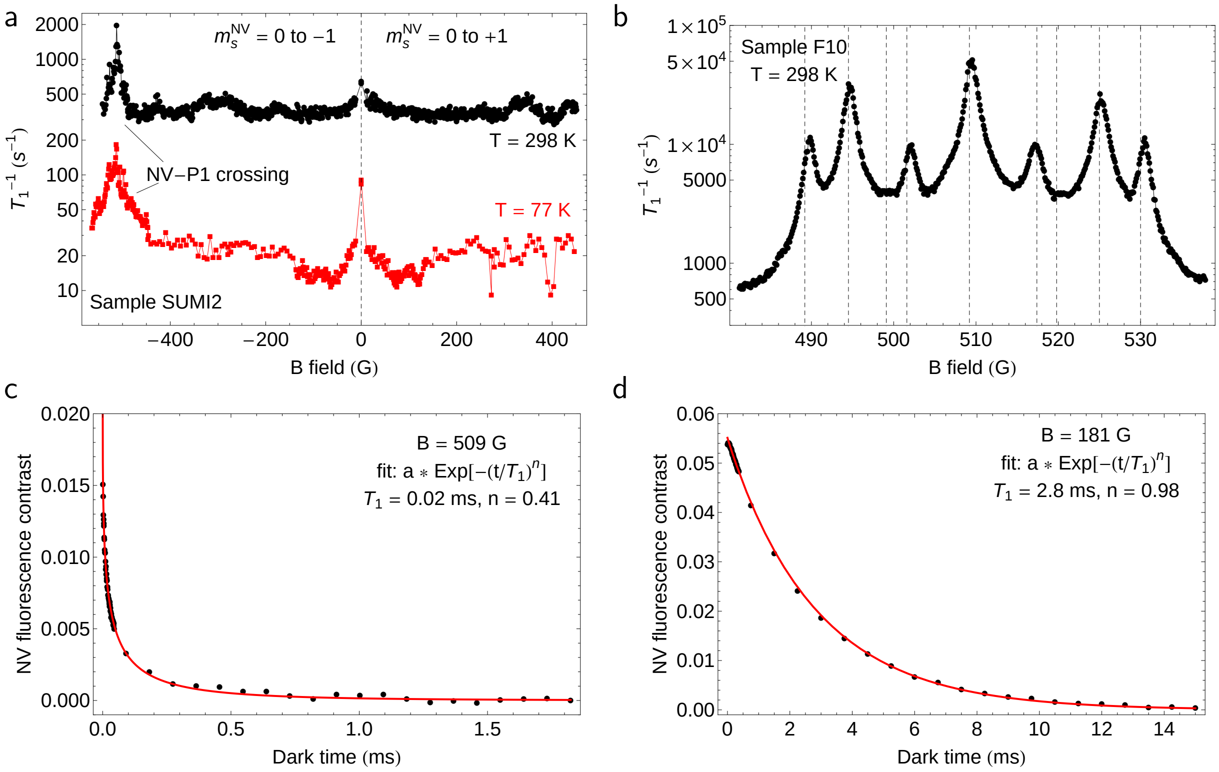

Figure 4.6: (a) T_1 for sample SUMI2 at room temperature and at 77 K, determined using an exponential fit. (b) T_1 for sample F10 at room temperature, determined using a stretched exponential fit (due to non-exponential decay near 500 G). The dashed vertical lines indicate the NV-P1 resonances (Fig. 4.4), and it is difficult to discern the m_I^{P1} non-conserving resonances. (c) An example of non-exponential T_1 decay at 509 G (room temperature). The dark times range up to $5T_1$, though since some NVs decay especially fast near the NV-P1 crossing, I included extra-short dark times to capture these non-exponential dynamics. (d) An example of exponential T_1 decay at 181 G (room temperature), where phonons dominate the T_1 decay processes.

To obtain a magnetic noise spectral density, we must process our NV polarization decay data with the following considerations:

- Since the filter function in Eq. 4.1 samples magnetic noise with a “point-spread function” of frequency width $1/T_2^*$, we must deconvolve our experimental population decay data. We used a deconvolution scheme that attempts to minimize the effect of photon shot noise.

- Equation 4.1 is written for one particular noise frequency, but we have several possible NV-P1 resonance frequencies because of the P1 hyperfine structure, orientations, and the m_I^{P1} non-conserving transitions (Fig. 4.4).

- The NV-P1 coupling strength $B_\perp$ depends on their relative separation, which is different for each NV in our ensemble measurement. This and the previous detail give rise to the non-exponential population decay shown in Fig. 4.6c, compared to ordinary exponential decay when phonon-induced decay dominates (Fig. 4.6d).

Taking these complications into consideration, our collaborators were able to calculate a P1 magnetic noise spectral density and showed good agreement with a predicted spectral density. This validates the T_1 noise spectrometer from a theoretical perspective, and also allows us to predict an ensemble mean NV-P1 distance of 2.7 nm from the noise spectral density.

T_2^* and T_2^{Hahn} measurements near 500 G

In addition to spoiling the NV T_1, P1 centers also spoil NV T_2 and T_2^* when on resonance (Fig. 4.7). Using Ramsey spectroscopy and Hahn echo, I measured T_2 and T_2^* at room temperature near the NV-P1 crossings. To avoid having to differentiate between T_2^* decay and Ramsey oscillations from microwave frequency detuning (from miscalibration), I intentionally detuned the microwave frequency, then determined T_2^* by fitting the decay constant of the resulting few-MHz oscillations in fluorescence. In the Hahn-echo experiment, I took differences between measurements putting the NV spins on the $m_s = 0$ or -1 final states by using both $[\frac{\pi}{2}, \pi, \frac{\pi}{2}]$ and $[\frac{\pi}{2}, \pi, -\frac{\pi}{2}]$ pulse sequences. Like the T_1 common-mode rejection scheme described above, this allows us to fit coherence decay to zero (example shown in Fig. 4.2c). Sample SUMI2, which has inhomogeneous NV density, yielded a range of T_2 times (from 2 to 8 μs) depending on the location on the sample. We chose to do more detailed analysis on a spot with 8 μs T_2 for technical reasons.

From Fig. 4.7, we see that P1 centers affect the NV transverse relaxation as well as longitudinal relaxation, though comparing T_2^* and T_2^{Hahn} for SUMI2, the P1 centers spoil T_2^{Hahn} more drastically. This also suggests that P1 centers are not the dominant contributors to NV T_2^*, with ^{13}C contributing additional broadening. This is to be expected; in a sample with 10 ppm P1 concentration and 1.1% ^{13}C, the typical magnetic fields an NV experiences from nearby P1 and ^{13}C are comparable.

4.4 Summary

We measured NV T_1 and T_2 relaxation near 500 G and observed NV-P1 cross-relaxation and magnetic noise. Together with theoretical framework from the group of L. Hollenberg, we showed that NV T_1 measurements are a useful magnetic noise spectrometer for MHz-GHz frequencies. We found good agreement between the expected magnetic noise spectral density from an ensemble of P1 centers and the noise density extracted from NV T_1 measurements [59]. We hope to extend this work to detect and identify other paramagnetic spins a few

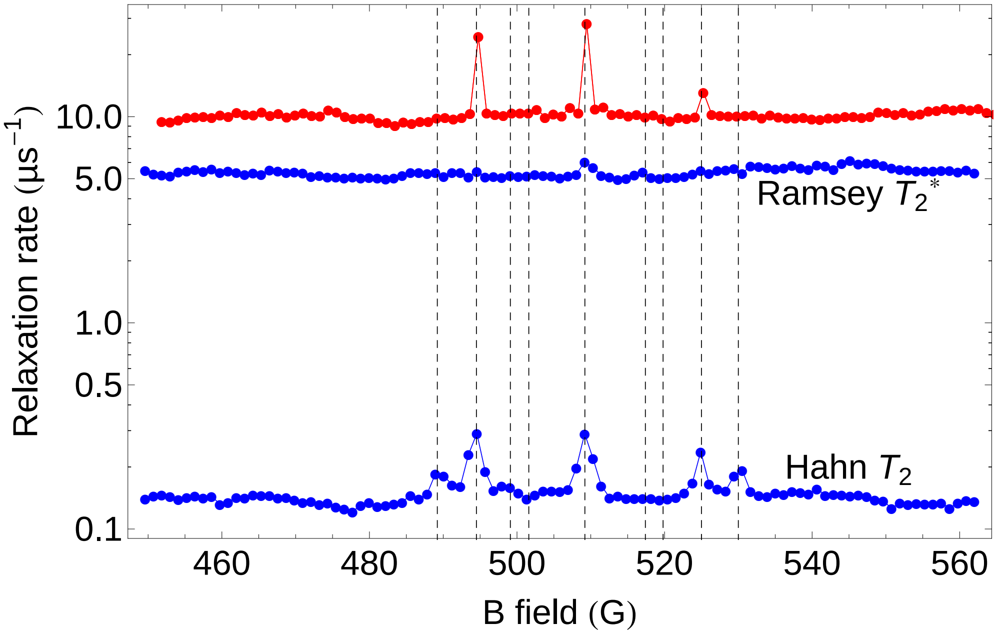

Figure 4.7: T_2^* and T_2^{Hahn} for samples SUMI2 (blue) and F10 (red) near 500 G (room temperature). I detuned the microwave frequency by 5 MHz (SUMI2) and 3 MHz (F10) in the Ramsey experiments to more clearly separate the T_2^* decay from the effect of unintentional microwave frequency detuning.

nanometers away from NVs and to use this technique to gauge the P1 (or other paramagnetic defect) density in our samples. We also found that P1 centers spoil the NV T_2^* and T_2^{Hahn} when on resonance.

Other open questions on NV T_1 physics remain, including how to measure the individual NV m_s lifetimes in an ensemble and what limits T_1 at low temperature and magnetic field. These are the subject of ongoing work.

Chapter 5

Summary and Outlook

5.1 Summary

With recent developments in NV sensing and quantum information applications, it continues to be an interesting time for studying NV centers. However, much of the NV basic physics remains unknown, which could prevent us from exploiting NVs to their full potential. In the above work, I described several experiments (singlet spectroscopy, microwave saturation spectroscopy, and T_1 relaxometry) that aim to clarify NV basic properties and extend the scope of NV sensing methods. In this summary, I discuss additional measurements and future directions for these experiments, progress on two additional ongoing topics, and an outlook on future challenges for NV sensing.

Singlet absorption spectroscopy

In this experiment, we studied the ${}^1E \to {}^1A_1$ PSB and searched for the ${}^1E \to {}^1E'$ ZPL by measuring optical absorption. Although we expected the ${}^1A_1$ and ${}^3A_2$ states to have similar phonon modes, we found that ${}^1A_1$ has higher energy phonons (including a narrow 169 meV localized phonon mode). This suggests that ${}^1A_1$ and ${}^3A_2$ have different enough electronic configurations to warrant different phonon modes between the two. This could be because the ${}^1E$ state might have primarily $a_1^2e^2$ configuration, but with some e^4 contribution as well. These measurements supported the NV infrared absorption magnetometer and can be useful for understanding the NV ISC required for optical pumping [119]. There are first-principles vibration calculations for the NV triplet states [108–110]. Similar calculations are not yet available for the singlet states, and the ${}^1E \to {}^1A_1$ PSB measurements can validate such a calculation.

We searched for the ${}^1E \to {}^1E'$ ZPL at energies up to 2.0 eV at 4 K and 2.6 eV at room temperature, but we did not find it. This may be because ${}^1E'$ (and/or ${}^1A_1'$) may lie in the diamond conduction band. Although we expect ${}^1E \to {}^1E'$ and ${}^3A_2 \to {}^3E$ to have similar cross sections (which are $\sim$10× greater than the ${}^1E \to {}^1A_1$ cross section), the diamond samples are opaque to probe light with wavelengths shorter than 637 nm. Furthermore, we must eliminate ${}^3E \rightarrow {}^3A_2$ fluorescence from reaching the detector (or subtract it out), especially for shorter probe wavelengths. Finally, the cryostat we used was not optimized for transmission (we used the same setup as shown in Fig. 4.5). Light collection is especially important for probe wavelengths shorter than 637 nm because ${}^3A_2 \rightarrow {}^3E$ absorption makes the diamond opaque to these probe wavelengths. The follow-up experiment will use a cryostat with a shorter transmission length and a tunable probe laser. The ${}^1E \rightarrow {}^1E'$ absorption transition may be useful for absorption magnetometry, as it should have a stronger absorption cross-section than the ${}^1E \rightarrow {}^1A_1$ transition.

To further constrain information about the NV energy levels, we may attempt the following experiments (illustrated in Fig. 5.1):

- After populating the ${}^1E$ state, we can attempt to drive a ${}^1E \rightarrow {}^3E$ transition. Although this transition will be weak (it does not conserve electron spin), it will immediately tell us the relative energies between the triplet and singlet states. This avoids the uncertainty and model dependence in indirect singlet-triplet energy measurements [30, 103]. Once a ${}^1E \rightarrow {}^3E$ ZPL is detected, a follow-up pulsed experiment can populate the ${}^1E$ state, wait for the ${}^3E$ fluorescence to decay, drive the ${}^1E \rightarrow {}^3E$ transition, and look for ${}^3E \rightarrow {}^3A_2$ fluorescence to prove ${}^3E$ is the final state for the new absorption feature.
- Similarly, at cryogenic temperature we can attempt to drive a ${}^3A_2$-to-singlet transition in a single NV [164]. First, a pump laser drives a cycling transition between the ${}^3A_2$ $m_s = 0$ sublevel and the E_x sublevel of ${}^3E$. This cycling transition is imperfect, and NVs starting in the $m_s = 0$ sublevel eventually end up in the "dark" $m_s = \pm 1$ states [81]. Next, a probe laser drives a ${}^3A_2 \rightarrow {}^1E$ or ${}^3A_2 \rightarrow {}^1A_1$ transition, spoiling the optical pumping and causing the E_x transition to fluoresce. The energy at which the probe laser spoils the optical pumping yields the triplet-singlet energy separation.
- Finding the energy necessary to optically ionize an NV from the ${}^1E$ state will provide a direct measurement of where the singlet states lie with respect to the diamond valence and conduction bands. This could be done with an optical transmission or a photocurrent measurement.

Microwave saturation spectroscopy

Borrowing techniques from atomic physics, we demonstrated microwave saturation spectroscopy in the ${}^3A_2$ ODMR transitions. We used this technique to demonstrate an NV thermometer that is resistant to changes in magnetic field and showed that magnetic inhomogeneity is chiefly responsible for the ODMR broadening. Since microwave hole burning reduces the ODMR width, we showed that this improves thermometer sensitivity when limited by photon shot noise, laser intensity noise, or electronic white noise (where the sensitivity depends on the slope of the ODMR peak).

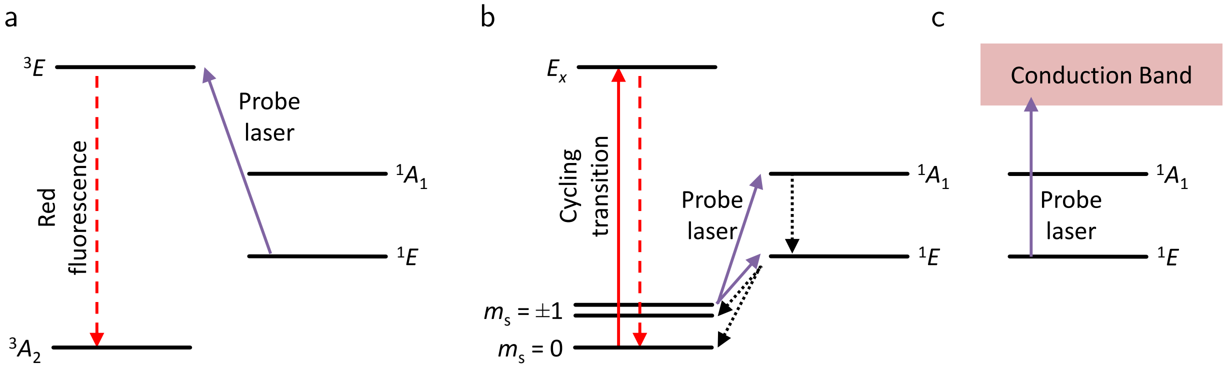

Figure 5.1: (a) A $^1E \rightarrow {}^3E$ absorption transition, which will constrain the NV triplet-singlet energies. Similar to the $^1E \rightarrow {}^1A_1$ experiment, the diamond is more opaque to probe light resonant with the $^1E \rightarrow {}^3E$ when pumped to the ^1E state. We may instead detect $^3E \rightarrow {}^3A_2$ fluorescence (for instance in a pulsed experiment). (b) A similar cryogenic scheme, which searches for $^3A_2$-to-singlet transitions in a single NV. The cycling transition is not perfectly efficient, and the NV is eventually pumped to the $m_s = \pm 1$ "dark" states. However, a $^3A_2$-to-singlet probe laser pumps NVs back to $m_s = 0$ "bright" state, where they again fluoresce in the cycling transition. (c) A ^1E ionization experiment; finding the ionization energy is useful for spin-to-charge or photocurrent readout [121, 123].

We aim to understand what limits the ODMR hole width and to study the diamond spin bath using saturation spectroscopy. Our samples were mainly magnetically-broadened by ^{13}C nuclei and P1 centers. It would be informative to study the opposite case, where strain inhomogeneity dominates (perhaps in nanodiamond samples) and the crossover between the two regimes. Furthermore, samples with different ^{13}C and P1 concentrations are interesting to explore. Finally, although we did not investigate coherent population oscillation by pumping and probing the same microwave transition, this may lead to additional new NV physics.

We attempted two hole burning experiments to study the spin-bath dynamics and magnetic-field correlation time:

- As described in Chapter 3, we can vary the hole chopping frequency. A fast chopping frequency probes one NV frequency class while the inhomogeneous magnetic fields are frozen in time, while a slow chopping frequency is unable to interrogate one frequency class before the selected NVs randomize frequencies, leading to broader hole width with slower chopping frequency. More thorough follow-up experiments (including further increasing the chopping frequency) can yield more information about the spin-bath dynamics and correlation time.

- In a pulsed-hole experiment, we can vary the dark time T_d between the hole and probe pulses (Fig. 3.1b). As the magnetic fields randomize during the dark time, the hole depth and width should fill in at a rate faster than T_1^{-1}. Our attempt to demonstrate this only found NV population decay consistent with T_1 (Fig. 5.3); narrower hole widths (achievable with longer π-pulse duration) may be necessary.

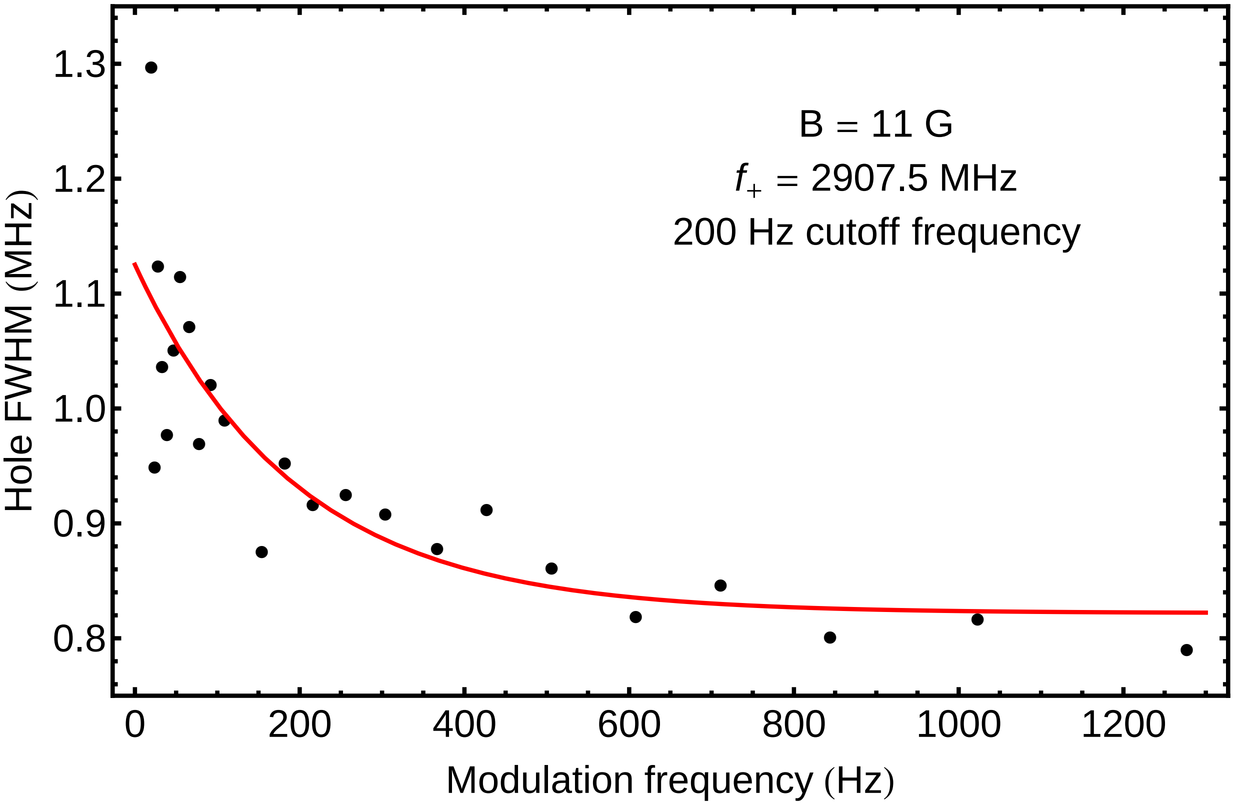

Figure 5.2: Detected hole width as a function of hole microwave chop frequency for sample HPHT2. We expect ~10 ms ^{13}C correlation time and ~10 µs P1 correlation time in this sample. Extending this experiment to higher modulation frequencies, we expect the hole width to narrow further, as the P1 centers become static.

Paramagnetic noise detection with T_1 relaxation

In this experiment, we used NV electronic T_1 relaxation to detect paramagnetic P1 centers through cross-relaxation. By tuning the NV magnetic sublevel transitions, we can listen to magnetic noise at arbitrary frequencies to make a GHz-frequency magnetic noise spectrometer. A T_1 experiment probes a different frequency range than a T_2 experiment, which is better suited for sensing MHz-frequency nuclear-spin magnetic noise.

This experiment measured T_1 for B from 0 to 560 G, and we found NV-P1 cross-relaxation peaks near 510 G corresponding to different P1 orientations, P1 ^{14}N hyperfine structure, and

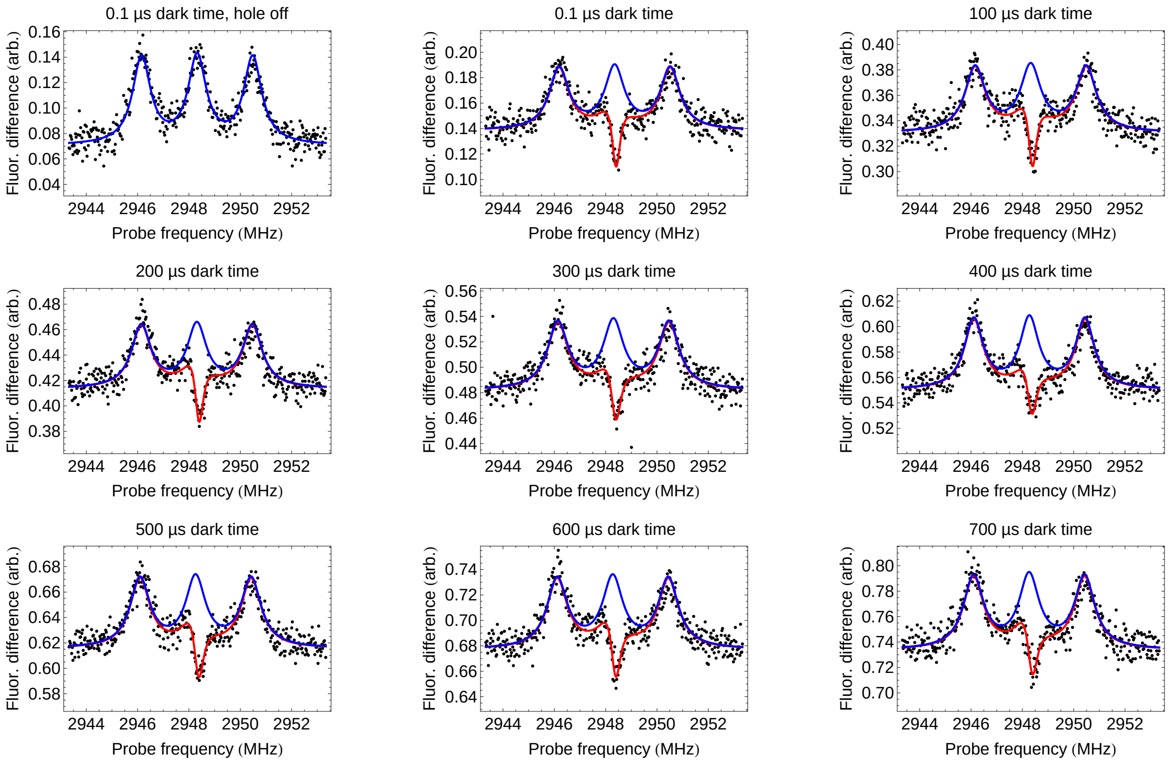

Figure 5.3: An attempt to measure the pulsed-hole lifetime in sample CVD1 by varying the dark time T_d between the hole and probe π-pulses (2 μs duration). Fitting these results showed no discernible change in the hole width while the hole depth decreased by ∼20% at $T_d = 700$ μs (consistent with $T_1 \approx 3$ ms decay).

both m_I^{P1}-conserving and non-m_I^{P1}-conserving NV-P1 resonances. The group of L. Hollenberg developed a method to convert the measured NV $m_s = 0 \leftrightarrow -1$ T_1 relaxation rates into a magnetic noise power spectral density, which has good agreement with a first-principles estimate for P1 spectral noise [59]. Their model also predicted non-exponential NV T_1 decay when on resonance with P1, which we observed experimentally.

While this work extends the interest in NV T_1 magnetic noise sensing, our collaborations with the group of W. Gawlik (Kraków) seek to explain T_1 basic properties, which are a fundamental limitation for NV T_2 and sensitivity. Some of the T_1 "basic physics" questions we aim to answer are listed below:

- After sensing P1 centers by measuring NV-P1 cross-relaxation, we hope to generalize the NV T_1 magnetic noise spectrometer to other paramagnetic spins. Other experiments have sensed paramagnetic spins with nearly white magnetic noise spectra, but we can test other paramagnetic spin species (with longer T_1) to demonstrate how NV T_1 measurements can yield species and density information. This method may provide a complementary technique to ESR sensing, with high spatial resolution and biocompatibility as its main advantages.

- We use the common-mode rejection scheme described in Chapter 4 in ensemble T_1 measurements to remove fluorescence contributions from the undesired NV orientations and other defects. However, this masks the individual m_s lifetimes, which could lead to ambiguity if magnetic noise affects both the $m_s = 0 \leftrightarrow -1$ and $m_s = 0 \leftrightarrow +1$ transition frequencies. In the NV-P1 relaxation example, we would expect the $m_s = 0$ and -1 lifetimes to be short near 500 G, but the $m_s = +1$ lifetime to remain unperturbed by the cross-relaxation. It would therefore be interesting to extract m_s lifetimes rather than measure population decay pairwise for each transition (as with common-mode rejection).
- Similarly, when the $^3A_2$ sublevel transitions are not affected by cross-relaxation (for $B \approx$ 100-400 G) and T_1 is dominated by phonon relaxation, it would be interesting to test verify that each m_s state has the same lifetime. Analyzing the individual m_s decay, we can tentatively suggest that each m_s state has the same lifetime, but this should no be longer true when we introduce magnetic noise.
- We have been studying how NV-NV cross-relaxation affects T_1. We can investigate this by studying T_1 for $B = 0$ and 595 G in samples with different NV densities (aligned along the [111] direction), by varying the magnetic field direction between the [100], [110], and [111] directions (bringing NV subensembles with different orientations into resonance) and measuring T_1 for each NV resonance, and by studying spin diffusion by pumping and interrogating different NV volumes.
- At cryogenic temperatures, the maximum-achievable T_1 is sample-dependent and seems to be related to NV density [56]. We seek to explain what mechanism sets the minimum T_1 for an NV ensemble, and how the cryogenic m_s lifetimes at $B = 0$ compare to those at room temperature.

5.2 Ongoing work

Bulk ^{13}C polarization

Conventional NMR uses a strong (∼10 T) magnetic field to thermally polarize nuclei. However, when the magnetic field is near 500 G (the excited-state level anticrossing, or ESLAC) or 1000 G (the ground-state level anticrossing, or GSLAC), NV centers can transfer the optically-pumped electronic polarization to nearby ^{13}C nuclei. This can yield ∼0.5% bulk ^{13}C polarization, a few hundred times greater than thermal polarization with an NMR magnet [65]. The eventual goal is to polarize all of the diamond ^{13}C, then transfer the polarization to nuclei in other molecules of interest. In particular, this would be especially useful if achievable in "supernatural" diamond samples with greater than the natural ^{13}C concentration, including a sample with 99.99% ^{13}C. We are searching for ^{13}C polarization at the ESLAC in this and other supernatural samples.

The NV ODMR in this sample is unusual compared to a 1.1% ^{13}C sample, as seen in Fig. 5.4a. NVs with a ^{13}C in the three locations nearest to the vacancy ("first-shell" sites) have a ∼100 MHz hyperfine splitting, while ^{13}C atoms in other lattice sites cause $\lesssim$10 MHz hyperfine splittings [43]. Similar to the NV ^{14}N and ^{13}C ESLAC polarization we tried in natural-abundance diamond [165], we searched for nuclear polarization in this sample with three methods:

- If the first-shell ^{13}C nuclei are polarized, their corresponding ODMR peak depths will change to reflect the new population (5.4b).
- If the non-first-shell ^{13}C nuclei are polarized, this may lead to reduced inhomogeneous widths for the four first-shell ODMR peaks, as the non-first-shell ^{13}C magnetic fields are no longer random (5.4c).
- If the non-first-shell ^{13}C nuclei are polarized, they may generate an additional magnetic field, which the NV centers will react to. This will appear as a nonlinearity in the $m_s = 0 \leftrightarrow -1$ transition frequencies near 500 (5.4d).

As seen in Fig. 5.4, bulk ^{13}C polarization was not detected. This may be because the ESLAC polarization transfer is sensitive to transverse magnetic fields, and the ^{13}C sample has ∼100 MHz of magnetic inhomogeneity compared to ∼1 MHz in a natural-abundance sample. Furthermore, ^{13}C nuclei at different lattice sites polarize in opposite directions, causing cancellation in the overall ^{13}C polarization [43]. We found similar results in a 10% ^{13}C sample, and plan to continue searching for ^{13}C polarization in other supernatural diamond samples.

NV rotation sensing

NV rotation sensing may work in three possible ways [166–169]:

- Dynamical phase accumulation - if an NV rotates about its z-axis, the $^3A_2$ $m_s = 0$ to ±1 transitions will shift by the rotation frequency. This is because when transforming to the rotating frame, the rotating-frame Hamiltonian contains an additional term $\Omega_{rot} S_z$, where Ω_{rot} is the rotation angular frequency and S_z is the z-axis spin-projection operator [41]. The phase accumulation caused by rotation about z is called dynamical phase [170].
- Geometric phase accumulation - if an NV rotates about an axis other than the z-axis, its magnetic sublevels will accumulate geometric phase instead [170].
- Non-Abelian geometric phase accumulation - an NV center can have non-Abelian geometric phase accumulation if the $m_s = 0$ and -1 states are degenerate. This occurs

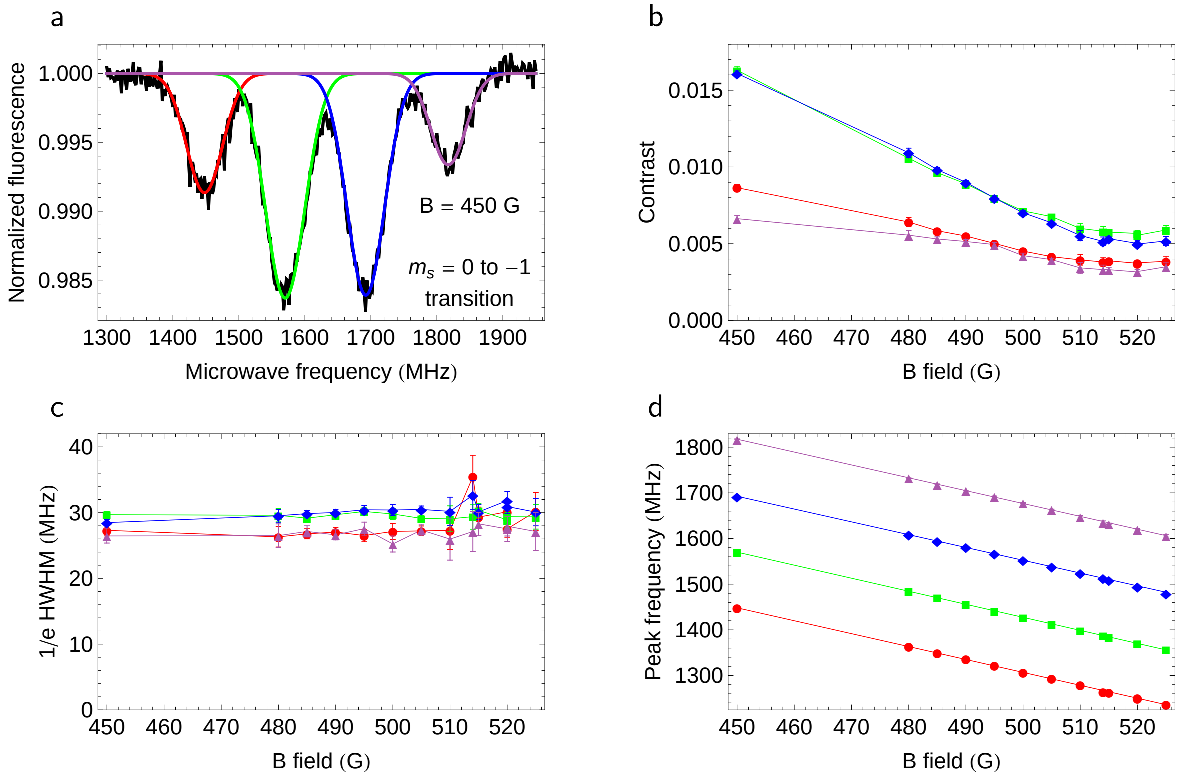

Figure 5.4: (a) An example ^{13}C ODMR plot, illustrating the four peaks corresponding to the first-shell ^{13}C states and the extensive inhomogeneous broadening from other ^{13}C nuclei. The two outer peaks correspond to the first-shell ^{13}C nuclei being all spin up or spin down, and the middle two correspond to two of three nuclei being spin up or spin down. The color scheme for the fits is consistent in all of the plots. (b) First-shell ODMR peak contrasts. The overall contrast decreases because of the ESLAC and the NV-P1 crossing, but a deviation in relative peak heights would indicate a change in the first-shell ^{13}C spin-state populations. (c) First-shell ODMR peak widths. A reduced width may indicate reduced inhomogeneous broadening from polarized ^{13}C nuclei. (d) First-shell ODMR peak center-frequencies. Any nonlinearity may suggest a magnetic field contribution from bulk ^{13}C polarization.

at the ground-state level anticrossing (GSLAC) when the axial magnetic field is near 1020 G. The phase accumulation from two rotations may depend on their order, and this scheme may have the added benefit that the NV coherence requirement becomes T_1 instead of T_2^* or T_2 [169].

We hope to implement an NV ensemble gyroscope, using either NV electron spins, NV ^{14}N spins, or polarized ^{13}C spins as rotation sensors. While electronic spins are simplest to polarize and read out, nuclear spins have better coherence times; ^{14}N lifetime measurements for an NV ensemble are ongoing.

5.3 Outlook

I described three NV experiments (and two ongoing pursuits), each of which sheds light on NV physics and contributes to the library of NV sensing techniques. In addition to searching for additional NV singlet states, our NV singlet spectroscopy measurements may constrain the singlet-triplet energy separations and the ^1E ionization energy. With microwave saturation spectroscopy, we hope to learn new physics by understanding what limits the minimum hole width in an NV ensemble. Following the initial experimental demonstrations and theoretical framework, NV paramagnetic noise detection will expand to being able to sense other paramagnetic spins, distinguish between different spin species, and extract spin concentrations (perhaps for ion channel monitoring) [53]. We seek to answer our remaining fundamental questions about NV T_1 relaxation mentioned above, which may lead to new physics or applications.

NV sensing and quantum information are at an important stage in their development. Following the initial successes of the past decade, NV centers are now a fashionable system to work on as more researchers study them. However, the excitement over NVs may soon dissipate if we do not solve the current sensitivity limitations, facilitate technology transfer to the engineering community, or find a "killer application" for which NV centers are the best solution. Fortunately, as NV researchers continue to invent unique applications (partly enabled by the fact that NVs work in ambient conditions) and have begun forming startup companies to pursue them, I am optimistic that NV sensing could become a standard sensing tool.

Bibliography

[1] R. Schirhagl, K. Chang, M. Loretz, and C. L. Degen, Annual Review of Physical Chemistry **65**, 83–105 (2014).

[2] M. W. Doherty, N. B. Manson, P. Delaney, F. Jelezko, J. Wrachtrup, and L. C. L. Hollenberg, Physics Reports **528**, 1–45 (2013).

[3] L. Rondin, J.-P. Tetienne, T. Hingant, J.-F. Roch, P. Maletinsky, and V. Jacques, Reports on Progress in Physics **77**, 056503 (2014).

[4] J. M. Taylor, P. Cappellaro, L. Childress, L. Jiang, D. Budker, P. R. Hemmer, A. Yacoby, R. Walsworth, and M. D. Lukin, Nat Phys **4**, 810–816 (2008).

[5] F. Dolde, H. Fedder, M. W. Doherty, T. Nöbauer, F. Rempp, G. Balasubramanian, T. Wolf, F. Reinhard, L. C. L. Hollenberg, F. Jelezko, and J. Wrachtrup, Nature Physics **7**, 459–463 (2011).

[6] V. M. Acosta, E. Bauch, M. P. Ledbetter, A. Waxman, L.-S. Bouchard, and D. Budker, Phys. Rev. Lett. **104**, 070801 (2010).

[7] D. M. Toyli, C. F. de las Casas, D. J. Christle, V. V. Dobrovitski, and D. D. Awschalom, Proceedings of the National Academy of Sciences **110**, 8417–8421 (2013).

[8] M. W. Doherty, V. V. Struzhkin, D. A. Simpson, L. P. McGuinness, Y. Meng, A. Stacey, T. J. Karle, R. J. Hemley, N. B. Manson, L. C. L. Hollenberg, and S. Prawer, Phys. Rev. Lett. **112**, 047601 (2014).

[9] P. C. Maurer, G. Kucsko, C. Latta, L. Jiang, N. Y. Yao, S. D. Bennett, F. Pastawski, D. Hunger, N. Chisholm, M. Markham, D. J. Twitchen, J. I. Cirac, and M. D. Lukin, Science **336**, 1283–1286 (2012).

[10] W. Pfaff, B. J. Hensen, H. Bernien, S. B. van Dam, M. S. Blok, T. H. Taminiau, M. J. Tiggelman, R. N. Schouten, M. Markham, D. J. Twitchen, and R. Hanson, Science **345**, 532–535 (2014).

[11] Diamond (C) lattice parameters, SpringerMaterials - The Landolt-Börnstein Database, O. Madelung, U. Rössler, and M. Schulz (eds).

[12] A. M. Zaitsev, *Optical Properties of Diamond: A Data Handbook* (Springer, 2001).

[13] P. Maletinsky, S. Hong, M. S. Grinolds, B. Hausmann, M. Lukin, R. L. Walsworth, M. Loncar, and A. Yacoby, Nat. Nano. **7**, 320–324 (2012).

[14] M. Geiselmann, M. L. Juan, J. Renger, J. M. Say, L. J. Brown, F. J. G. de Abajo, F. Koppens, and R. Quidant, Nat Nano **8**, 175–179 (2013).

[15] G. Kucsko, P. C. Maurer, N. Y. Yao, M. Kubo, H. J. Noh, P. K. Lo, H. Park, and M. D. Lukin, Nature **500**, 54–58 (2013).

[16] V. M. Acosta, E. Bauch, M. P. Ledbetter, C. Santori, K.-M. C. Fu, P. E. Barclay, R. G. Beausoleil, H. Linget, J. F. Roch, F. Treussart, S. Chemerisov, W. Gawlik, and D. Budker, Phys. Rev. B **80**, 115202 (2009).

[17] E. Kim, V. M. Acosta, E. Bauch, D. Budker, and P. R. Hemmer, Applied Physics Letters **101**, 082410 (2012).

[18] Y. Chu, N. de Leon, B. Shields, B. Hausmann, R. Evans, E. Togan, M. J. Burek, M. Markham, A. Stacey, A. Zibrov, A. Yacoby, D. Twitchen, M. Loncar, H. Park, P. Maletinsky, and M. Lukin, Nano Letters **14**, 1982–1986 (2014).

[19] K. Ohno, F. J. Heremans, L. C. Bassett, B. A. Myers, D. M. Toyli, A. C. B. Jayich, C. J. Palmstrom, and D. D. Awschalom, Applied Physics Letters **101**, 082413, 082413 (2012).

[20] B. A. Myers, A. Das, M. C. Dartiailh, K. Ohno, D. D. Awschalom, and A. C. Bleszynski Jayich, Phys. Rev. Lett. **113**, 027602 (2014).

[21] L.-J. Su, C.-Y. Fang, Y.-T. Chang, K.-M. Chen, Y.-C. Yu, J.-H. Hsu, and H.-C. Chang, Nanotechnology **24**, 315702 (2013).

[22] P. Andrich, B. J. Aleman, J. C. Lee, K. Ohno, C. F. de las Casas, F. J. Heremans, E. L. Hu, and D. D. Awschalom, Nano Letters **14**, 4959–4964 (2014).

[23] B. J. M. Hausmann, T. M. Babinec, J. T. Choy, J. S. Hodges, S. Hong, I. Bulu, A. Yacoby, M. D. Lukin, and M. Loncar, New Journal of Physics **13**, 045004 (2011).

[24] M. J. Burek, Y. Chu, M. S. Z. Liddy, P. Patel, J. Rochman, S. Meesala, W. Hong, Q. Quan, M. D. Lukin, and M. Loncar, Nature Communications **5** (2014).

[25] F. A. Cotton, *Chemical Applications of Group Theory*, 3rd edition (Wiley-Interscience, 1990).

[26] J. R. Maze, A. Gali, E. Togan, Y. Chu, A. Trifonov, E. Kaxiras, and M. D. Lukin, New Journal of Physics **13**, 025025 (2011).

[27] M. W. Doherty, N. B. Manson, P. Delaney, and L. C. L. Hollenberg, New Journal of Physics **13**, 025019 (2011).

[28] V. M. Acosta, A. Jarmola, E. Bauch, and D. Budker, Phys. Rev. B **82**, 201202 (2010).

[29] L. J. Rogers, S. Armstrong, M. J. Sellars, and N. B. Manson, New Journal of Physics **10**, 103024 (2008).

[30] M. L. Goldman, A. Sipahigil, M. W. Doherty, N. Y. Yao, S. D. Bennett, M. Markham, D. J. Twitchen, N. B. Manson, A. Kubanek, and M. D. Lukin, Phys. Rev. Lett. **114**, 145502 (2015).

[31] N. Aslam, G. Waldherr, P. Neumann, F. Jelezko, and J. Wrachtrup, New Journal of Physics **15**, 013064 (2013).

[32] B. Henderson and G. F. Imbusch, *Optical Spectroscopy of Inorganic Solids* (Oxford University Press, 2006).

[33] M. Fox, *Optical Properties of Solids*, 2nd edition (Oxford University Press, 2010).

[34] S. Choi, M. Jain, and S. G. Louie, Phys. Rev. B **86**, 041202 (2012).

[35] L. Robledo, H. Bernien, T. van der Sar, and R. Hanson, New Journal of Physics **13**, 025013 (2011).

[36] V. M. Huxter, T. A. A. Oliver, D. Budker, and G. R. Fleming, Nat Phys **9**, 744–749 (2013).

[37] A. Faraon, C. Santori, Z. Huang, V. M. Acosta, and R. G. Beausoleil, Phys. Rev. Lett. **109**, 033604 (2012).

[38] A. Batalov, V. Jacques, F. Kaiser, P. Siyushev, P. Neumann, L. J. Rogers, R. L. McMurtrie, N. B. Manson, F. Jelezko, and J. Wrachtrup, Phys. Rev. Lett. **102**, 195506 (2009).

[39] J.-P. Tetienne, L. Rondin, P. Spinicelli, M. Chipaux, T. Debuisschert, J.-F. Roch, and V. Jacques, New Journal of Physics **14**, 103033 (2012).

[40] M. Steiner, P. Neumann, J. Beck, F. Jelezko, and J. Wrachtrup, Phys. Rev. B **81**, 035205 (2010).

[41] M. H. Levitt, *Spin Dynamics: Basics of Nuclear Magnetic Resonance*, 2nd edition (Wiley, 2008).

[42] M. W. Doherty, V. M. Acosta, A. Jarmola, M. S. J. Barson, N. B. Manson, D. Budker, and L. C. L. Hollenberg, Phys. Rev. B **90**, 041201 (2014).

[43] A. Dréau, J.-R. Maze, M. Lesik, J.-F. Roch, and V. Jacques, Phys. Rev. B **85**, 134107 (2012).

[44] V. Acosta, D. Budker, P. Hemmer, J. Maze, and R. Walsworth, "Optical Magnetometry with Nitrogen-Vacancy Centers in Diamond", in *Optical Magnetometry*, edited by D. Budker and D. F. Jackson Kimball (Cambridge, 2013), pp. 142–166.

[45] D. Le Sage, L. M. Pham, N. Bar-Gill, C. Belthangady, M. D. Lukin, A. Yacoby, and R. L. Walsworth, Phys. Rev. B **85**, 121202 (2012).

[46] J. F. Barry et al., in preparation.

[47] D. Le Sage, K. Arai, D. R. Glenn, S. J. DeVience, L. M. Pham, L. Rahn-Lee, M. D. Lukin, A. Yacoby, A. Komeili, and R. L. Walsworth, Nature **496**, 486–489 (2013).

[48] R. R. Fu, B. P. Weiss, E. A. Lima, R. J. Harrison, X.-N. Bai, S. J. Desch, D. S. Ebel, C. Suavet, H. Wang, D. Glenn, D. Le Sage, T. Kasama, R. L. Walsworth, and A. T. Kuan, Science **346**, 1089–1092 (2014).

[49] D. Glenn, D. LeSage, C. Connolly, and R. Walsworth, in DAMOP D1.00089 (2015).

[50] J.-P. Tetienne, T. Hingant, J.-V. Kim, L. H. Diez, J.-P. Adam, K. Garcia, J.-F. Roch, S. Rohart, A. Thiaville, D. Ravelosona, and V. Jacques, Science **344**, 1366–1369 (2014).

[51] L. Rondin, J.-P. Tetienne, S. Rohart, A. Thiaville, T. Hingant, P. Spinicelli, J.-F. Roch, and V. Jacques, Nature Communications **4**, 2279 (2013).

[52] F. Shi, Q. Zhang, P. Wang, H. Sun, J. Wang, X. Rong, M. Chen, C. Ju, F. Reinhard, H. Chen, J. Wrachtrup, J. Wang, and J. Du, Science **347**, 1135–1138 (2015).

[53] S. Steinert, F. Ziem, L. T. Hall, A. Zappe, M. Schweikert, N. Götz, A. Aird, G. Balasubramanian, L. Hollenberg, and J. Wrachtrup, Nature Communications **4** (2013).

[54] A. Waxman, Y. Schlussel, D. Groswasser, V. M. Acosta, L.-S. Bouchard, D. Budker, and R. Folman, Phys. Rev. B **89**, 054509 (2014).

[55] E. A. Ekimov, V. A. Sidorov, E. D. Bauer, N. N. Mel'nik, N. J. Curro, J. D. Thompson, and S. M. Stishov, Nature **428**, 542–545 (2004).

[56] A. Jarmola, V. M. Acosta, K. Jensen, S. Chemerisov, and D. Budker, Phys. Rev. Lett. **108**, 197601 (2012).

[57] A. O. Sushkov, N. Chisholm, I. Lovchinsky, M. Kubo, P. K. Lo, S. D. Bennett, D. Hunger, A. Akimov, R. L. Walsworth, H. Park, and M. D. Lukin, Nano Letters **14**, 6443–6448 (2014).

[58] S. Kolkowitz, A. Safira, A. A. High, R. C. Devlin, S. Choi, Q. P. Unterreithmeier, D. Patterson, A. S. Zibrov, V. E. Manucharyan, H. Park, and M. D. Lukin, Science **347**, 1129–1132 (2015).

[59] L. T. Hall, P. Kehayias, D. A. Simpson, A. Jarmola, A. Stacey, D. Budker, and L. C. L. Hollenberg, arXiv:1503.00830 (2015).

[60] H. J. Mamin, M. Kim, M. H. Sherwood, C. T. Rettner, K. Ohno, D. D. Awschalom, and D. Rugar, Science **339**, 557–560 (2013).

[61] T. Staudacher, F. Shi, S. Pezzagna, J. Meijer, J. Du, C. A. Meriles, F. Reinhard, and J. Wrachtrup, Science **339**, 561–563 (2013).

[62] S. J. DeVience, L. M. Pham, I. Lovchinsky, A. O. Sushkov, N. Bar-Gill, C. Belthangady, F. Casola, M. Corbett, H. Zhang, M. Lukin, H. Park, A. Yacoby, and R. L. Walsworth, Nature Nanotechnology **10**, 129–134 (2015).

[63] M. S. Grinolds, M. Warner, K. D. Greve, Y. Dovzhenko, L. Thiel, R. L. Walsworth, S. Hong, P. Maletinsky, and A. Yacoby, Nature Nanotechnology **9**, 279–284 (2014).

[64] A. Laraoui, F. Dolde, C. Burk, F. Reinhard, J. Wrachtrup, and C. A. Meriles, Nature Communications **4**, 1651 (2013).

[65] R. Fischer, C. O. Bretschneider, P. London, D. Budker, D. Gershoni, and L. Frydman, Phys. Rev. Lett. **111**, 057601 (2013).

[66] C. Belthangady, N. Bar-Gill, L. M. Pham, K. Arai, D. Le Sage, P. Cappellaro, and R. L. Walsworth, Phys. Rev. Lett. **110**, 157601 (2013).

[67] P. London, J. Scheuer, J.-M. Cai, I. Schwarz, A. Retzker, M. B. Plenio, M. Katagiri, T. Teraji, S. Koizumi, J. Isoya, R. Fischer, L. P. McGuinness, B. Naydenov, and F. Jelezko, Phys. Rev. Lett. **111**, 067601 (2013).

[68] H. Bernien, B. Hensen, W. Pfaff, G. Koolstra, M. S. Blok, L. Robledo, T. H. Taminiau, M. Markham, D. J. Twitchen, L. Childress, and R. Hanson, Nature **497**, 86–90 (2013).

[69] Y. Makhlin, G. Schön, and A. Shnirman, Rev. Mod. Phys. **73**, 357–400 (2001).

[70] C. Gerry and P. Knight, *Introductory Quantum Optics* (Cambridge University Press, 2004).

[71] J. J. Garcia-Ripoll, P. Zoller, and J. I. Cirac, Journal of Physics B: Atomic, Molecular and Optical Physics **38**, S567 (2005).

[72] M. Fleischhauer, A. Imamoglu, and J. P. Marangos, Rev. Mod. Phys. **77**, 633–673 (2005).

[73] A. Imamoglu, D. D. Awschalom, G. Burkard, D. P. DiVincenzo, D. Loss, M. Sherwin, and A. Small, Phys. Rev. Lett. **83**, 4204–4207 (1999).

[74] J. J. Pla, F. A. Mohiyaddin, K. Y. Tan, J. P. Dehollain, R. Rahman, G. Klimeck, D. N. Jamieson, A. S. Dzurak, and A. Morello, Phys. Rev. Lett. **113**, 246801 (2014).

[75] J. J. Pla, K. Y. Tan, J. P. Dehollain, W. H. Lim, J. J. L. Morton, D. N. Jamieson, A. S. Dzurak, and A. Morello, Nature **489**, 541–545 (2012).

[76] A. Sipahigil, K. D. Jahnke, L. J. Rogers, T. Teraji, J. Isoya, A. S. Zibrov, F. Jelezko, and M. D. Lukin, Phys. Rev. Lett. **113**, 113602 (2014).

[77] A. L. Falk, B. B. Buckley, G. Calusine, W. F. Koehl, V. V. Dobrovitski, A. Politi, C. A. Zorman, P. X.-L. Feng, and D. D. Awschalom, Nature Communications **4**, 1819 (2013).

[78] C. Simon, M. Afzelius, J. Appel, A. Boyer de la Giroday, S. J. Dewhurst, N. Gisin, C. Y. Hu, F. Jelezko, S. Kröll, J. H. Müller, J. Nunn, E. S. Polzik, J. G. Rarity, H. De Riedmatten, W. Rosenfeld, A. J. Shields, N. Sköld, R. M. Stevenson, R. Thew, I. A. Walmsley, M. C. Weber, H. Weinfurter, J. Wrachtrup, and R. J. Young, The European Physical Journal D **58**, 1–22 (2010).

[79] D. Farfurnik, A. Jarmola, L. M. Pham, Z. H. Wang, V. V. Dobrovitski, R. L. Walsworth, D. Budker, and N. Bar-Gill, arXiv:1505.00636 (2015).

[80] J. P. Hadden, J. P. Harrison, A. C. Stanley-Clarke, L. Marseglia, Y.-L. D. Ho, B. R. Patton, J. L. O'Brien, and J. G. Rarity, Applied Physics Letters **97**, 241901, 241901 (2010).

[81] L. Robledo, L. Childress, H. Bernien, B. Hensen, P. F. A. Alkemade, and R. Hanson, Nature **477**, 574–578 (2011).

[82] G. Waldherr, Y. Wang, S. Zaiser, M. Jamali, T. Schulte-Herbruggen, H. Abe, T. Ohshima, J. Isoya, J. F. Du, P. Neumann, and J. Wrachtrup, Nature **506**, 204–207 (2014).

[83] T. H. Taminiau, J. Cramer, T. van der Sar, V. V. Dobrovitski, and R. Hanson, Nature Nanotechnology **9**, 171–176 (2014).

[84] E. M. Kessler, I. Lovchinsky, A. O. Sushkov, and M. D. Lukin, Phys. Rev. Lett. **112**, 150802 (2014).

[85] D. B. Hume, T. Rosenband, and D. J. Wineland, Phys. Rev. Lett. **99**, 120502 (2007).

[86] G. D. Fuchs, G. Burkard, P. V. Klimov, and D. D. Awschalom, Nature Physics **7**, 789–793 (2011).

[87] S. Arroyo-Camejo, A. Lazariev, S. W. Hell, and G. Balasubramanian, Nature Communications **5**, 4870 (2014).

[88] S. Sangtawesin, T. O. Brundage, and J. R. Petta, Phys. Rev. Lett. **113**, 020506 (2014).

[89] J. Cai, A. Retzker, F. Jelezko, and M. B. Plenio, Nat Phys **9**, 168–173 (2013).

[90] K.-M. C. Fu, C. Santori, P. E. Barclay, I. Aharonovich, S. Prawer, N. Meyer, A. M. Holm, and R. G. Beausoleil, Applied Physics Letters **93**, 234107, 234107 (2008).

[91] R. Mhaskar, S. Knappe, and J. Kitching, Applied Physics Letters **101**, 241105 (2012).

[92] A. Finkler, Y. Segev, Y. Myasoedov, M. L. Rappaport, L. Ne'eman, D. Vasyukov, E. Zeldov, M. E. Huber, J. Martin, and A. Yacoby, Nano Letters **10**, 1046–1049 (2010).

[93] D. Rugar, R. Budakian, H. J. Mamin, and B. W. Chui, Nature **430**, 329–332 (2004).

[94] M. Koschorreck, M. Napolitano, B. Dubost, and M. W. Mitchell, Applied Physics Letters **98**, 074101 (2011).

[95] A. L. Herrera-May, L. A. Aguilera-Cortes, P. J. Garcia-Ramirez, and E. Manjarrez, Sensors **9**, 7785–7813 (2009).

[96] A. Gali, M. Fyta, and E. Kaxiras, Phys. Rev. B **77**, 155206 (2008).

[97] L. M. Pham, D. L. Sage, P. L. Stanwix, T. K. Yeung, D. Glenn, A. Trifonov, P. Cappellaro, P. R. Hemmer, M. D. Lukin, H. Park, A. Yacoby, and R. L. Walsworth, New Journal of Physics **13**, 045021 (2011).

[98] S. Arroyo-Camejo, M.-P. Adam, M. Besbes, J.-P. Hugonin, V. Jacques, J.-J. Greffet, J.-F. Roch, S. W. Hell, and F. Treussart, ACS Nano **7**, 10912–10919 (2013).

[99] G. Waldherr, J. Beck, P. Neumann, R. S. Said, M. Nitsche, M. L. Markham, D. J. Twitchen, J. Twamley, F. Jelezko, and J. Wrachtrup, **7**, 105–108 (2011).

[100] N. M. Nusran, M. Momeen Ummal, and M. V. Gurudev Dutt, Nature Nanotechnology **7**, 109–113 (2012).

[101] K. Fang, V. M. Acosta, C. Santori, Z. Huang, K. M. Itoh, H. Watanabe, S. Shikata, and R. G. Beausoleil, Phys. Rev. Lett. **110**, 130802 (2013).

[102] L. M. Pham, N. Bar-Gill, C. Belthangady, D. Le Sage, P. Cappellaro, M. D. Lukin, A. Yacoby, and R. L. Walsworth, Phys. Rev. B **86**, 045214 (2012).

[103] D. M. Toyli, D. J. Christle, A. Alkauskas, B. B. Buckley, C. G. Van de Walle, and D. D. Awschalom, Phys. Rev. X **2**, 031001 (2012).

[104] M. L. Goldman, M. W. Doherty, A. Sipahigil, N. Y. Yao, S. D. Bennett, N. B. Manson, A. Kubanek, and M. D. Lukin, Phys. Rev. B **91**, 165201 (2015).

[105] L. J. Rogers, M. W. Doherty, M. S. J. Barson, S. Onoda, T. Ohshima, and N. B. Manson, New Journal of Physics **17**, 013048 (2015).

[106] Y. Ma, M. Rohlfing, and A. Gali, Phys. Rev. B **81**, 041204(R) (2010).

[107] A. Ranjbar, M. Babamoradi, M. Heidari Saani, M. A. Vesaghi, K. Esfarjani, and Y. Kawazoe, Phys. Rev. B **84**, 165212 (2011).

[108] A. Gali, T. Simon, and J. E. Lowther, New Journal of Physics **13**, 025016 (2011).

[109] J. Zhang, C.-Z. Wang, Z. Z. Zhu, and V. V. Dobrovitski, Phys. Rev. B **84**, 035211 (2011).

[110] A. Alkauskas, B. B. Buckley, D. D. Awschalom, and C. G. V. de Walle, New Journal of Physics **16**, 073026 (2014).

[111] H. J. Mamin, M. H. Sherwood, M. Kim, C. T. Rettner, K. O. D. D. Awschalom, and D. Rugar, Phys. Rev. Lett. **113**, 030803 (2014).

[112] P. Kehayias, M. Mrózek, V. M. Acosta, A. Jarmola, D. S. Rudnicki, R. Folman, W. Gawlik, and D. Budker, Phys. Rev. B **89**, 245202 (2014).

[113] S. Armstrong, L. J. Rogers, R. L. McMurtrie, and N. B. Manson, Physics Procedia **3**, 1569–1575 (2010).

[114] L. Robledo, H. Bernien, I. van Weperen, and R. Hanson, Phys. Rev. Lett. **105**, 177403 (2010).

[115] B. J. Hausmann, M. Khan, Y. Zhang, T. M. Babinec, K. Martinick, M. McCutcheon, P. R. Hemmer, and M. Loncar, Diamond and Related Materials **19**, 621–629 (2010).

[116] T.-L. Wee, Y.-K. Tzeng, C.-C. Han, H.-C. Chang, W. Fann, J.-H. Hsu, K.-M. Chen, and Y.-C. Yu, The Journal of Physical Chemistry A **111**, 9379–9386 (2007).

[117] P. Kehayias, M. W. Doherty, D. English, R. Fischer, A. Jarmola, K. Jensen, N. Leefer, P. Hemmer, N. B. Manson, and D. Budker, Phys. Rev. B **88**, 165202 (2013).

[118] Y. Dumeige, M. Chipaux, V. Jacques, F. Treussart, J.-F. Roch, T. Debuisschert, V. M. Acosta, A. Jarmola, K. Jensen, P. Kehayias, and D. Budker, Phys. Rev. B **87**, 155202 (2013).

[119] K. Jensen, N. Leefer, A. Jarmola, Y. Dumeige, V. M. Acosta, P. Kehayias, B. Patton, and D. Budker, Phys. Rev. Lett. **112**, 160802 (2014).

[120] H. Clevenson, M. E. Trusheim, T. S. C. Teale, D. Braje, and D. Englund, arXiv:1406.5235 (2014).

[121] B. J. Shields, Q. P. Unterreithmeier, N. P. de Leon, H. Park, and M. D. Lukin, Phys. Rev. Lett. **114**, 136402 (2015).

[122] A. Brenneis, L. Gaudreau, M. Seifert, H. Karl, M. S. Brandt, H. Huebl, J. A. Garrido, F. H. L. Koppens, and A. W. Holleitner, Nature Nanotechnology **10**, 135–139 (2015).

[123] E. Bourgeois, A. Jarmola, M. Gulka, J. Hruby, D. Budker, and M. Nesladek, arXiv:1502.07551 (2015).

[124] L. M. Pham, N. Bar-Gill, D. Le Sage, C. Belthangady, A. Stacey, M. Markham, D. J. Twitchen, M. D. Lukin, and R. L. Walsworth, Phys. Rev. B **86**, 121202 (2012).

[125] J. Michl, T. Teraji, S. Zaiser, I. Jakobi, G. Waldherr, F. Dolde, P. Neumann, M. W. Doherty, N. B. Manson, J. Isoya, and J. Wrachtrup, Applied Physics Letters **104**, 102407 (2014).

[126] M. Lesik, J.-P. Tetienne, A. Tallaire, J. Achard, V. Mille, A. Gicquel, J.-F. Roch, and V. Jacques, Applied Physics Letters **104**, 113107 (2014).

[127] S. Cui and E. L. Hu, Applied Physics Letters **103**, 051603 (2013).

[128] V. M. Acosta, C. Santori, A. Faraon, Z. Huang, K.-M. C. Fu, A. Stacey, D. A. Simpson, K. Ganesan, S. Tomljenovic-Hanic, A. D. Greentree, S. Prawer, and R. G. Beausoleil, Phys. Rev. Lett. **108**, 206401 (2012).

[129] S. Castelletto, B. C. Johnson, V. Ivady, N. Stavrias, T. Umeda, A. Gali, and T. Ohshima, Nat Mater **13**, 151–156 (2014).

[130] G. Davies and M. F. Hamer, Proceedings of the Royal Society of London. Series A, Mathematical and Physical Sciences **348**, 285–298 (1976).

[131] A. Lenef and S. C. Rand, Phys. Rev. B **53**, 13441–13455 (1996).

[132] P. Delaney, J. C. Greer, and J. A. Larsson, Nano Letters **10**, 610–614 (2010).

[133] G. Davies, Journal of Physics C: Solid State Physics **7**, 3797 (1974).

[134] B. T. Webber, M. C. Per, D. W. Drumm, L. C. L. Hollenberg, and S. P. Russo, Phys. Rev. B **85**, 014102 (2012).

[135] A. A. Maradudin, *Solid State Physics*, edited by F. Seitz and D. Turnbull, Vol. 18 (Academic Press, 1966), p. 273.

[136] H. C. Longuet-Higgins, U. Öpik, M. H. L. Pryce, and R. A. Sack, Proceedings of the Royal Society of London. Series A. Mathematical and Physical Sciences **244**, 1–16 (1958).

[137] N. Mounet and N. Marzari, Phys. Rev. B **71**, 205214 (2005).

[138] A. Bosak and M. Krisch, Phys. Rev. B **72**, 224305 (2005).

[139] A. L. Schawlow, Rev. Mod. Phys. **54**, 697–707 (1982).

[140] W. E. Moerner, ed., *Persistent Spectral Hole-Burning: Science and Applications* (Springer-Verlag, 1988).

[141] M. J. Thorpe, L. Rippe, T. M. Fortier, M. S. Kirchner, and T. Rosenband, Nat Photon **5**, 688–693 (2011).

[142] N. B. Manson, L. J. Rogers, E. A. Wilson, and C. Wei, Journal of Luminescence **130**, 1659–1667 (2010).

[143] V. M. Acosta, K. Jensen, C. Santori, D. Budker, and R. G. Beausoleil, Phys. Rev. Lett. **110**, 213605 (2013).

[144] A. Dréau, M. Lesik, L. Rondin, P. Spinicelli, O. Arcizet, J.-F. Roch, and V. Jacques, Phys. Rev. B **84**, 195204 (2011).

[145] L. W. Hillman, R. W. Boyd, J. Krasinski, and C. R. Stroud, Jr., Optics Communications **45**, 416–419 (1983).

[146] A. Eilam, I. Azuri, A. V. Sharypov, A. D. Wilson-Gordon, and H. Friedmann, Opt. Lett. **35**, 772–774 (2010).

[147] Several lineshape functions (including Lorentzian and Gaussian) described our hole spectra well, and we chose to use Lorentzian fits. A rigorous analysis of hole parameters (width, contrast, and central frequency) should use lineshape functions derived from the broadening mechanism.

[148] P. Neumann, I. Jakobi, F. Dolde, C. Burk, R. Reuter, G. Waldherr, J. Honert, T. Wolf, A. Brunner, J. H. Shim, D. Suter, H. Sumiya, J. Isoya, and J. Wrachtrup, Nano Letters **13**, 2738–2742 (2013).

[149] J. S. Hodges, N. Y. Yao, D. Maclaurin, C. Rastogi, M. D. Lukin, and D. Englund, Phys. Rev. A **87**, 032118 (2013).

[150] A. Laraoui, J. S. Hodges, C. A. Ryan, and C. A. Meriles, Phys. Rev. B **84**, 104301 (2011).

[151] N. Mizuochi, P. Neumann, F. Rempp, J. Beck, V. Jacques, P. Siyushev, K. Nakamura, D. J. Twitchen, H. Watanabe, S. Yamasaki, F. Jelezko, and J. Wrachtrup, Phys. Rev. B **80**, 041201 (2009).

[152] G. de Lange, Z. H. Wang, D. Ristè, V. V. Dobrovitski, and R. Hanson, Science **330**, 60–63 (2010).

[153] G. de Lange, T. van der Sar, M. Blok, Z.-H. Wang, V. Dobrovitski, and R. Hanson, Scientific Reports **2** (2012).

[154] N. Bar-Gill, L. Pham, C. Belthangady, D. L. Sage, P. Cappellaro, J. Maze, M. Lukin, A. Yacoby, and R. Walsworth, Nature Communications **3**, 858 (2012).

[155] N. Bar-Gill, L. M. Pham, A. Jarmola, D. Budker, and R. L. Walsworth, Nature Communications **4**, 1743 (2013).

[156] C. Belthangady, N. Bar-Gill, L. M. Pham, K. Arai, D. Le Sage, P. Cappellaro, and R. L. Walsworth, Phys. Rev. Lett. **110**, 157601 (2013).

[157] L. Childress, M. V. Gurudev Dutt, J. M. Taylor, A. S. Zibrov, F. Jelezko, J. Wrachtrup, P. R. Hemmer, and M. D. Lukin, Science **314**, 281–285 (2006).

[158] M. S. Grinolds, S. Hong, P. Maletinsky, L. Luan, M. D. Lukin, R. L. Walsworth, and A. Yacoby, Nat Phys **9**, 215–219 (2013).

[159] M. Loretz, J. M. Boss, T. Rosskopf, H. J. Mamin, D. Rugar, and C. L. Degen, Phys. Rev. X **5**, 021009 (2015).

[160] W. V. Smith, P. P. Sorokin, I. L. Gelles, and G. J. Lasher, Phys. Rev. **115**, 1546–1552 (1959).

[161] J. H. N. Loubser and J. A. van Wyk, Reports on Progress in Physics **41**, 1201 (1978).

[162] R. de Sousa, "Electron Spin as a Spectrometer of Nuclear-Spin Noise and Other Fluctuations", in *Electron Spin Resonance and Related Phenomena in Low-Dimensional Structures*, Vol. 115, edited by M. Fanciulli, Topics in Applied Physics (Springer, 2009), pp. 183–220.

[163] P. L. Stanwix, L. M. Pham, J. R. Maze, D. Le Sage, T. K. Yeung, P. Cappellaro, P. R. Hemmer, A. Yacoby, M. D. Lukin, and R. L. Walsworth, Phys. Rev. B **82**, 201201 (2010).

[164] Fedor Jelezko proposed this experiment during a discussion on possible follow-up NV singlet spectroscopy experiments.

[165] R. Fischer, A. Jarmola, P. Kehayias, and D. Budker, Phys. Rev. B **87**, 125207 (2013).

[166] D. Maclaurin, M. W. Doherty, L. C. L. Hollenberg, and A. M. Martin, Phys. Rev. Lett. **108**, 240403 (2012).

[167] M. P. Ledbetter, K. Jensen, R. Fischer, A. Jarmola, and D. Budker, Phys. Rev. A **86**, 052116 (2012).

[168] A. Ajoy and P. Cappellaro, Phys. Rev. A **86**, 062104 (2012).

[169] M. A. Kowarsky, L. C. L. Hollenberg, and A. M. Martin, Phys. Rev. A **90**, 042116 (2014).

[170] D. J. Griffiths, *Introduction to Quantum Mechanics*, 2nd edition (Pearson Prentice Hall, 2004).